



Saurashtra University

Re – Accredited Grade 'B' by NAAC
(CGPA 2.93)

Tayade, Rajesh J., 2005, “*Studies on Decomposition of Dyes and Volatile Organic Compounds Using Semiconductor Photocatalysts*”, thesis PhD, Saurashtra University

<http://etheses.saurashtrauniversity.edu/id/859>

Copyright and moral rights for this thesis are retained by the author

A copy can be downloaded for personal non-commercial research or study, without prior permission or charge.

This thesis cannot be reproduced or quoted extensively from without first obtaining permission in writing from the Author.

The content must not be changed in any way or sold commercially in any format or medium without the formal permission of the Author

When referring to this work, full bibliographic details including the author, title, awarding institution and date of the thesis must be given.

Saurashtra University Theses Service
<http://etheses.saurashtrauniversity.edu>
repository@sauuni.ernet.in

© The Author

**STUDIES ON DECOMPOSITION OF DYES AND
VOLATILE ORGANIC COMPOUNDS USING
SEMICONDUCTOR PHOTOCATALYSTS**

THESIS

Submitted to



**SAURASHTRA UNIVERSITY
Rajkot-360 005**

for the Degree of

**DOCTOR OF PHILOSOPHY
in
PHYSICS**

by

TAYADE RAJESH JAGANNATH

(Ph. D. Regd. No. 2495 / 07-04-2000)

GUIDE:

Dr. R.G. Kulkarni

M.S. (KANSAS), Ph. D. (VIRGINIA)

**Rtd. Prof. & Head
DEPARTMENT OF PHYSICS
SAURASHTRA UNIVERSITY
RAJKOT- 360 005, INDIA**

2005

ACKNOWLEDGEMENTS

At the outset, I would like to mention that it is my supervisor **Dr. R.G. Kulkarni** (Rtd.), Prof. & Head, Dept. of Physics, Saurashtra University, Rajkot with whose enduring guidance and timely constructive comments made this work in the present form. Even distance of around 200 kms. between Rajkot and Bhavnagar- my place of work, did not prevent his ideas, suggestions and bountiful love and affection to reach me even at a speed greater than the speed of light. He always kept me inspiring and boosted by confidence. He is indeed very kind, supportive and best enough in all respects to anyone.

All words of thanks, praise and adoration for my beloved and dearest **Dr. R. V. Jasra**, Dy. Director, CSMCRI, Bhavnagar fall small when I retrospect the kind of his inspiring, relentless and invaluable guidance, insights and advice during the work. All onus goes to him for making this research happen. He made available all necessary chemicals, instruments, newly constructed well furnished lab and other paraphernalia for carrying out the work uninterruptedly. The road to a research was bumpy and the advancing steps were initially very short. He can be anointed as a true co-supervisor of my thesis work

I am highly indebted to **Dr. Pushpito K. Ghosh**, Director, CSMCRI, Bhavnagar, for granting kind and generous permission to carry out this research work in one of the country's premier R & D lab in the field of catalysis, marine chemicals and environment and Reverse Osmosis. Our honourable Director was infact very much supportive and directive vision to promote R & D in this exciting field of photocatalysis.

My acknowledgements will be incomplete if I don't ornament a special mention and thanks to **Dr. H. C. Bajaj**, Aast. Director, CSMCRI, Bhavnagar, who bestowed untiring help, advice and lovely support about pretty much anything.

I would like to thanks for my close friends Mr. Shobhit Singh Chauhan, Mr. Jince Sebastian, Mr. Mukesh Kr. Yadav, and Mr. Sunil A.P., for gratuitous support in all respect throughout my research and especially at the time of writing of this thesis, which was invaluable. I am overwhelmingly thankful to all of them not only for the time and effort spent proof reading this manuscript and for their valuable suggestions and comments, but also for their unconditional friendship. All the moments shared with them are very special and important to me.

I render my thankfulness to Prof. K. N. Iyyer, Head, Dept. of Physics, Saurashtra University, Rajkot and Prof. D. G. Kuberkar, Prof. H. H. Joshi, Prof. M. J. Joshi, Prof. G. J. Baldha for there prompt help in many occasions.

I express my sincere thanks to Dr. D.B. Shukla and Dr. (Mrs.) Anjani Bhatt for introducing me to the photocatalysis experimental work in my initial stages and for their support in building a basic niche in me to carry out this research work in photocatalysis.

I would like to place my respect and deep sense of gratitude to Dr. R. S. Shukla, Dr. S.H.R. Abdi, Dr. S. D. Bhatt, Dr. R. I. Kureshy, Dr. R. S. Somani, Dr. S. Kannan, Dr. N. H. Khan, Dr. H. M. Mody, Dr. Jugnu Bhatt, Dr. Beena Tyagi, Dr. A. B. Boricha for their encouraging and supportive words.

I am grateful to Dr. P. Paul, Head, Analytical Science Discipline, for providing easy access to various instrumental facilities. I am also indebted to Dr. Amitava Das for readily providing DRS measurements, Dr. R. P. Pandya for XRF, Mr. Chandrakant C. K. for SEM, Dr. (Mrs.) P.B. Bhatt

for recording XRD, Mr. V. P. Boricha for FTIR. Mr. Jagan Mohan for thermal analysis and other staff members, Dr. P. S. Subramanian, Dr. E. Suresh, Dr. P. Dastidar.

I would also like to thank Dr. (Mrs.) K. H. Modi for COD measurements facility and Mr. S. T. Talreja & Mr. Pradeep Parmar for upkeep of the instruments.

I would also like to Mr. Popoatbhai and Mr. Jeetubhai, glass blowing division, who made glass reactors, vessels etc and roughening of tiles in time.

I convey my words of appreciation to Incharge, I. T. Cell Mr. Pradeep Kumar and staff Mr. H. S. Vasudeva, Mr. Pramod Makwana, Mr. Sanjay Jani and Ms. Himani for their assistance in various problems related to PC and software during this period.

I am also thankful to Planning Cell staff Mr. S. N. Ghosh, Mr. Atul Shah and Mr. M. L. Bhatt for the support in correspondence with university.

I am very much gratified to the staff from Director Secretariat, Library, BDIM, Electrical, Mechanical, Carpentry, Refrigeration, Store & Purchase, Administration, Finance & Accounts, Canteen and Watch & Ward for their co-operation during this period.

I am thankful to Mr. P. G. Mohanan Pillai, PS, Dy. Director for his help in all official works. I also acknowledge Mr. Chimanbhai.Gohil, Mr. Bharat Parmar, Mr. Jayanthi Parmar, Mr. Ali Lakhani, Mr. Bahadur Vaghela, for their prompt help rendered during this period.

I am also thankful to Dr. Priti. H. Pandya, Dr. Yogi. M. Badheka, Dr. Chintan Chudasama, Dr. Darshan Kudaliya, Dr. Nilay Pachal, Dr. Suresh Lagate, Dr. Pares Dave, Dr. Atindra Shukla, Dr. Amit Dubey, Dr. C. Gunanathan, and for their valuable suggestions and support in many difficult situations.

I would also like to acknowledge the support of my friends and colleagues Mr. Vivek Srivastava, Mr. Dharmesh Parmar, Mr. Jaysukh Parmar, Ms. Rohini Parmar, Mr. D. Krishna Kumar, Mr. Amar Ballabh, Mr. Surendra Singh, Mr. Irshad Ahmed Mr. Amilan Jose, Dr. Kishor Dasari, Mr. Manish Mishra, Mr. Kartik Patel, Ms. Kavita Pathak, Mr. Achyut Bhatt, Mr. Devendra Ghelani, Mr. Hasmukh Patel, Mr. Sumeet Sharma, Mr. Kalpesh Sidhpuria, Mr. Vishal Mayani, Mr. Mallikarjun Patil, Mr. Kiran Patil, Mr. Arvind Chaudhary, Ms Chitrleka Khatri, Mr. Praveen Suroliya, Mr. Afsar Ali, Mr. Prabhash Prasad, Mr. J. Krishna Mohan, Mr. Rajkumar, Mr. Shubhankar Bose and Mr. Munir Khokhar for providing a good friendly working atmosphere.

I express my sincere gratitude to my mother, father, sisters, brothers, for their moral support to complete this work successfully. All of them have gone through important phases in each of their lives that I have largely missed.

I appreciate the patience of my wife Manisha for being supportive to me. She had managed everything back home excellently. I love my son Nishant and infant daughter Parnika who did disturb a little during works.

Finally I place my regards to all those who helped me knowingly or unknowingly.

It is time to celebrate, and start a new scientific life,

Rajesh J. Tayade

(with group V elements like P, As, Sb, and Bi) corresponds to the formation of empty acceptor levels near the valence band, creating positive charge carriers where current is carried mainly by positive charges. The surface defects and impurities in p-type or n-type semiconductors are responsible for the change in bandgap of the semiconductor.

1.1.3. Semiconductor Photocatalysis

A single particle of semiconductor can provide both oxidizing and reducing species for the reaction. Semiconductors like TiO_2 , ZnO , Fe_2O_3 , CdS , ZnS can be used as photocatalyst for the wastewater treatment and polluted air purification [2, 13-21]. Semiconductors can act as sensitizer for light-induced processes. Absorption of a photon of energy greater than the bandgap energy leads to the formation of an electron-hole pair. In the absence of suitable scavengers, the stored energy is dissipated within few nanoseconds by recombination [6]. If a suitable scavenger or surface defects state is available to trap electron or hole, recombination is prevented and subsequent redox reaction may occur. The valence band holes are powerful oxidants (+1.0 to +3.5V vs. NHE depending on the semiconductor and pH), while the conduction band electrons are good reductants (+0.5 to -1.5V vs. NHE) [22].

Most organic photodegradation reactions utilize the oxidizing power of the holes either directly or indirectly. However, in very small semiconductor particle suspensions, both species are present on the surface. Therefore, careful consideration of both the oxidative and the reductive paths is required.

Semiconductor photocatalysis is an emerging technique valuable for water and air purification and remediation. Fundamental and applied research on this subject has been performed extensively during the last 30 years all over the world [2, 9, 29, 31-34] Nowadays, the main goal of research and development in semiconductor heterogeneous photocatalysis which is a part of Advanced Oxidation Process (AOPs) used for air and wastewater treatment [9].

1.1.4. Semiconductor Photocatalysts used in Photocatalysis

Metal oxides and sulphides represent a large class of semiconductor materials suitable for photocatalysis [31-33]. Table 1.3 lists some selected semiconductor materials, which have been reported to be used for photocatalytic reactions, with their VB and

Titanium dioxide, Degussa P-25, from *Degussa Corporation, Germany* has become the standard for photoreactivity in environmental applications. This material is cheap and extremely photoactive. Therefore it is widely used in semiconductor photochemistry research, particularly with regard to work involving semiconductor powder dispersions. TiO₂ produced through high-temperature (greater than 1200°C) flame hydrolysis of TiCl₄ in the presence of hydrogen and oxygen. The TiO₂ so formed, is treated with steam to remove HCl, which is also produced as part of the reaction. The product is 99.5% pure TiO₂ (anatase: rutile ratio, 70:30), which is non-porous, with rounded edges cubic particles. The P-25 TiO₂ Powder has a surface area of 55±15 m²g⁻¹ and an average particle diameter of 30 nm. It is important to note that 90% of the material does not exist as isolated particles, but rather as irreducible complex primary aggregates, typically of approximately 0.1 μm in diameter. Degussa P-25 possesses an excellent activity for the degradation of organic and inorganic pollutant in water and air. The valance band and conduction band positions for Degussa P-25 are reported as +2.9 and -0.3 V respectively at pH=1.

1.1.5. The Structures of TiO₂

TiO₂ exists in three main crystallographic forms, brookite, anatase and rutile [24]. Other structures exist as well, for example cotunnite TiO₂ has been synthesized at high pressures and is one of the hardest polycrystalline materials [25]. However, only anatase and rutile play role in all the applications of TiO₂. Figure 1.3 shows the bulk structures of rutile and anatase TiO₂. The energy bandgap of anatase (3.23 eV, 384 nm) and rutile (3.02 eV, 411 nm) combines with the valance band position to generate highly energetic holes at the interface giving rise to easy oxidation reactions. Anatase has been found, in most of the cases, to be photocatalytically more active than rutile [26]. The structure of rutile and anatase can be described in terms of chain of TiO₆ octahedra. The two crystal structures differ by the distortion of each octahedron and by the assembly pattern of the octahedral chain. Figure 1.4 shows the unit cell structure of the rutile and anatase crystal. Each Ti⁴⁺ ion is surrounded by an octahedron of six O₂⁻ ions. The octahedron in rutile is not regular, showing a slight orthorhombic distortion. The octahedron in anatase is significantly distorted so that its

CHAPTER - 2

NANOCRYSTALLINE SEMICONDUCTOR

PHOTOCATALYSTS

2.1. Introduction

Nanocrystalline metals and alloys, with average and range of grain sizes typically smaller than 100 nm, have been the subject of considerable research in recent years. This interest has been spurred by progress in the processing of materials and by advances in computational materials science. As materials science and engineering evolves, new approaches provide increasingly precise control at the atomic and molecular levels over the structural properties and enhance the function of materials. Although this is largely driven by a recognition that familiar bulk properties like mechanical, magnetic, electronic, and optoelectronic depend upon atomic and molecular building blocks, the same properties often differ from bulk when examined on the nanometer scale. Smallness in itself is not the goal. Instead, it is the realization, or now possibly even the expectation, those new properties intrinsic to novel structures will enable breakthroughs in a multitude of technologically important areas [1].

The impact of nanostructure materials with an intrinsic property of high surface area is an area of increasing importance for understanding, creating, and improving materials for diverse applications. The synthesis of nanoparticles with controlled size and composition is of technological interest and challenge. The effort to understand the physics of ever-smaller structures has kept pace with attempts to exploit their beneficial properties. The phenomena of semiconductor nanocrystals showing size-tunable optical properties and other metal nanoparticles that influence the activity and specificity of catalysis have been integrated into exploratory optical and electronic devices [2].

In particular, there has been a lot of emphasis on the production of nanoparticles of TiO_2 for a wide variety of applications [3]. Synthetic routes for TiO_2 production usually result in titanium hydroxide, amorphous solid TiO_2 or crystallites like anatase or rutile depending on the preparation route and experimental conditions. It is also known that the transformation behaviour from the amorphous to the anatase or rutile phase is influenced by the synthesis conditions; however, most of the literature shows that alkoxide-based sol-gel or precipitation processes yield amorphous titania precursors or powders preferentially in the anatase phase [4-6]. The anatase phase of TiO_2 , which is stable phase at low temperatures, has gained importance as a

photocatalyst for photodecomposition and solar energy conversion because of its high photoactivity [7-9].

TiO₂ shows different electrical characteristics with oxygen partial pressure, because it has wide chemical stability and a non-stoichiometric phase region. Because of this, it is suitable as a humidity sensor and high-temperature oxygen sensor [10-11]. Furthermore, the properties of nanosized semiconductor particles have long been known to depend very sensitively on the particle size [12]. As the diameter of crystallite approaches the exciton Bohr diameter, a splitting of the energy bands into discrete quantised energy levels occur. This is the so-called quantum size effect. Size quantization leads to a blue shift in the absorption spectrum due to increased bandgap, nonlinear optical properties, and unusual luminescence.

Nanostructured materials can be prepared by several methods namely sol-gel chemistry, sputtering and evaporation, controlled crystallization of an amorphous precursor and gas condensation [13-14]. The sol-gel technique has emerged as a promising processing route for the synthesis of nano-sized particles because of the simplicity of sol-gel processing in addition to its high purity resulting from the availability of high purity chemicals as raw materials [15-16].

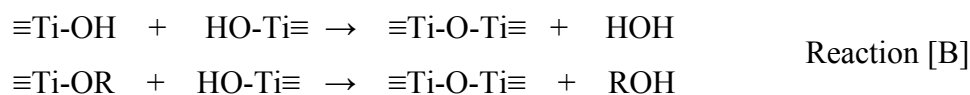
Controlling the particle size, however, is not an easy task in the case of using other methods. It is widely accepted that as the particle size falls in the nanometer size range, the physical and chemical properties of the semiconductor are predominantly governed by the surface of the particle as compared with the bulk semiconductor because the surface to volume ratio becomes more significant [17]. Therefore, the photocatalytic characteristics of TiO₂ are strongly affected by its particle size and control of the particle size becomes one of the most important parameters.

2.1.1. Sol-Gel Chemistry

The sol-gel reaction is said to have occurred when a metal alkoxide reacts with water to form a metal hydroxide which condenses into a metal-oxygen-metal sequence, with the liberation of water and alcohol. The metal may be aluminum, tin, cesium, the transition elements titanium, zirconium, the metalloid silicon, etc [18]. Sol-gel chemistry involves two reaction steps. The first step, named the hydrolysis step, is illustrated in Reaction [A] below for a generalized metal alkoxide:



Where M represents a metal alkoxide and the R group represents an alkyl chain such as methyl, ethyl, isopropyl, tert-butyl, etc., and the nature of this group plays a role in the rate of the hydrolysis reaction. In general, the smaller such groups are, the faster the reaction so that titanium isopropoxide, (where R = isopropyl), undergoes hydrolysis faster than titanium butoxide, (R = n-butyl), other conditions being the same. The R group is also important to the shrinkage during curing as losing more volume (with larger ROH molecules) causes greater shrinkage. The mechanism of Reaction [A] proceeds in three stages. First, the “metal” atom of the metal alkoxide (in this case the metalloid titanium) undergoes nucleophilic attack by the oxygen atom in a water molecule. While the titanium atom is in this penta-coordinated state, a proton is transferred from the water molecule to an OR group on the same titanium atom. Finally, the ROH molecule is released from the titanium atom [19]. The second step in the sol-gel process is the polycondensation step which can take place by either of the two sub-reactions in [B] below:



The existence of the second sub-reaction implies that the hydrolysis step shown in Reaction [A] need not be complete for polycondensation to begin. Both sub-reactions in [B] lead to the same $\equiv Ti-O-Ti\equiv$ bridge. Note that the reactant titanates in reaction(s) [B] have three other reactive sites that are not shown (recall the original titanium structure from Reaction [A]) which may participate in network development.

All three reactions in [A] and [B] are reversible. Although not universally accepted, many scientists believe that two moles of water are required for every one mole of tetrafunctional alkoxide in the sol-gel reaction. This was alluded to before upon pointing out that the hydrolysis step need not be complete for condensation to begin. If this is the case, a net loss of four moles of alcohol would occur upon complete conversion of one mole of tetrafunctional titanium alkoxide to the amorphous titanium dioxide network.

2.1.2. Photocatalytic Activity of nanocrystalline TiO₂

Since the photocatalytic activity is mostly confined to the surface of the photocatalytic material, its surface area must be increased to maximize the photocatalytic efficiency. One way to do this is the synthesis of nano-sized TiO₂ particles to increase photocatalytic reaction sites on the surface. Also, the amount of anatase phase must be maximized among those than the crystalline phases such as anatase, rutile, brookite, because the anatase phase shows a higher photocatalytic activity. Other than making nanosized semiconductor, the enhancement in the photocatalytic activity of the semiconductor were studied by doping the metal ion on the surface of semiconductor photocatalyst to trap the electron, and to decrease the electron-hole pair recombination [20-30].

The bandgap plays major role in the generation and recombination of electron-hole pair in the semiconductor, which are the main processes involved in the degradation of organic pollutants. The bandgap of the semiconductor photocatalyst depends upon size, support of the semiconductor, and preparation method. The previous report shows that, the nanocrystalline semiconductor possesses higher photocatalytic activity than that of bulk semiconductor. The recombination rate of the electron hole pair is higher in bulk or large size semiconductor photocatalyst particles, which decreases the photocatalytic activity of the semiconductor photocatalyst. Many reports show that the sol-gel route is the simple way for the preparation of nanocrystalline semiconductor.

The bandgap of this nanocrystalline TiO₂ was reported to be changed by calcination under air. Another way of changing the bandgap of the semiconductor is by loading or doping the transition metal. The doping of metal ion prevents the electron hole pair

recombination, which helps to improve the photocatalytic activity of the semiconductor photocatalyst [31-41].

To date, anatase form of titanium dioxide (TiO_2) is widely used mainly because of its high photocatalytic activity. As described earlier, anatase is a wide bandgap semiconductor with bandgap energy of 3.2 eV, so only solar radiations with wavelengths below 387.5 nm is absorbed to form the e^-/h^+ pairs [46, 47].

At the ground level, however, solar irradiation starts at about 300 nm; thus approximately 4% of the total spectrum can activate TiO_2 . Hence, for solar applications, materials that exhibit similar photoactivity as anatase but possess spectral properties in the visible part of the solar spectrum should be developed.

2.1.3. Aim for Catalyst Preparation

The objectives for synthesis of the nanocrystalline TiO_2 semiconductor is to achieve higher photocatalytic activity of the semiconductor photocatalyst by utilising visible part of solar spectrum and to study the effect of calcination on the bandgap and the photocatalytic activity of the nanocrystalline TiO_2 semiconductor.

To study the effect of metal ion loading on the bandgap and the photoactivity of the semiconductor photocatalyst, we have impregnated metal ion like Ag, Fe, Cu, Co, and Ni was impregnated on the surface of semiconductor photocatalyst. The work function of these transition metal ions is different than the semiconductor photocatalyst that results in the trapping of electron-hole pairs, which affects the photocatalytic activity of the semiconductor photocatalyst.

The photocatalytic activity was determined by degradation of organic compounds like acetophenone (AP), nitrobenzene (NB) that are found in wastewaters and dyes like methylen blue (MB), malachite green (MG) that are found in the industrial waste of textile industries alongwith number of other dyes So we have tried to study the degradation dyes MB, MG and organic pollutants AP, NB under ultra violet light by using the synthesized semiconductor photocatalysts in this study. The effect of induced bandgap in the semiconductor photocatalyst on the photocatalytic activity for degradation of the organic compound and dyes was also studied.

2.2. Synthesis of Nanocrystalline Semiconductor Photocatalyst

2.2.1 Chemicals & Materials

Titanium tetra isopropoxide (97%), Copper acetate LR grade, and Nickel acetate were procured from *Aldrich* USA. Silver nitrate AR grade was procured from Ranbaxy, *Fine Chemicals Limited*, India. Cobalt chloride, Ferric chloride, Methylene blue, Malachite green and Nitrobenzene AR grade (99.0%) were procured from *s. d. Fine Chem. Limited*, India. and acetophenone AR grade and COD Standard chemical reagents (Solution A: 1.14538, Solution B: 1.14681 and 1.14682) were purchased from E. Merck, India. P-25 Titanium dioxide was procured from *Degussa Corporation, Germany*.

2.2.2. Preparation of catalysts

Nanocrystalline TiO₂ photocatalyst were prepared by sol-gel method. The typical preparation flowchart is as shown in Figure 2.1. Following two methods are followed to get photocatalysts of the different bandgaps:

I. Calcination at various temperatures – Method A.

Nanocrystalline TiO₂ of various bandgaps were prepared by sol-gel process. The mixture of dry ethanol (100ml) and titanium tetra isopropoxide (30ml) was taken in a 250 ml round bottom flask. This mixture was continuously stirred for 30 minutes and then ultrasonicated for 30 minutes. Distilled water (24ml) was slowly added at the rate of 0.5 ml/min under continuous stirring. The precipitate obtained was dried using rotavapour (*Buchi Rotavapour, R-205*) slowly at 243K under vacuum (400 mm of Hg). The powder was then kept in an oven at 393K for 12 hours. The catalyst thus obtained is termed as NPC-393. NPC-393 was calcined at temperatures 583K, 628K, 673K, 713K, 753K, 833K, 913K in tubular furnace under airflow (Flow rate =3 LPM) and at 1023K in a muffle furnace without airflow for 11 hours. These calcined catalysts are termed as NPC-583, NPC-628, NPC-673, NPC-713, NPC-753, NPC-833, NPC-913 and NPC-1023. The numerals denote the calcination temperatures.

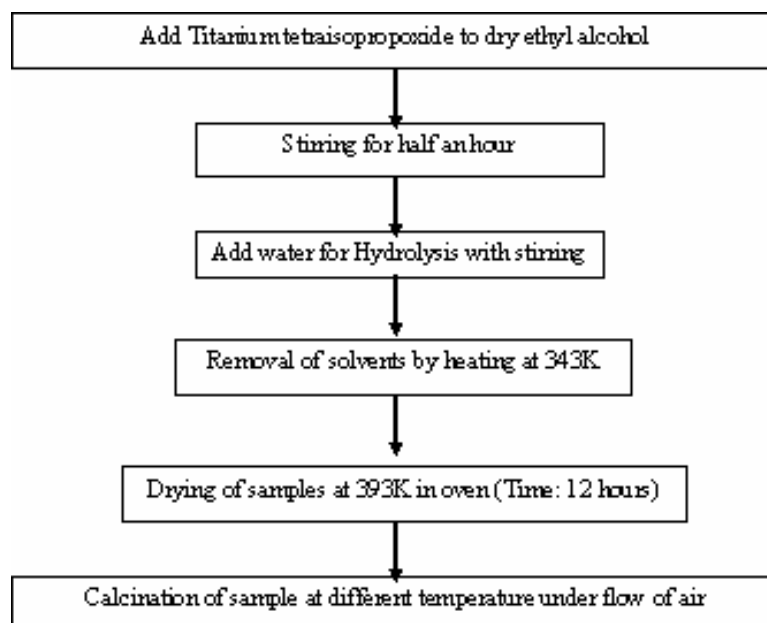


Figure 2.1: Schematic diagram of sol-gel synthesis of nanocrystalline TiO_2

II. Impregnation of metal ions on the surface of photocatalyst – Method B.

The catalysts were prepared in same way as per method A, except the rate adding water was changed to 2 ml/min to get nanocrystalline TiO_2 of higher crystallite size. This catalyst was calcined at 773K. The catalyst thus obtained is termed as MT-10. The prepared bare TiO_2 catalyst (MT-10) was suspended in separate aqueous solutions of silver nitrate, cobalt chloride, ferric chloride, copper acetate and nickel acetate separately [48].

All mixtures were stirred for 48 hours to get 0.5% loading of metal ion on the bare catalyst (MT-10). The slurry was dried in an oven at 393K for 12 hours. These dried catalysts were grounded with agate mortar and pestle thoroughly and calcined at 773K temperature for 4 hours. The impregnated nanocrystalline TiO_2 catalysts with metal ions are termed as Ti-M where M represent the impregnated metal ions. This process is termed as metal impregnation.

2.3. Characterisation of semiconductor photocatalysts

2.3.1. XRD

Powder X-ray diffraction patterns were recorded with Phillips X'pert MPD system using CuK α 1 radiation ($\lambda = 0.154056\text{nm}$). Diffraction patterns were measured in 2θ range 5° - 60° at a scan rate of 0.1°sec^{-1} . X-ray diffraction patterns were compared with the standard anatase and rutile diffractograms to find out the phase transition in TiO₂ [49]. The percent phase formed was determined from integrated peak intensity at $2\theta = 25.3$ (1 0 1) for anatase and peak at $2\theta = 27.4$ (1 1 0) for rutile. The percentage of anatase, A (%) was determined using the following Equation 2.1 [50].

$$A\% = \frac{100}{1 + 1.265 \frac{I_R}{I_A}} \quad \text{Equation 2.1}$$

I_R is the intensity of rutile peak at $2\theta = 27.4$ and I_A is the intensity of anatase peak at $2\theta = 25.3$

The crystallite size was estimated by the Scherrer formula [51] Equation 2.2 which is in general the accepted method to estimate the mean crystallite size. Crystallite size was determined from the characteristic peak of $2\theta = 25.3$ (1 0 1) for anatase and $2\theta = 27.4$ (1 1 0) for rutile with a shape factor (K) of 0.9,

$$\text{Crystallite size} = K\lambda / W \cos \theta \quad \text{Equation 2.2}$$

where $W = W_b - W_s$,

W_b = broadened profile width of experimental catalysts

W_s = standard profile width of reference silica catalysts.

λ , is the wavelength of X-ray radiation (CuK α 1=0.154056nm).

The crystallinity of the TiO₂ was determined by measuring the total peak area under five main peaks over the range of $2\theta = 5^\circ$ - 60° . The highest percentage crystallinity containing anatase phase was obtained for NPC-753, the percentage crystallinity of other catalysts were relative to the crystallinity of this catalysts, NPC-753.

The crystal structure transformation is known to occur on calcination of TiO₂ at higher temperatures [52-54]. The calcination temperature influences the catalyst activity as it affects the physical and electronic properties of the catalyst namely porosity, surface area, crystal structure, crystal size and bandgap. The amorphous–

anatase and anatase–rutile transformation depends strongly on the method of preparation, nature of precursor and calcination conditions [55].

The X-ray diffraction patterns of nanocrystalline TiO₂ synthesized by Method A are shown in Figure 2.2. TiO₂ catalysts prepared by this method were largely amorphous in nature before calcination. The percent crystallinity in anatase phase and the crystallite size of TiO₂ was observed to increase as the calcination temperature was increased. The nanocrystalline TiO₂ calcined in temperature range 583K-833K was anatase in nature. The phase transformation from anatase to rutile took place beyond 833K and at 1023K the phase constitution of TiO₂ was 100% rutile [56]. Therefore, the anatase to rutile phase conversion was observed to occur at higher temperature for nanocrystalline material compared to that of bulk TiO₂.

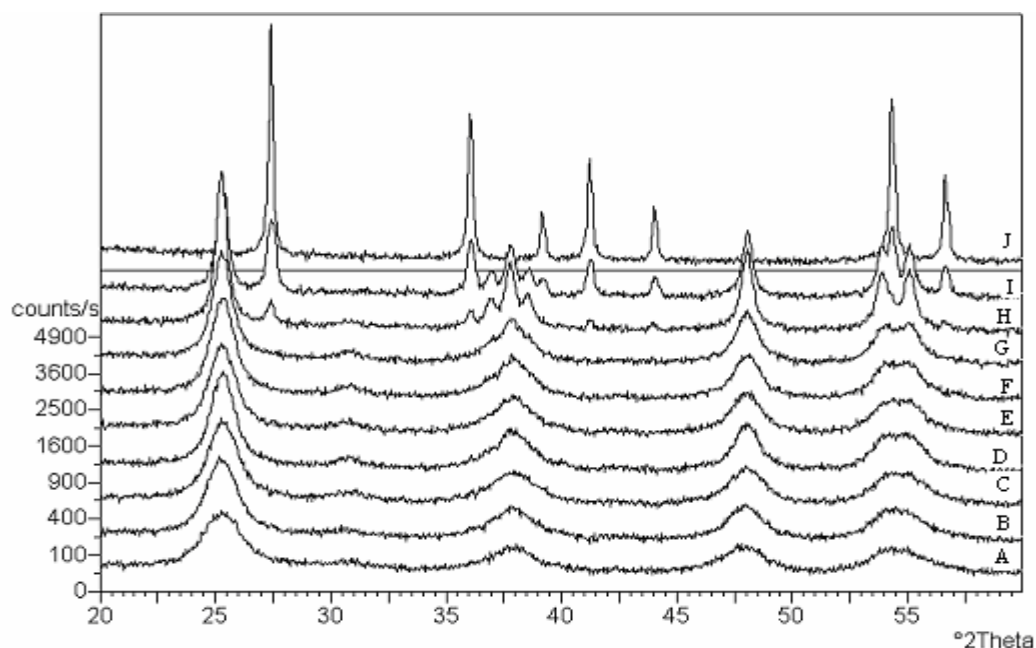


Figure 2.2: XRD patterns of nanocrystalline TiO₂ calcined at different temperatures:
A) NPC-393 B) NPC-583 C) NPC-628 D) NPC-673 E) NPC-713 F) NPC- 753
G) NPC- 833 H) P 25 I) NPC- 913 J) NPC-1023

The lattice parameters of anatase phase of nanocrystalline TiO₂ calcined at various temperatures were determined by XRD and lattice parameters were refined by *PowderX* software as given in Table 2.1.

Table 2.1: Crystallite size and lattice parameter of anatase in synthesized nanocrystalline TiO₂ prepared using method A.

Catalyst	Crystallite size of Anatase* (nm)	Crystallinity (%)	Lattice parameter of anatase (nm)		
			a	c	c/a
NPC-393	8	62	0.3877	0.921	2.376
NPC-583	9	80	0.3877	0.937	2.417
NPC-628	10	85	0.3867	0.932	2.410
NPC-673	12	90	0.3866	0.927	2.397
NPC-713	13	91	0.3852	0.924	2.398
NPC-753	14	100	0.3855	0.923	2.394
NPC-833	19	90	0.3845	0.919	2.390
NPC-913	29	70	0.3825	0.915	2.392
NPC-1023	-	65	-	-	-
P25	28	-	0.3855	9.21	2.389

(* The peak position chosen at $2\theta \approx 25.3^\circ$ for anatase.)

The catalyst synthesised at 393K had the highest surface area $259 \text{ m}^2\text{g}^{-1}$ (Table 2.3) and the smaller crystallite size of 8 nm. As the calcination temperature was raised to 913K, the surface area reduced to $2 \text{ m}^2\text{g}^{-1}$ and crystallite size of 29 nm. These data show that the TiO₂ catalysts synthesized are nanocrystalline with crystallite size varying from 8-29 nm. An increase in calcination temperature increases crystallite size and percentage crystallinity [30, 57]. The highest percentage of crystallinity was observed in NPC-753. The changes in crystallinity with varying temperatures are shown in Figure 2.3.

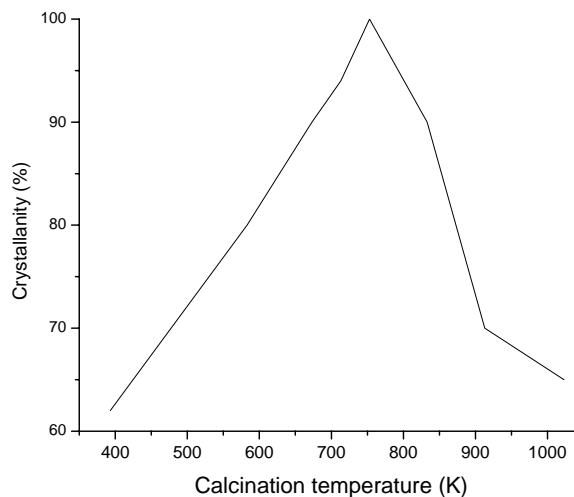


Figure 2.3: Effect of calcination temperature on crystallinity

The percentage ratio of anatase and rutile was 91:8 in the metal ion loaded catalysts synthesized by Method B as is the case with catalyst MT-10 (bare TiO_2). The XRD pattern shown in Figure 2.4 shows that MT-10 is crystalline in nature and the crystallite size of this catalyst is 38 nm. The peak average area in the XRD patterns of all catalysts demonstrates that the crystallinity of metal impregnated and MT-10 is nearly the same. There was 1-2 % reduction of anatase phase of TiO_2 after impregnation of metal ion. This may be due to the variation in the calcination temperature of the furnace. There was no additional peak observed in metal impregnated catalysts, this may be due to the less amount of impregnation of the metal ions.

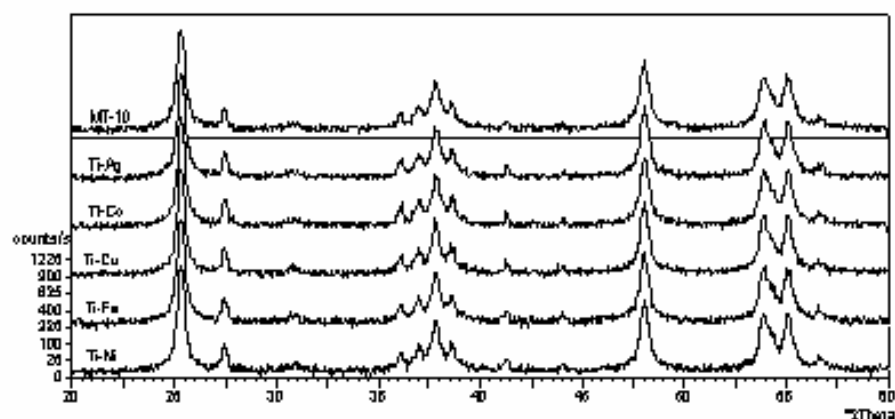


Figure 2.4: XRD patterns of nanocrystalline TiO₂ metal impregnated photocatalysts

The properties of the metal impregnated catalyst determined from XRD diffractograms are shown in Table 2.2. The catalysts prepared by metal impregnation show 6-12 nm change in crystallite size as compared to MT-10. Another change was the colour of impregnated catalysts. No additional peaks of metal ions in impregnated nanocrystalline TiO₂ in XRD patterns prepared by method B as shown in Figure 2.4 confirmed that there is no change in the structure of the TiO₂. The ratio of anatase to rutile in all the catalysts after impregnation of the metal was nearly same as shown in Table 2.2.

Table 2.2: XRD data of impregnated catalysts.

Catalyst	MT-10	Ti-Ag	Ti-Co	Ti-Cu	Ti-Fe	Ti-Ni
Crystallite size (nm)	38	44	49	50	45	48
Anatase phase content (%)	92	91	90	90	90	90
Rutile phase content (%)	8	9	10	10	10	10
Ionic radius of Impregnated metal (Å)	-	1.26	0.74	0.72	0.64	0.72
Colour of catalyst	White	White	Light Green	Light Yellow	Light Yellow	Light Pink

2.3.2. Surface area analysis (N₂ adsorption)

Specific surface area, pore volume and pore size distributions of calcined catalysts were determined from N₂ adsorption-desorption isotherms at 77K by ASAP 2010,

Micromeritics, USA. Surface area and pore size distribution were determined using the BET equation and BJH method respectively [58]. The catalysts were degassed under vacuum (10^{-2} Torr) at 393 K for 4 h, prior to measurement. The catalysts NPC-393 and NPC-583 were degassed at 373K and 573K respectively for two hours where as the catalysts NPC-626, NPC-673, NCT-713, NPC-753, NPC-833, NPC-913, NPC-1023 and P25 Degussa were degassed at 623K for two hours. Calcination at higher temperature significantly affects the textural properties of nanocrystalline TiO₂. The surface area and pore volume of nanocrystalline TiO₂ calcined at various temperatures and P25 is given in Table 2.3. The synthesised amorphous TiO₂ catalyst NPC-393 had the highest surface area of 259 m²g⁻¹ whereas the anatase TiO₂, NPC-833 had surface area of 91 m²g⁻¹. The surface area of NPC-913 and NPC-1023 catalysts reduced to 2 m²g⁻¹ for NPC-913 and NPC-1023 with increase in the calcination temperature. The sharp decrease in pore volume was obtained at 913K reflects sintering, and the formation of densely packed crystalline structure of nanocrystalline TiO₂. The highest pore diameter of 76 Å was observed for NPC-833 that reduced to 73 Å and 54 Å respectively for NPC-913 and NPC-1023 catalysts. This may be the indication of complete phase transition from anatase to rutile phase for NPC-1023.

Table 2.3: Textural properties of nanocrystalline TiO₂ calcined at different temperatures.

Catalysts	Degassing Temperature (K)	BET surface area (m ² /g)	Average pore volume (cm ³ /g)	Average pore Diameter (Å)
NPC-393	373	259	0.310	48
NPC-583	573	199	0.300	61
NPC-628	623	174	0.290	65
NPC-673	623	166	0.280	67
NPC-713	623	145	0.270	72
NPC-753	623	124	0.230	75
NPC-833	623	091	0.170	76
NPC-913	623	002	0.004	73
NPC-1023	623	002	0.005	54
P25	623	061	0.120	82

The pore size distribution for nanocrystalline TiO₂ calcined at various temperatures is shown in Figure 2.5. The distribution curve showed that the nanocrystalline catalysts were having narrower pore size distribution and increased with temperature.

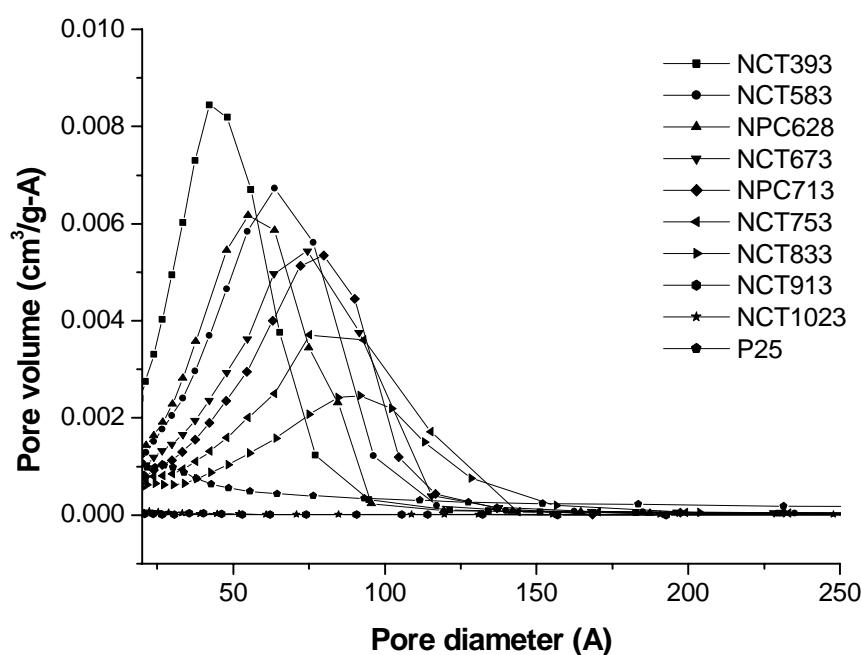


Figure 2.5: Pore size distribution for nanocrystalline TiO₂ calcined at various temperatures.

Figure 2.6 shows the pore size distribution curve and the corresponding nitrogen adsorption-desorption isotherms (insert) of MT-10. The BET surface area and pore parameters from nitrogen adsorption-desorption isotherms (Barret-Jooyner-Halenda method) of catalysts synthesized by Method-B are summarised in Table 2.4. The data of N₂ sorption study in Table 2.4 shows that the impregnations of metal on MT-10 had reduced the surface area by 6-12 m²g⁻¹ in various catalysts. The reduced surface area and increased pore volume confirmed the impregnation of metal on TiO₂. There was no change observed in the shape of isotherm plot after metal impregnation on nanocrystalline TiO₂. The average pore diameter of metal impregnated catalyst was between ca. 11-14 nm. The lowest and highest surface area was obtained for cobalt (26 m²g⁻¹) and silver (32 m²g⁻¹) impregnated catalysts respectively.

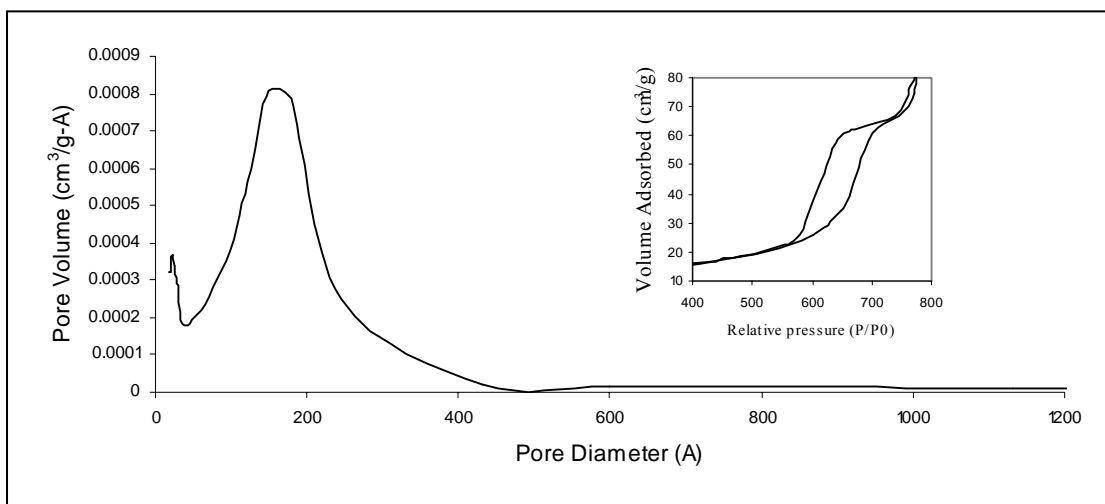


Figure 2.6: Isotherm plot (inset) & Pore size distribution of MT-10.

Table 2.4: Textural properties of metal ion impregnated catalysts

Catalyst	MT-10	Ti-Ag	Ti-Co	Ti-Cu	Ti-Fe	Ti-Ni
BET Surface Area (m^2g^{-1})	38	32	26	27	31	30
Pore diameter (Å)	112	132	132	137	128	139
Ionic radius of impregnated metal (Å)	-	1.26	0.74	0.72	0.64	0.72
Work function of metal	-	4.73	5.00	4.70	4.50	5.15

2.3.3. Diffuse Reflectance Spectroscopy

The bandgap of the nanocrystalline TiO_2 catalysts calcined at various temperatures were determined using the Diffuse Reflectance Spectroscopy (DRS) (*Shimadzu UV-3101PC with DRS Model no. ISR-3100*) equipped with an integrating sphere at room temperature in the wavelength range of 250-600nm. All spectra were recorded with BaSO_4 as a reference [46-47].

The DRS spectra of nanocrystalline TiO_2 catalysts calcined at various temperatures are shown in Figure 2.7. A shift of 21 nm toward longer wavelength was observed for NPC-1023 nanocrystalline TiO_2 compared to that for NPC-393.

A differential calculation on all curves of Figure 2.7 was done to determine the band edges of the catalysts which is as shown in Figure 2.8. The band edges of the catalysts determined from differentiation of absorption curves of Figure 2.8 were tabulated in Table 2.5.

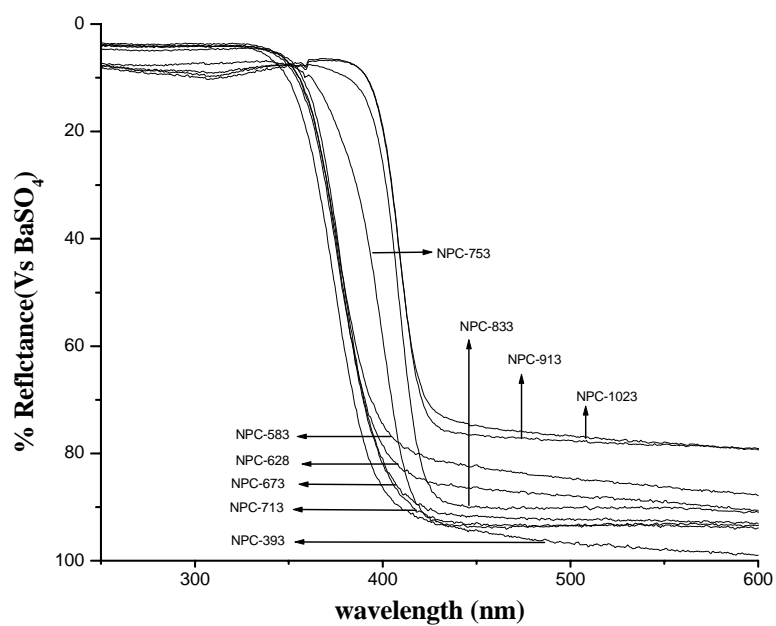


Figure 2.7: DRS spectra of nanocrystalline TiO_2 catalysts calcined at various temperatures.

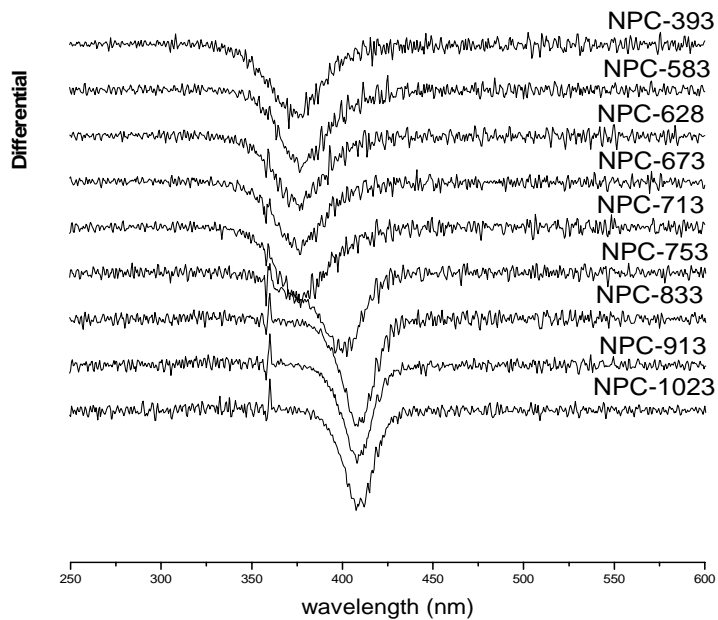


Figure 2.8: Differential spectra of DRS of nanocrystalline TiO_2 catalysts calcined at various temperatures

The bandgaps of nanocrystalline TiO₂ catalysts tabulated in Table 2.5 was calculated using the following Equation 2.3 [46, 47].

$$E_g \text{ (eV)} = 1240/\lambda_g \quad \text{Equation 2.3}$$

where absorption edge is λ_g and the bandgap E_g in eV.

Table 2.5: Bandgap of nanocrystalline TiO₂ catalysts calcined at various temperatures

Catalysts	Crystallite size of anatase (nm)	Band edge (nm)	Bandgap (eV)
NPC-393	08	376.5	3.29
NPC-583	09	376.5	3.29
NPC-628	10	377.0	3.28
NPC-673	12	377.0	3.28
NPC-713	13	385.0	3.22
NPC-753	14	400.0	3.10
NPC-833	19	410.0	3.02
NPC-913	29	411.0	3.01
NPC-1023	-	412.0	3.01
P25	28	393.5	3.15

The bandgap of nanocrystalline catalyst NPC-393 was 3.29 eV. On increase in calcination temperature, the amorphous TiO₂ converted to anatase phase and the bandgap decreased from 3.29 at 393K to 3.02 eV at 833K. The bandgap of nanocrystalline TiO₂ catalysts prepared at temperature 833K and that of P25 which had crystallite sizes of 16 and 28 nm respectively were 3.02 and 3.15 eV showing that the change in bandgap is due to the change in crystallite size. The crystallite size of nanocrystalline TiO₂ increased with increase in calcination temperature which results in the decrease of bandgap.

The smaller bandgap values indicated the relative densely packed crystalline structures [54]. The bandgap of the amorphous TiO₂ synthesized by Method A was 3.29 eV. The data in Table 2.5 evidenced that the bandgap depends upon the crystallite size which decreased with an increase in crystallite size. The bandgap of

NPC-1023 nanocrystalline TiO_2 catalyst was 3.01 eV and contains only the rutile phase.

The DRS spectra of the catalysts synthesized by impregnation of different metal ions on TiO_2 as per Method B are shown in Figure 2.9. The changes in the DRS spectrum for various metal impregnated catalysts may be attributed to the change in the bandgap of TiO_2 . The shift towards longer wavelength of 1.5 nm for Fe and 11 nm for Ni confirms that the change in bandgap depends upon the metal ion loaded on TiO_2 . The differentials of DRS spectra of metal impregnated nanocrystalline TiO_2 catalysts are shown in Figure 2.10.

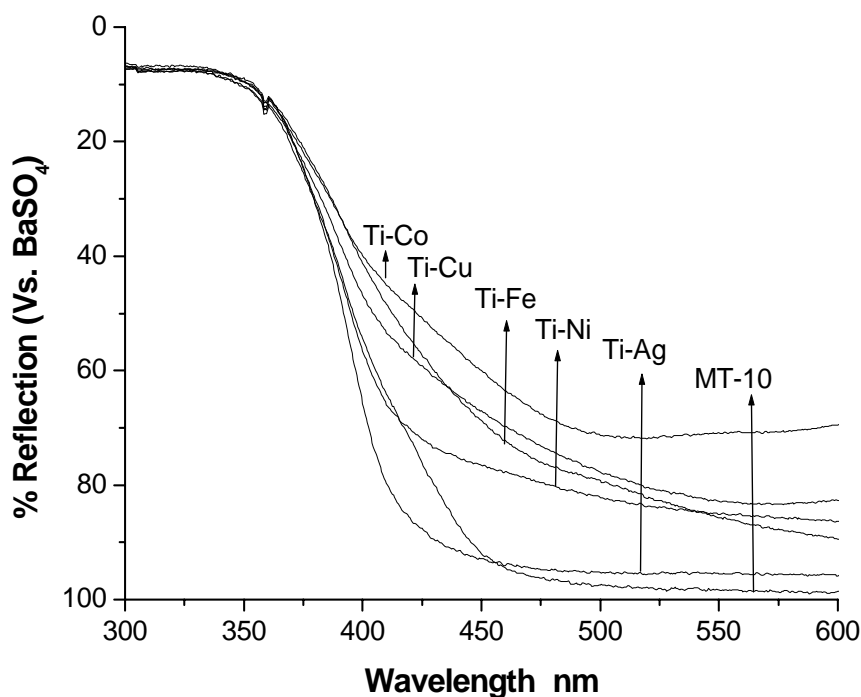


Figure 2.9: DRS spectra of metal ion impregnated catalysts.

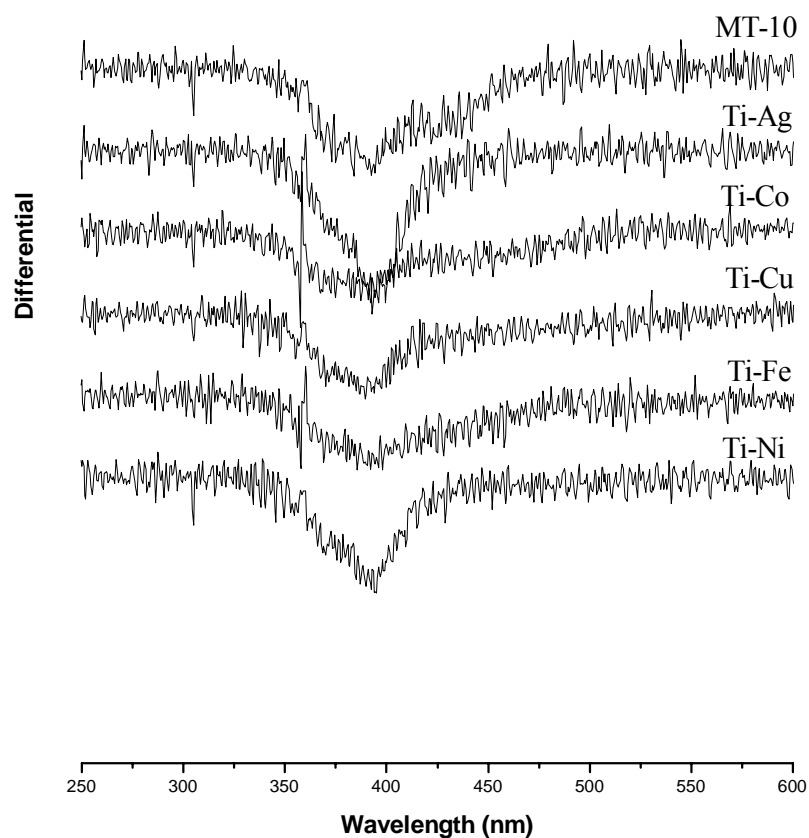


Figure 2.10: Differential spectra of DRS of metal ion impregnated catalysts.

The band edge position and bandgap of the catalysts were found from Figure 2.10 and are given in Table 2.6.

Table 2.6: Band edge positions and Bandgaps of metal ion impregnated catalysts

Catalyst	Band edge (nm)	Red shift (nm)	Bandgap (eV)
MT-10	384	-	3.229
Ti-Ag	393	09.0	3.155
Ti-Co	392	10.0	3.163
Ti-Cu	389.5	05.5	3.183
Ti-Fe	385.5	01.5	3.216
Ti-Ni	395	11.0	3.139

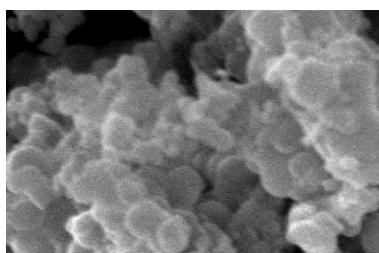
2.3.4. Scanning Electron Microscopy (SEM)

The surface morphology of the catalysts calcined at different temperatures was determined with scanning electron microscope (Leo Series 1430 VP) equipped with INCA, Energy Dispersive System (EDX). The catalysts were supported on aluminium stubs using silver paint and then sputter coated with gold (by using Polaris Sputter Coater, Model Polaron SC7620, Quantum Technologies). The scanning electron micrographs show that the photocatalysts are having nearly spherical shape. Figures 2.11 and 2.12 show the scanning electron micrographs of the catalyst synthesized by both Method A and Method B. There was no significant change observed in metal impregnated catalysts micrograph images.

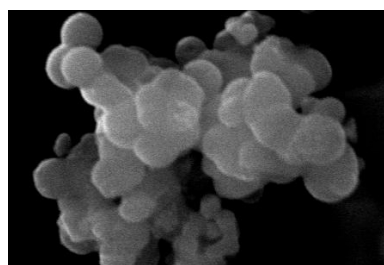
For metal ion impregnated semiconductor catalyst, the surface elemental analysis was done by Energy Dispersive System (EDX) analysis (Table 2.7) confirmed the presence of impregnation of metal on MT-10. The indicated amount of metal percentages given in Table 2.7 for all catalysts agrees with the metal impregnation on bare TiO₂ catalyst.

Table 2.7: EDX results of metal ion impregnated TiO₂ catalysts

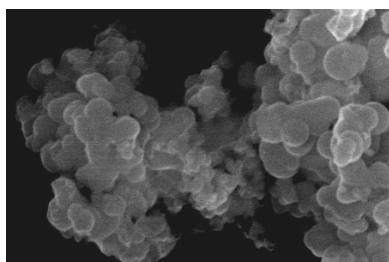
Catalyst	Weight % (Ti)	Weight % (O)	Weight % (Impregnated metal)
MT-10	63.63	36.37	0.00
Ti-Ag	52.75	46.74	0.51
Ti-Co	54.65	44.71	0.64
Ti-Cu	67.77	31.79	0.44
Ti-Fe	59.87	39.86	0.47
Ti-Ni	69.13	30.35	0.52



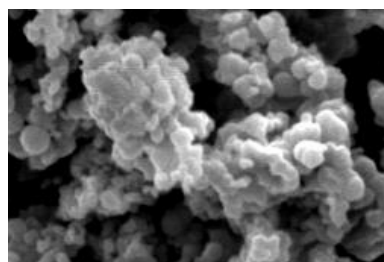
Dried at 393K



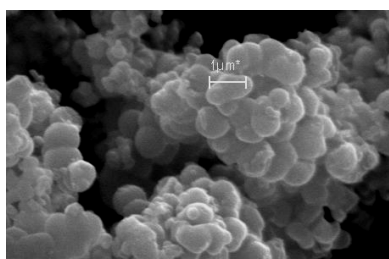
Calcined at 753K



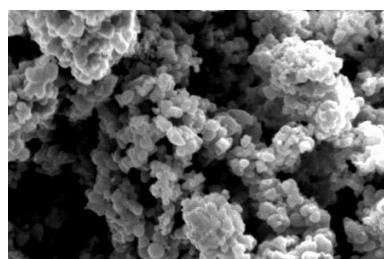
Calcination at 583K



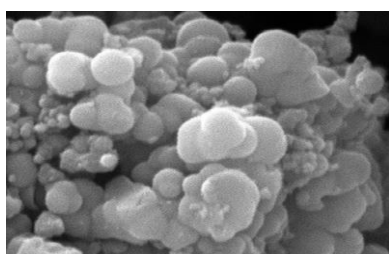
Calcined at 833K



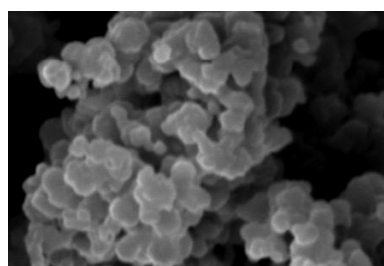
Calcined at 673K



Calcined at 913K

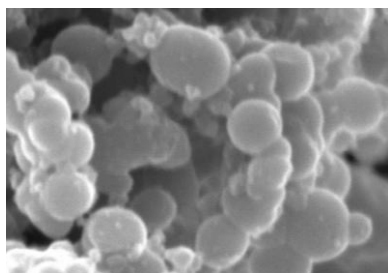


Calcined at 713K

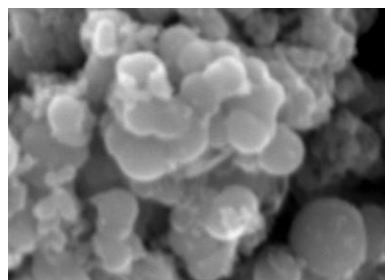


Calcined at 1023K

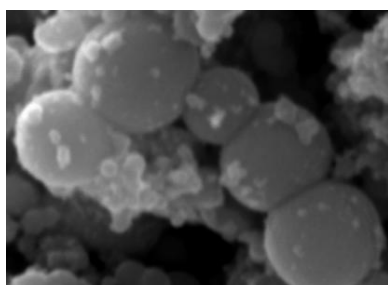
Figure 2.11: SEM images of nanocrystalline TiO₂ prepared by Method A.



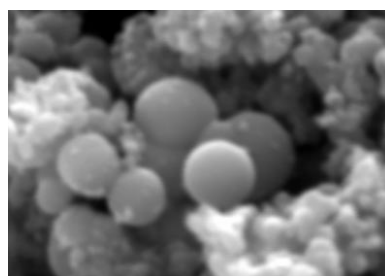
Ti-Ag



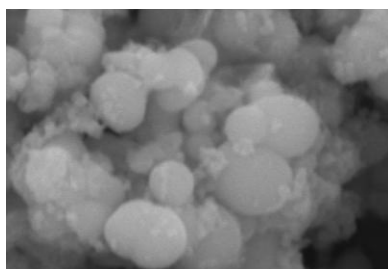
Ti-Fe



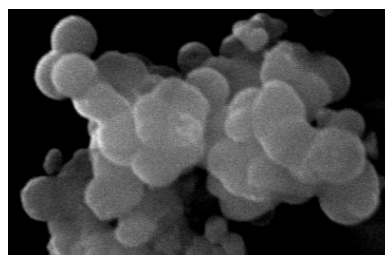
Ti-Co



Ti-Ni



Ti-Cu



MT-10

Figure 12: SEM images of nanocrystalline TiO₂ prepared by Method B.

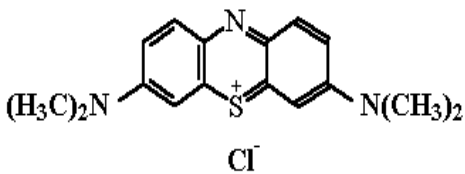
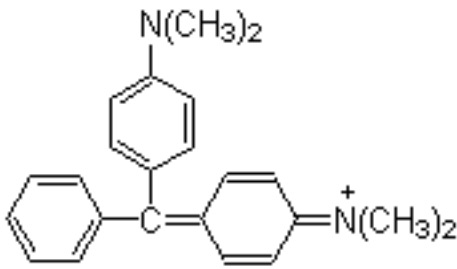
2.4. Photocatalytic degradation of dyes

In this section, the photocatalytic degradation of dyes with the catalysts synthesized by both Method A and Method B is presented.

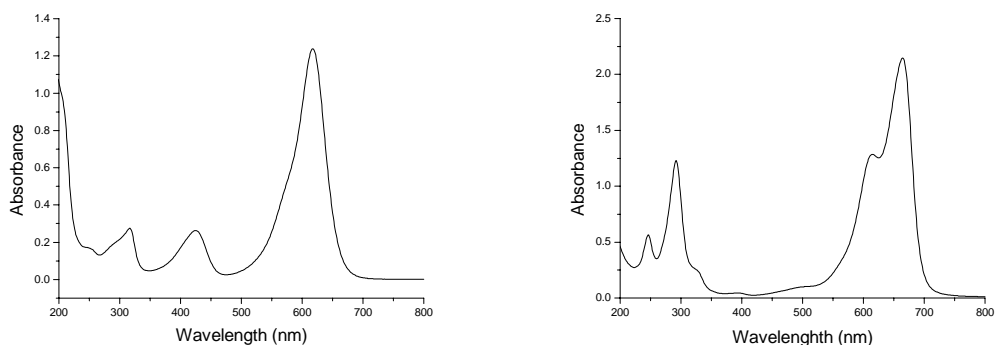
2.4.1. Dye compounds and their characteristic properties

To study the photocatalytic degradation activity of the synthesised photocatalysts, two dyes were randomly selected. These dyes were Methylene Blue (MB) and Malachite Green (MG). These two dyes are mainly found in the effluents of textile industries. The molecular structure and chemical properties of these two dyes are given in Table 2.8.

Table 2.8: Molecular structure and chemical properties of dyes

 <p>a) Methylene Blue</p>	<p>Molecular Weight: 319.86</p> <p>Chemical Formula: $C_{16}H_{18}ClN_3S$</p> <p>Solubility in water 3.55%</p> <p>Absorption maximum 644 nm</p> <p>Class Thiazin</p>
 <p>b) Malachite Green</p>	<p>Molecular Weight: 927.02</p> <p>Chemical Formula: $C_{22}H_{24}N_4O_2$</p> <p>Solubility in water Very</p> <p>Absorption maximum 628 nm</p> <p>Class Triarylmethane</p>

The UV-Visible absorption spectra of MB and MG dyes are shown in Figure 2.13. These spectra were recorded for both dyes with 50 ppm each but diluted five times to get spectra obeying Beer-Lambert Law. The absorbance maxima of MB and MG are 644 nm and 628 nm respectively.

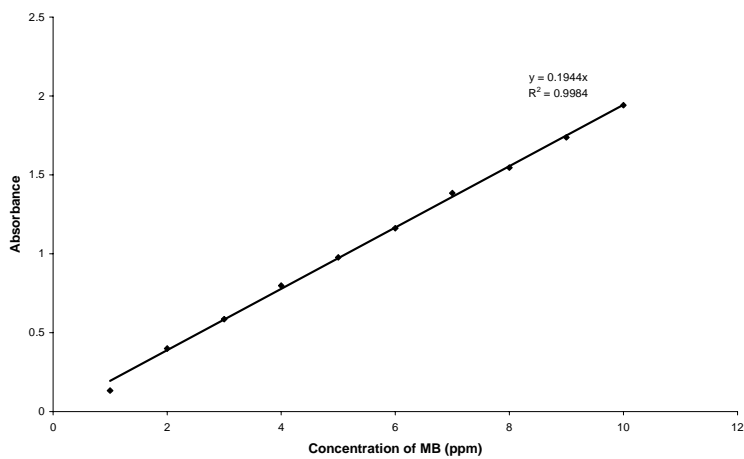


a) Methylene Blue

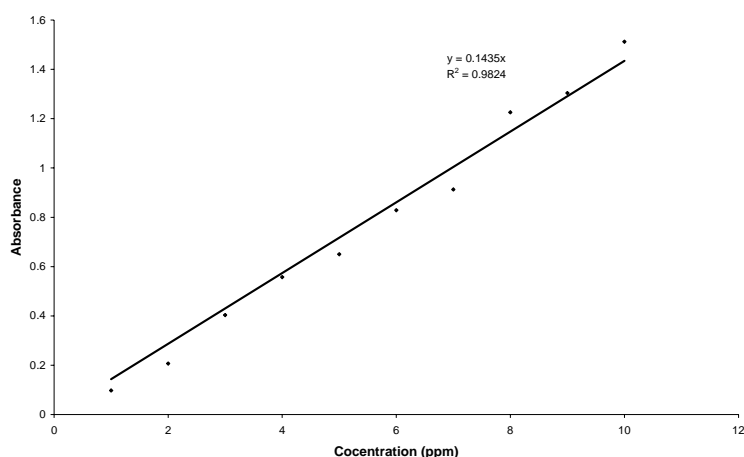
b) Malachite green

Figure 2.13: UV-Vis absorption spectra of a) Methylene Blue b) Malachite green (5 times diluted)

The calibration curves for both these dyes were recorded by using the known concentrations of these dyes from 0-15 ppm. The calibration curves for both the dyes are shown in Figure 2.14.



(a) Calibration curve of MB



(b) Calibration curve of MG

Figure 2.14: Calibration curves of dyes for known concentrations (a) MB (b) MG

The equations (Equation 2.4 and 2.5) obtained from the calibration curve were used to find out the amount of dye present in the photodegraded solution.

$$\text{For MB} \quad y = 0.1944 x \quad \text{Equation 2.4}$$

$$\text{For MG} \quad y = 0.1435 x \quad \text{Equation 2.5}$$

where x is the concentration of the dye and y (644nm, 628 nm) is characteristic maximum absorbance of the MB and MG dyes respectively.

2.4.2. Photocatalytic degradation setup

The photocatalytic degradation setup comprised a reactor which was designed and fabricated. The line sketch of photocatalytic reactor is shown in Figure 2.15. It consisted of a glass vessel where the solution to be degraded was placed. This glass vessel housed a double wall quartz vessel to hold the irradiation source. This double wall jacketed quartz vessel had two lines, one for inlet and another for outlet of water for cooling the irradiation source. The irradiation source was 125-watt mercury vapour lamp. The wavelength of irradiation of mercury vapour lamp was in the range of 200-400 nm. The irradiation source was indirectly cooled by circulating water to 303K during experiments.

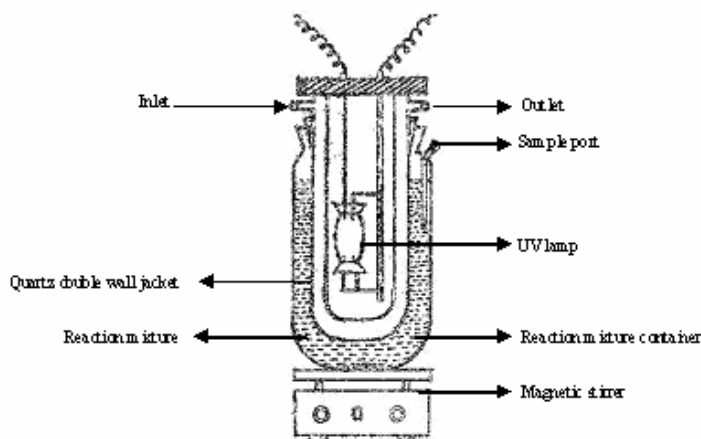


Figure 2.15: Sketch of photocatalytic reactor.

2.4.3. Photocatalytic Experimental Study

Photocatalytic degradation experimental studies of MB, MG, AP, and NB under UV light irradiation were done by determining the spectroscopic absorption and COD measurements.

2.4.3.1. Spectroscopic Absorption Measurements

The Photocatalytic experimental studies were done using UV-Visible Spectrophotometer (*Varian Cary 500*). The absorption spectrum of the periodically photocatalytic degraded dye solutions were recorded in the range of 200-800 nm. The decrease in the absorbance value for dye solutions were used as the deterministic parameter for the degradation of dyes. The decrease in the absorbance maxima corresponds to a decrease in the dye concentration.

2.4.3.2. Chemical Oxygen Demand (COD) Measurements

Chemical Oxygen Demand (COD) of the dye was measured by using *SPECTROQUANT NOVA 60* Photometer. COD value determines the presence of any organic compounds, dyes in the present study. Higher the COD value, higher is the concentration of dye in the solution and vice-a-versa. The reagent solutions used in the study were Standard COD solution A (No. 1.14538, 0.3 ml) and Standard COD solution B (No. 1.14681 or 1.14682, 2.85 ml) for COD analysis. A 3 ml of the

reaction solution degraded at periodic intervals were mixed with reagents in glass cells and digested in Thermodigester (*Spectroquant TR 320*) for two hours at 148°C. After digestion, mixture was cooled to room temperature and the COD was measured using the photometer.

2.4.4. Photocatalytic Degradation Procedure

The photocatalytic experiments were carried out for four hours to determine the photocatalytic activity of all the synthesized catalysts. Prior to commencing illumination, a suspension containing 50 mg of the catalyst and 250 ml aqueous solution of about 50 ppm of dye was taken in glass vessel of the reactor. The dye suspension was continuously stirred for 30 minutes in the dark for adsorption of dye on the catalyst. At each interval of 10 minutes, for first one hour and then after every one hour, a 10ml of reaction solution was withdrawn by syringe from the irradiated suspension. The catalyst was separated by centrifuge from the reaction solution prior to analysis. The concentration of dye in the reaction solution was determined by spectrophotometer from the Equation 2.4 & 2.5 obtained from the calibration curve Figure 2.14. The 50 ppm concentration of dye was used as the initial value for the measurement of degradation of dye.

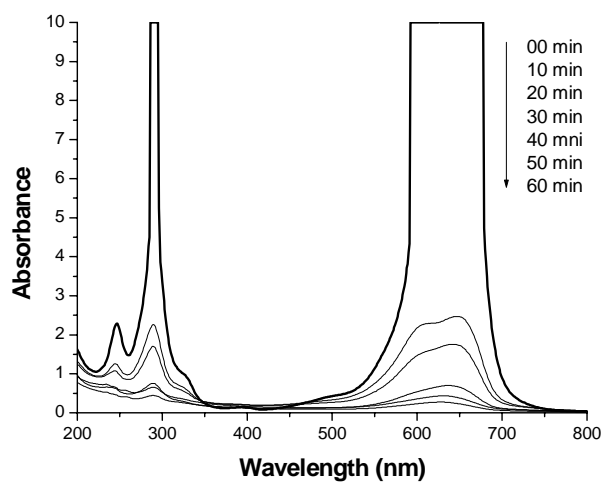
2.4.5. Photocatalytic Degradation Studies

In the following sections, the photocatalytic activity of all the catalysts synthesised by Method A and Method B is discussed.

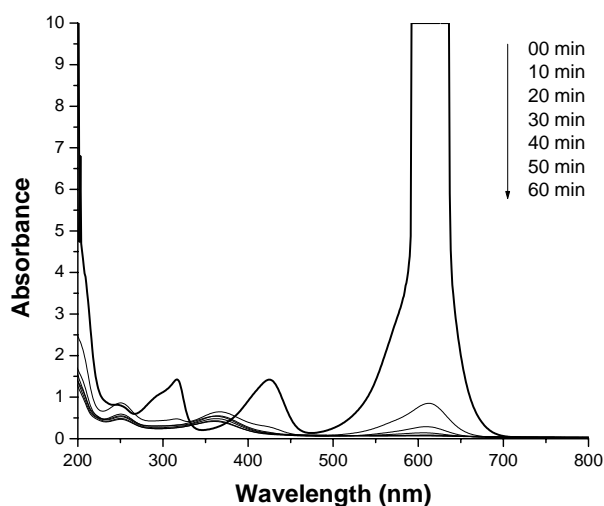
2.4.5.1. Photocatalytic Degradation studies by Catalysts Prepared by Method A

The photocatalytic activity of catalysts synthesized by Method A was investigated by studying the degradation MB and MG dyes. The irradiation experiments using each catalyst was carried out for four hours to determine the photocatalytic activity of the catalysts. UV-Visible absorption spectra were recorded after the irradiation of UV light on the solution of dyes at various intervals of time. The absorption spectrum of both the photodegraded dyes using NPC-583 catalyst is as shown in Figure 2.16. The

photocatalytic activity of all catalysts was indicated by a decrease in the concentration of both the dyes as shown in Figure 2.17. The catalyst NPC-753 showed good photocatalytic activity for degradation of both dyes. The complete degradation of both dyes took place in around 50 minutes with NPC-753 catalyst where 100% visible decolourization was observed in two hours. There was no additional peak observed with degradation of dyes for any of the catalyst. The photocatalytic activity of all catalysts was observed to be different for the two studied dyes.

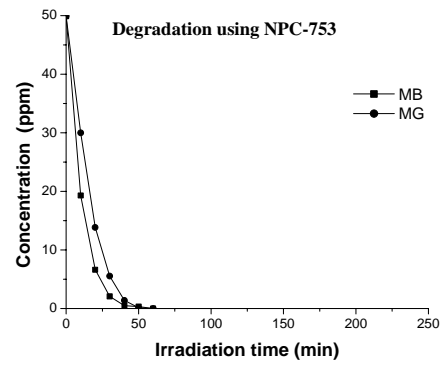
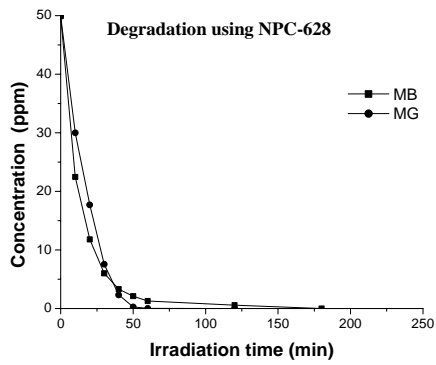
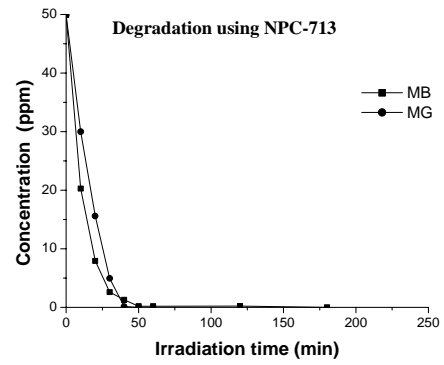
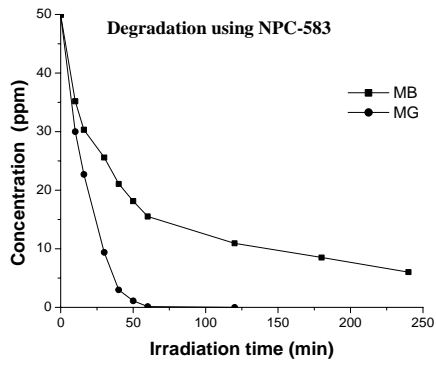
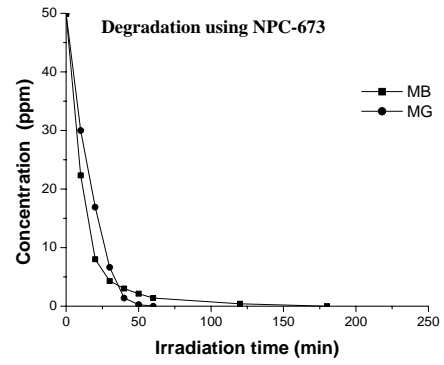
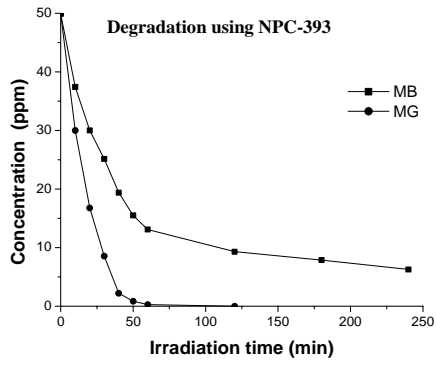


(a) MB degradation using NPC-583



b) MG using NPC-583

Figure 2.16: UV-Visible absorption spectra recorded after irradiation of UV light using NPC-583 at various intervals of time (a) MB (b) MG



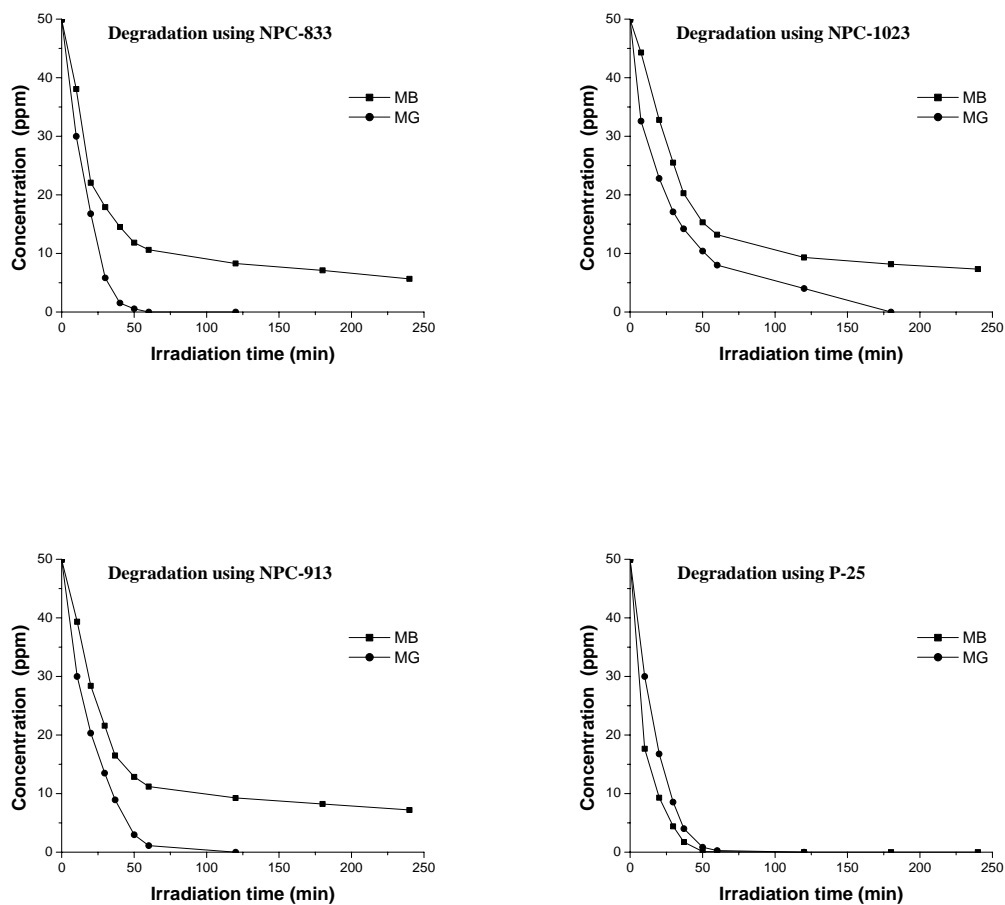


Figure 2.17: Degradation of MB and MG using catalysts calcined at various temperatures

The COD values were also measured for dye solutions degraded for 1-4 hours with all catalysts which are tabulated in Table 2.9. It is understood from this table that the dyes photodegraded with NPC-753 had the lowest measured COD in minimum time of 2 hours for both dyes which eventually dropped to zero in 3 hours. COD also zeroed in 3 hours with some catalysts while some took 4 hours. In case of NPC-1023 catalyst the COD did not levelled to zero during the 4 hours degradation studies.

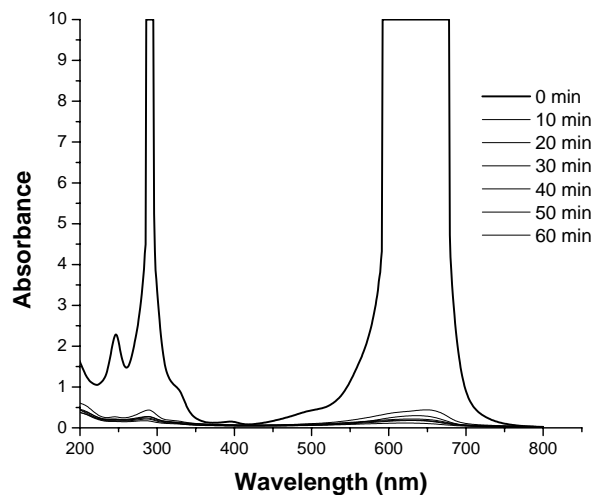
Table 2.9: COD of reaction mixture of dyes using synthesized catalysts

Catalyst	COD of reaction mixture of dyes w.r.t. irradiation time (mg/L)							
	MB (Initial COD= 65 mg/L)				MG (Initial COD=75 g/L)			
	1 Hr	2 Hrs	3 Hrs	4 Hrs	1 Hr	2 Hrs	3 Hrs	4 Hrs
NPC-393	18	16	14	00	19	08	00	00
NPC-583	23	18	12	00	18	08	00	00
NPC-628	12	08	00	00	16	07	00	00
NPC-673	09	06	00	00	14	06	00	00
NPC-713	08	06	00	00	14	06	00	00
NPC-753	08	05	00	00	12	04	00	00
NPC-833	18	14	08	00	15	08	00	00
NPC-913	20	16	10	08	18	12	08	00
NPC-1023	22	16	12	08	20	16	10	04
P-25	10	07	00	00	10	06	00	00

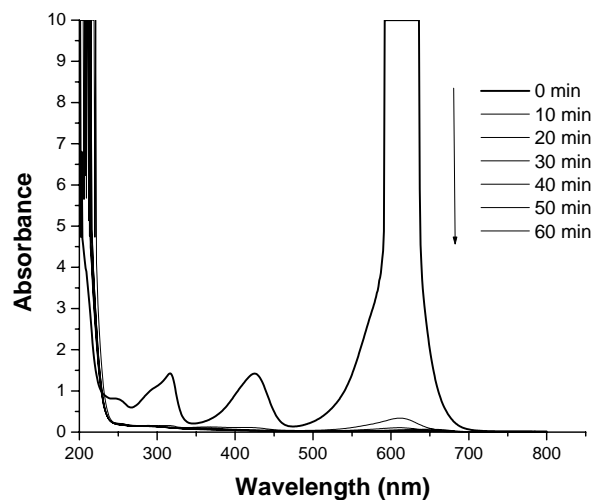
2.4.5.2. Photocatalytic Degradation studies by Catalysts prepared by Method B

The photoactivity of catalysts synthesized by Method B was similarly investigated by studying the degradation MB and MG dyes. The same experimental procedure was followed as described in 2.4.4.1 for photodegradation of both dyes and absorbance measurements. The absorption spectrum of both photodegraded dyes using Ti-Ag catalyst are shown in Figure 2.18. The photocatalytic activity of all catalysts was indicated by a decrease in the concentration of both the dyes as shown in Figure 2.19. Among the metal impregnated catalysts, the highest initial rate of degradation of MB was obtained for Ti-Ag while for MG it was same and also it was higher when photodegraded by Ti-Ag, Ti-Cu and Ti-Ni as compared to MT-10. The complete degradation of MG dye took place in around 60 minutes with Ti-Ag catalyst and 120 minutes for MB followed by 100% visible decolourization in two hours. There was no additional peak observed with degradation of dyes for any of the catalyst. All catalysts

showed varying photocatalytic activity for different metal ions impregnated on the surface of the catalysts as shown in Figure 2.19 for various intervals of time.



(a) MB degradation using Ti-Ag



(b) MG degradation using Ti-Ag

Figure 2.18: UV-Visible absorption spectra recorded after irradiation of UV light using Ti-Ag at various intervals of time (a) MB (b) MG.

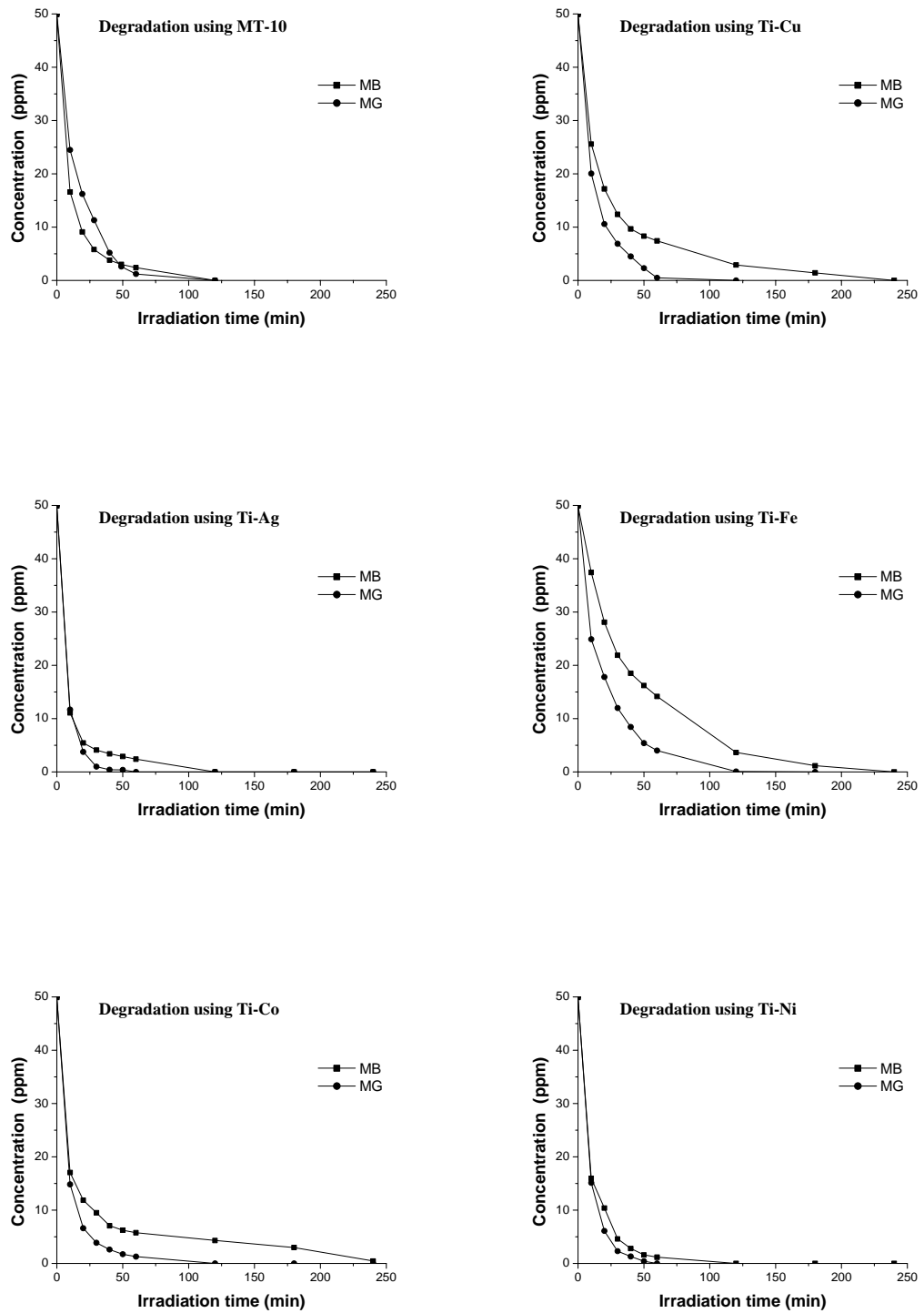


Figure 2.19: Degradation of dyes using catalysts prepared by Method B.

Similarly, the COD values were recorded for dye solutions degraded from 1-4 hours as tabulated in Table 2.10. The maximum red shift was observed in Ti-Ag catalyst and hence higher photocatalytic activity was obtained which resulted in the lowest COD with Ti-Ag for both dyes within 2 hours.

Table 2.10: COD of reaction mixture of dyes using synthesized catalysts.

Catalyst	COD of reaction mixture of dyes w.r.t. irradiation time (mg/L)							
	MB (Initial COD= 65 mg/L)				MG (Initial COD=75 g/L)			
	1 Hr	2 Hrs	3 Hrs	4 Hrs	1 Hr	2 Hrs	3 Hrs	4 Hrs
MT-10	08	06	00	00	10	08	00	00
Ti-Ag	06	00	00	00	08	00	00	00
Ti-Fe	12	10	06	00	10	08	04	00
Ti-Co	14	11	08	00	15	09	06	00
Ti-Cu	14	12	07	00	09	06	03	00
Ti-Ni	07	04	00	00	09	05	00	00

2.5. Photocatalytic Degradation of Organic Compounds

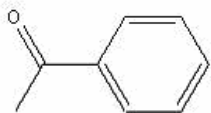
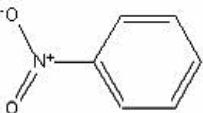
In this section, the photocatalytic degradation of organic compounds for all the catalysts synthesized by both Method A and Method B are presented.

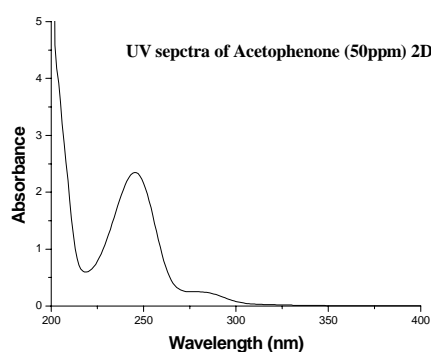
2.5.1. Organic Compounds and their Characteristic Properties

To study the photocatalytic degradation activity of the synthesised photocatalysts two organic compounds were randomly selected. These were Acetophenone (AP) and Nitrobenzene (NB). These two compounds show considerably low reactivity towards bio-chemical and chemical oxidation. NB is a pale yellow liquid with odour of bitter almonds and is toxic in nature. Its solubility in water is 1900 mgL^{-1} at 20°C . NB is primarily used in the production of aniline and aniline derivatives, such as methyl diphenyl diisocyanate (MDI). However, it also finds use in the manufacturing of rubber chemicals, pesticides, dyes, and pharmaceuticals [59]. NB is also used in shoe

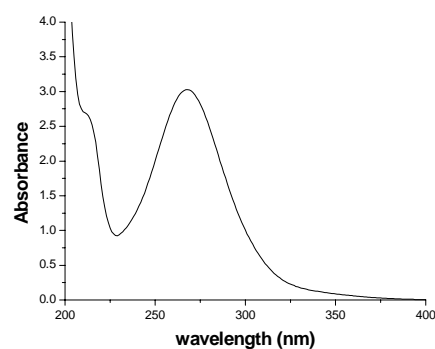
and floor polishes, leather dressings and paint solvents and is also used in the production of the analgesic acetaminophen. The removal of NB from aqueous effluent is done by highly energy intensive incineration. In the present study, it is attempted to reduce NB from such an aqueous effluents by photocatalysis. The molecular structure and chemical properties of these two compounds are given in Table 2.11 and Figure 20 show the UV-Vis absorption spectrum of AP and NB.

Table 2.11: Molecular structure and chemical properties of organic compounds AP and NB

 <p>a) Acetophenone (AP)</p>	Molecular Weight	120.15
	Chemical Formula	C ₈ H ₈ O
	Absorption maximum	232 nm
	Colour	Colourless
 <p>b) Nitrobenzene (NB)</p>	Molecular Weight	123.11
	Chemical Formula	C ₆ H ₅ NO ₂
	Absorption maximum	268 nm
	Colour	Colourless to pale yellow



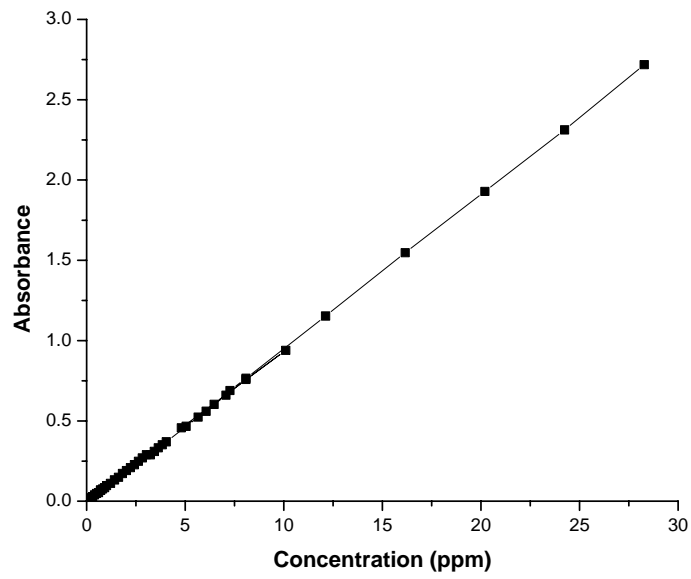
(a) AP



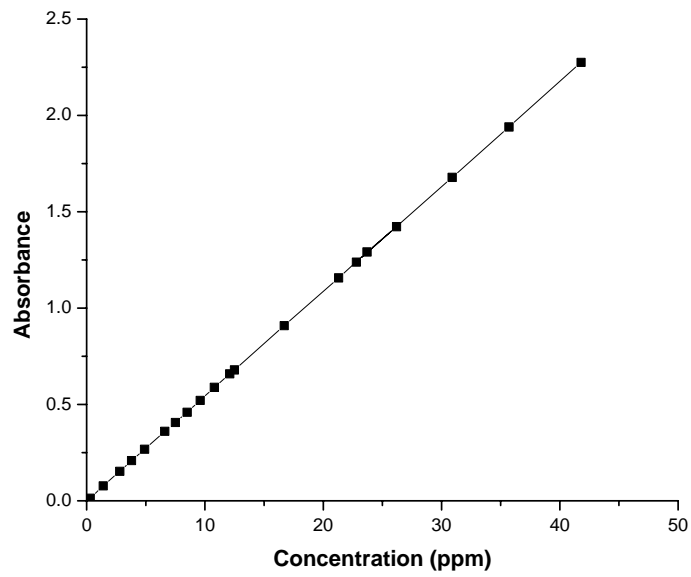
(b) NB

Figure 2.20: UV-Vis absorption spectra of (a) AP and (b) NB

The calibration curve for both of these organic compounds were recorded by using known concentrations from 0-30 ppm for AP and 0-50 ppm for NB. The calibration curves are shown in Figure 2.21.



(a) Calibration curve of AP



(b) Calibration curve of NB

Figure 2.21 Calibration curves of known concentrations of (a) AP and (b) NB

The equations (Equation 2.6 and 2.7) obtained from the calibration curve were used to find out the amount of organic compound present in the solution.

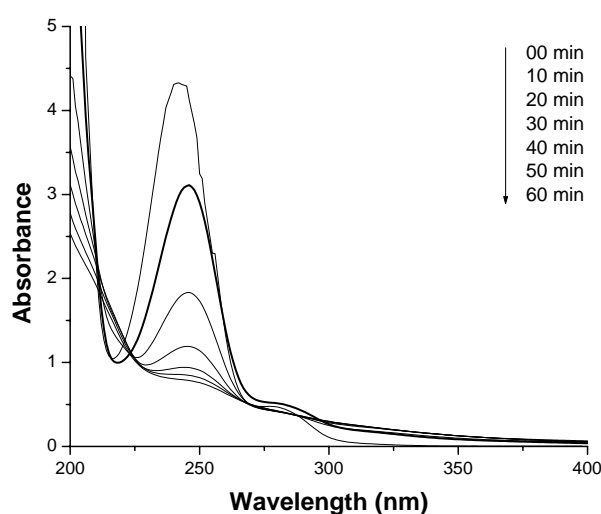
$$\text{For AP} \quad y = 0.0952 x \quad \text{Equation 2.6}$$

$$\text{For NB} \quad y = 0.0544 x \quad \text{Equation 2.7}$$

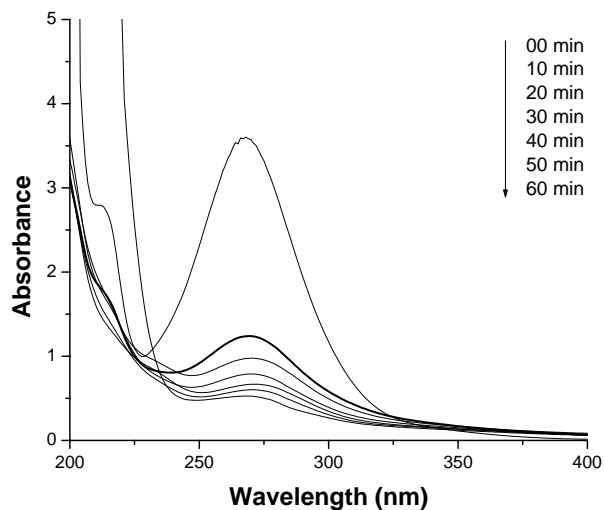
where x , is the concentration of the AP and NB and y is characteristic maximum absorbance of the AP (232 nm) and NB (268 nm) respectively.

2.5.2. Photocatalytic Degradation studies by Catalysts Prepared by Method A

The photocatalytic degradation setup, photodegradation procedure, experimental study and photocatalytic activity measurements were carried out by the same procedure as discussed in 2.4.2 to 2.4.5. The absorbance spectra of both photodegraded AP and NB using NPC-753 catalyst with respect to time from 0-60 min are given in Figure 2.22. The synthesised NPC-753 had shown the highest photocatalytic activity among all the catalysts towards degradation of both the compounds. The graph of concentration verses time for degradation of AP and NB using all catalysts are given in Figure 2.23. The complete degradation of AP with catalyst NPC-753 took 4 hours. The degradation of NB was slow as compared to AP.

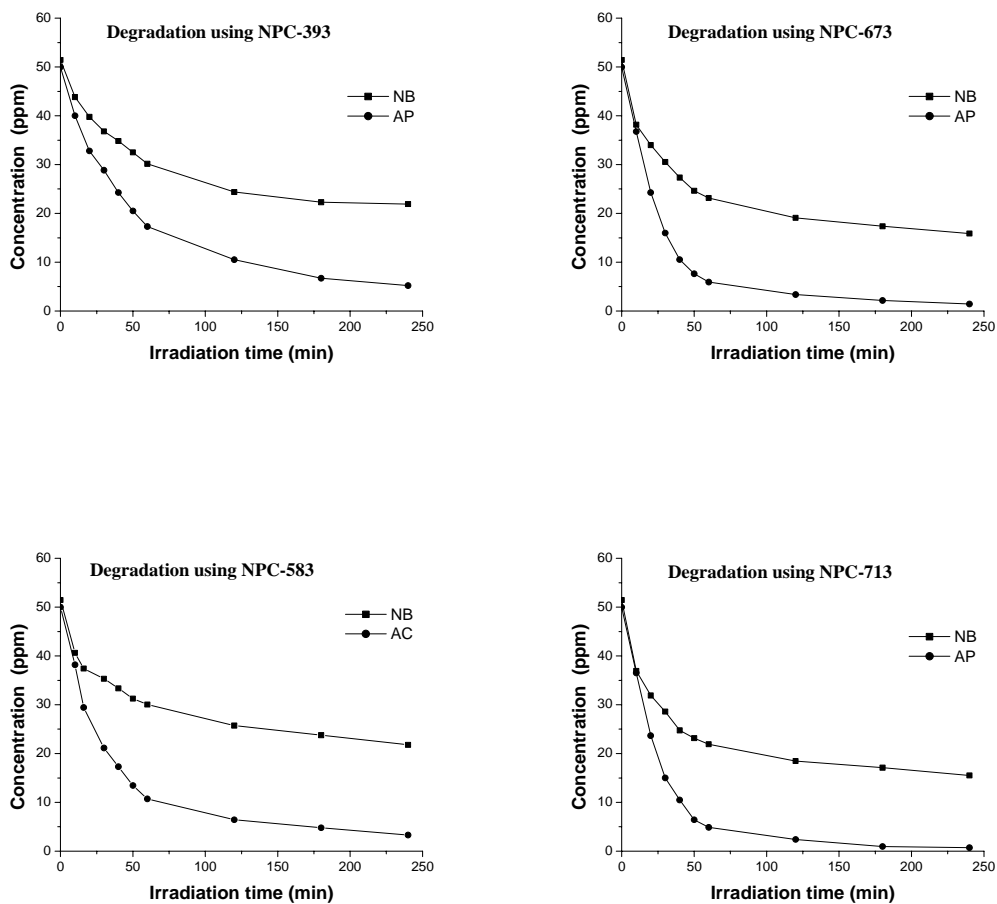


(a) Degradation of AP using NPC-753



(b) Degradation of Nitrobenzene using NPC-753

Figure 2.22: UV-Vis absorption spectra of degradation of a) AP and b) NB using NPC-753.



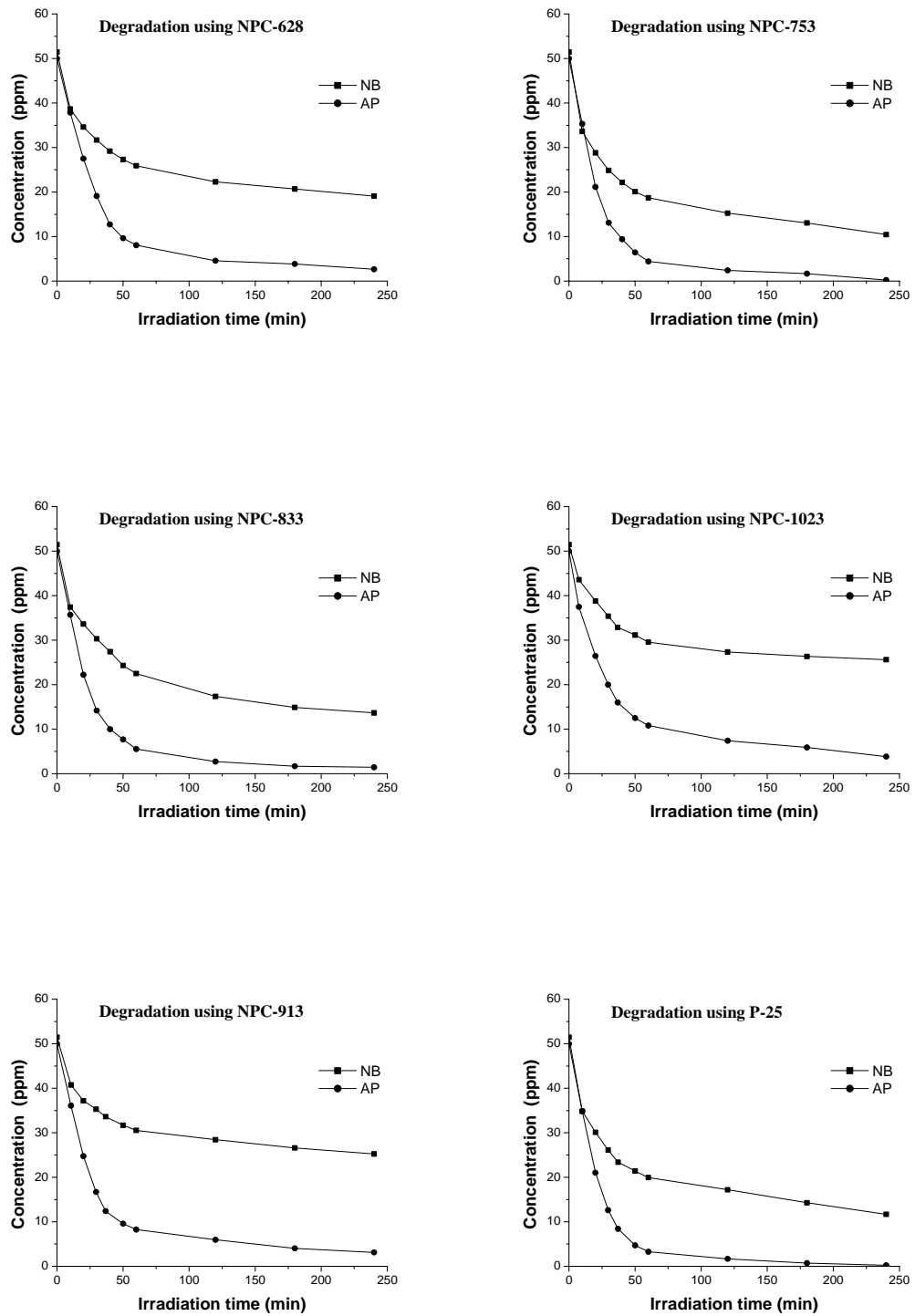


Figure 2.23: Degradation of NB and AP using semiconductor photocatalyst calcined at various temperatures under UV light with respect to time.

The COD values were also measured for organic solutions degraded for 1-4 hours with all catalysts which are as shown in Table 2.11. It is understood from this table that the organic compounds photodegraded with NPC-753 had the lowest measured COD in 4 hours duration.

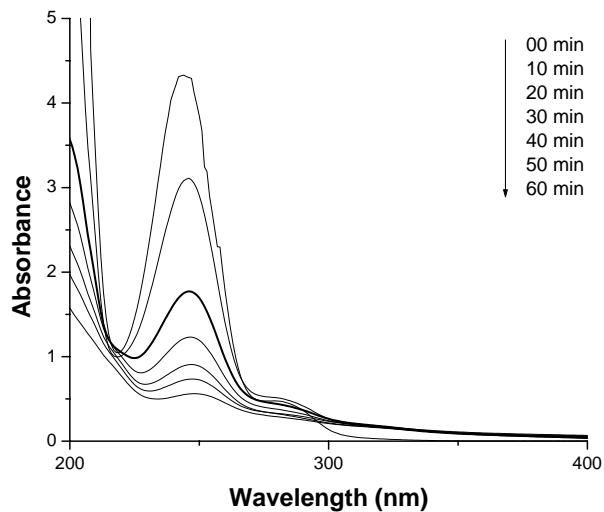
Table 2.11: COD of reaction mixture of AP and NB using synthesized catalysts.

Catalyst	COD of reaction mixture of AP and NB with respect to irradiation time (mg/L)							
	Acetophenone (Initial COD= 120 mg/L)				Nitrobenzene (Initial COD= 90 mg/L)			
	1 Hr	2 Hrs	3 Hrs	4 Hrs	1 Hr	2 Hrs	3 Hrs	4 Hrs
NPC-393	50	35	27	22	53	42	38	37
NPC-583	36	27	22	18	53	44	41	37
NPC-628	30	23	18	16	44	38	35	32
NPC-673	26	20	16	12	40	32	27	26
NPC-713	23	18	15	12	37	31	28	25
NPC-753	22	18	15	10	31	25	20	15
NPC-833	25	19	16	14	36	29	24	22
NPC-913	33	30	26	22	54	50	46	43
NPC-1023	36	29	25	21	52	47	45	44
P25	50	35	27	24	35	29	22	15

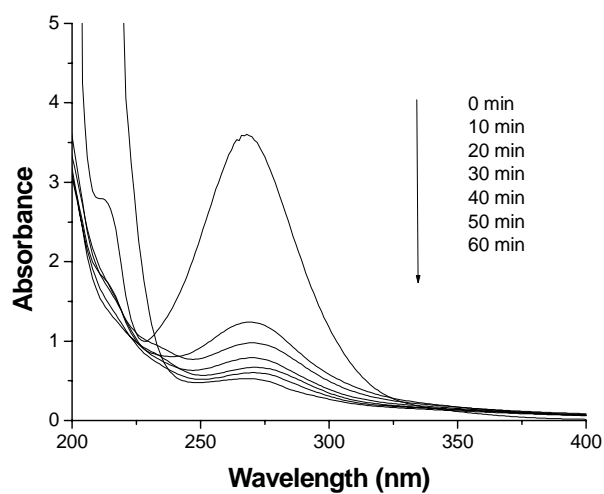
2.5.3. Photocatalytic Degradation studies by Catalysts Prepared by Method B

The photocatalytic activity of the catalysts prepared by Method B was also determined by degradation of AP and NB. The absorbance spectra for degradation of NB and AP with Ti-Ag catalyst is shown in Figure 2.24. From the graph it is understood that with time both AP and NB got degraded with Ti-Ag. Similar trend was obtained for other catalysts also. The graph of concentration verses time for degradation of AP and NB using all catalysts is given in Figure 2.25. The highest photocatalytic degradation was obtained for AP with Ti-Ag. The complete

degradation of AP took place in 4 hours while NB got degraded to around 90% in the same duration.



(a) Degradation of AP using Ti-Ag



(b) Degradation of NB using Ti-Ag

Figure 2.24: UV-Vis absorption spectra of degradation of (a) AP and (b) NB using Ti-Ag.

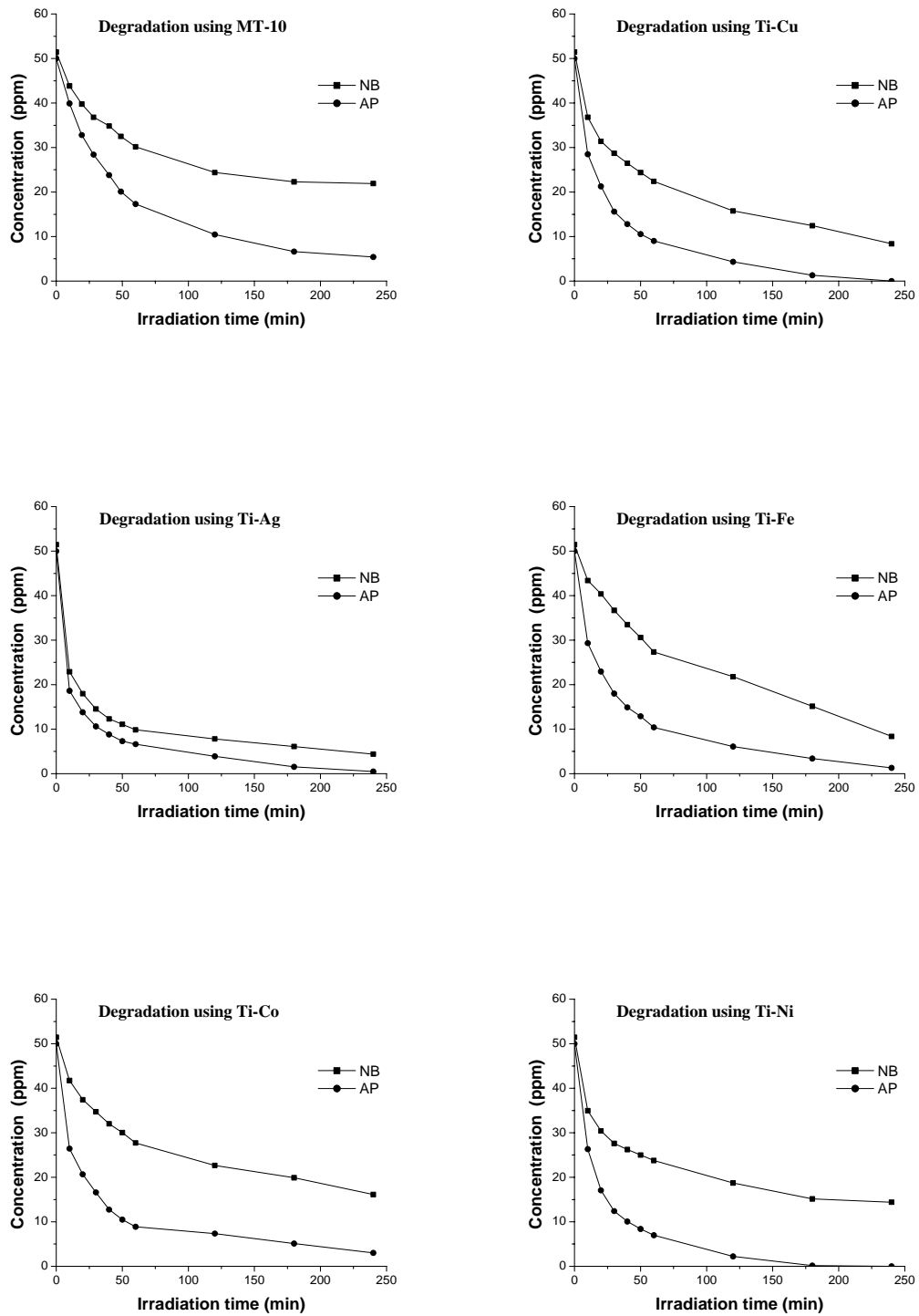


Figure 2.25: Degradation of AP and NB using metal ion impregnated semiconductor photocatalysts under UV light with respect to time

The COD values were also measured for organic solutions degraded for 1-4 hours with all metal impregnated catalysts which are as shown in Table 2.12. It is understood from this table that the organic compounds photocatalytically degraded with NPC-753 has the lowest measured COD in 4 hours duration. The lowest COD values were obtained for both organic compounds using Ti-Ag.

Table 2.12: Decrease in COD of reaction mixture of AP and NB using synthesized catalysts.

Catalyst	COD of reaction mixture of AP and NB with respect to irradiation time (mg/L)							
	Acetophenone (Initial COD= 120 mg/L)				Nitrobenzene (Initial COD= 90 mg/L)			
	1 Hr	2 Hrs	3 Hrs	4 Hrs	1 Hr	2 Hrs	3 Hrs	4 Hrs
MT-10	50	35	27	22	35	28	22	13
Ti-Ag	27	21	16	12	16	14	10	06
Ti-Fe	32	29	17	14	48	37	24	11
Ti-Co	32	22	16	14	49	39	27	26
Ti-Cu	35	26	20	16	37	25	19	11
Ti-Ni	28	18	13	12	41	31	24	23

2.6. Results and Discussions

The TiO₂ catalysts prepared by both Method A and Method B are nanocrystalline in nature. This is evidenced by the crystallite size calculated by the substitution of parameters obtained from XRD patterns (Figures 2.2, 2.3, 2.4) in equation 2.1 which are tabulated in Table 2.2, 2.4. The XRD patterns (Figure 2.2) of catalysts prepared by Method A showed that the amorphous TiO₂ converted to anatase phase with increase in calcination temperature. The XRD peaks became sharper as the calcination temperature was increased. The NPC-393 catalyst was amorphous in nature upto 393K. As the calcination temperature was increased, transition from amorphous to anatase phase started with complete anatase phase constitution at 833K. Further when the calcination temperature was increased, anatase phase started disappearing with increasing rutile phase which appeared at 913K. This suggests that there was a phase transition from anatase to rutile which agreed with previous results [54]. Residual anatase phase still existed in the catalysts upto 913K. At 1023K, the transition from anatase to rutile phase was complete.

As understood from Table 2.1, the smallest crystallite size was obtained at a calcination temperature of 393K. At higher calcination temperatures, the crystallite size of the catalyst increased. This can be attributed to the thermally promoted crystallite growth [54]. The size of anatase crystallites increased from 8 to 29 nm when the calcination temperature was raised from 393K to 913K. There were also some changes observed in lattice parameters with the increase in calcination temperature. This showed that an increase in calcination temperature is responsible for the changes in morphology, phase transitions (amorphous to anatase and anatase to rutile phase conversation) and also the electronic properties of semiconductor photocatalyst (band edge and bandgap) [54, 55, 60-62].

The calcination temperature also affected the surface area of the catalyst (Figure 2.26). The catalyst prepared at 393K had the highest surface area which decreased with the calcination temperature. Similar was the effect on pore volume of the catalysts. Apparently, the surface area can be correlated to the crystallite size, i.e. smaller size crystallites had larger specific surface areas. As the calcination temperature was raised to 1023K, the surface area reduced to 2 m²g⁻¹. The increase in

temperature causes the sintering in the catalyst and this reduces the surface area of the catalyst whereas crystallite size increased.

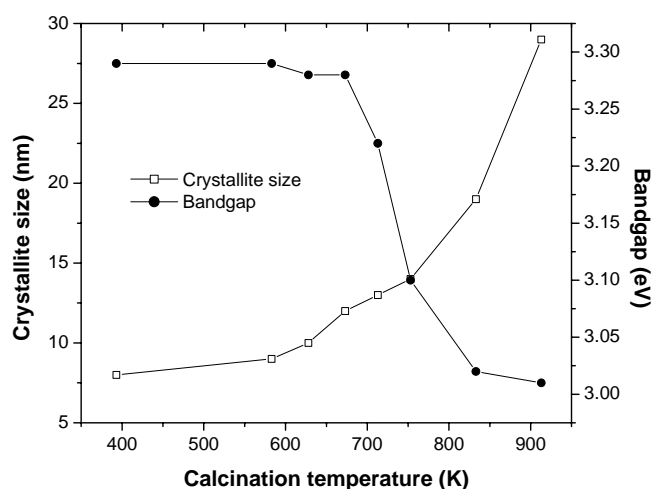


Figure 2.26: Effect of calcination temperatures on crystallite size and bandgap on the catalysts

It is well known that the bandgap of semiconductor material depends on crystallite size and as the crystallite size increases, bandgap decreases [54]. From Table 2.5, it is understood that an increase in the calcination temperature decreased the bandgap of the catalysts. The decrease in bandgap may be due to the increase in crystallite size of the catalyst. The bandgap of the catalysts decreased from 3.29 to 3.01 eV and crystallite size increased from 8-29 nm. The bandgap of standard P25 Degussa catalyst is 3.15 eV. The bandgap obtained for NPC-913 catalyst containing anatase and rutile phase was 3.01 eV. Figure 2.26 show the effect of calcination temperatures on crystallite size and bandgap of the catalysts.

From the experimental results, it is understood that thermal treatment in air leads to an enhancement in photocatalytic activity of catalysts for degradation of MB, MG, AP and NB until the anatase phase was predominately present till 753K calcination temperature with total absence of rutile phase. Further increase in temperature, increased the rutile phase content that led to decrease in photocatalytic activity. This is in agreement with well known concept that TiO_2 in rutile phase is less effective than that in the anatase form for the degradation of most organic compounds [63-65]. Therefore, it can be understood that the TiO_2 catalyst which was thermally treated at 833K had shown to exhibit lower photocatalytic activity than that thermally treated at 753K. It is thought that thermal treatment in air allows more oxygen molecules to be

adsorbed on the surface of TiO_2 . These oxygen molecules act as photoexcited electron traps and inhibit the recombination of photoexcited electrons and holes [66].

Thus it is established from the experimental results that thermal treatment induces alterations in phase constitution, crystallite size and surface area of the catalyst. It may be concluded that a temperature of 753K favours optimum physical characteristics of the catalyst where the photocatalytic activity of catalyst was at its peak. Further, it was understood that at this calcination temperature, the bandgap of the catalyst was the lowest (3.1 eV) among all the catalysts calcined at temperatures below 753K. Lowering in bandgap increases the absorption spectrum of the catalyst. This lowest bandgap favours increased light absorption capacity of the catalyst promoting greater number of electrons and holes at the surface of the catalyst. These greater number of electron-hole pairs participate in the oxidation and reduction process, thereby increasing its photocatalytic activity. The initial rate of degradation of MB, MG, AP, and NB using all catalyst prepared by Method A is given in Figure 2.27

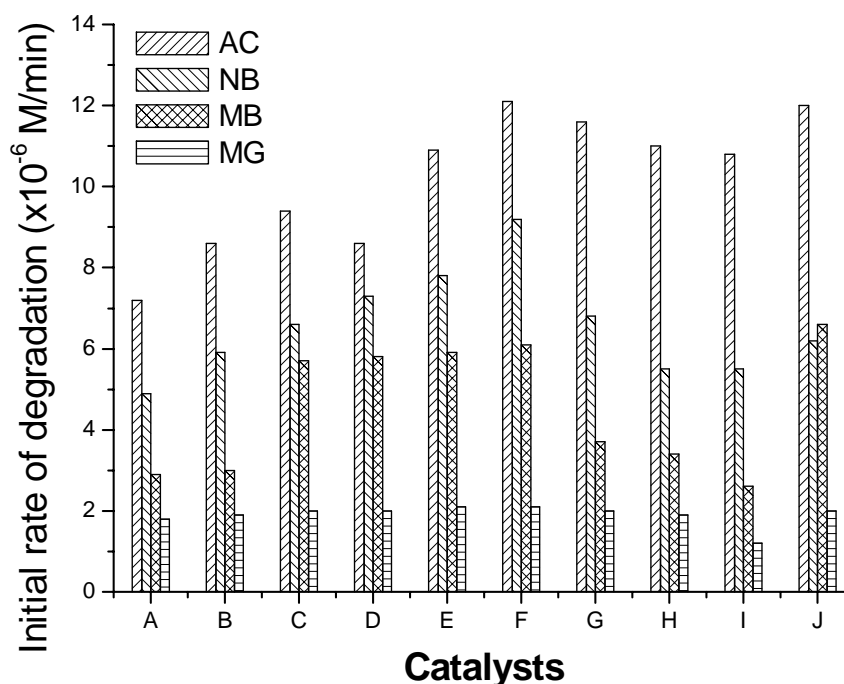


Figure 2.27 : Initial rates of degradation of dyes and organic compound using catalysts A) NPC-393 B) NPC-583 C) NPC-628 D) 673 E) NPC-713 F) NPC-753 G) NPC-833 H) NPC-913 I) NPC-1023 J) P-25 under UV light.

From the experimental results of metal impregnated catalysts, it is understood that metal dopants affect the characteristics and performance of catalysts. The XRD patterns (Figure 2.3) of metal impregnated (Ag, Co, Cu, Fe, Ni) catalysts and MT-10 showed no substantial change in the peak positions and peak area without any detectable dopant-related peaks. This confirmed that the metal impregnated catalysts had nearly the same phase constitution (Table 2.2) It is found that the crystallite size in the metal impregnated catalysts varied by 12 nm in order of Ag-doped (44) < Fe-doped (45) < Ni-doped (48) < Co-doped (49) < Cu-doped (50). The lowest crystallite size in Ag-doped enhanced the promotion of electrons and holes to the surface of the catalyst coupled with decrease in recombination rate within the catalyst [67]. This imparts increased photocatalytic activity to Ag doped catalysts as compared to other metal impregnated catalysts, Figures 2.18, 2.19, 2.24, and 2.25. The initial rates of degradation of MB, MG, AP, and NB are given in Figure 2.28 using catalysts synthesized by Method B.

The highest surface area was obtained for Ag-doped catalyst ($32 \text{ m}^2\text{g}^{-1}$) amongst other metal (Co, Cu, Fe, Ni) impregnated catalysts. The Ti-Ag catalyst with highest surface area facilitates the availability of increased electron-hole pairs at the surface of the catalyst that participates in the oxidation and reduction processes [68]. Therefore, the highest photocatalytic activity was obtained with Ag-doped catalyst Figure 2.19 and 2.25.

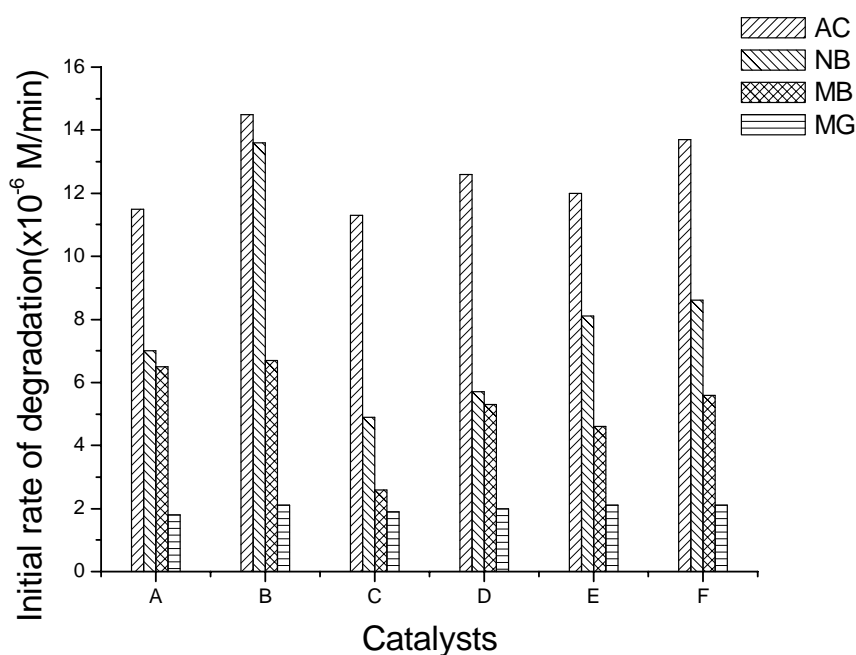


Figure 2.28 : Initial rates of degradation of AP and NB using catalyst (A) MT-10 (B) Ti-Ag (C) Ti-Co (D) Ti-Cu (E) Ti-Fe (F) Ti-Ni under UV light.

For metal ions in interstitial and substitutional positions, the change in their potential level is different and they have different trapping efficiencies for electrons. The effect of the interstitials in distorting the potential energy is larger than that of substitutional atoms. According to XRD results of doped TiO₂, no separate dopant related phase was observed. This finding indicates that dopant ions Ag, Co, Cu, Fe, Ni are either in octahedral interstitial sites or the substitutional positions of TiO₂. From the effective radii of ions in Table 2.2, it is understood that Co, Cu, Fe, Ni have ionic radii comparable to that of Ti. It is energetically favourable for these metal ions to occupy Ti sites. Ag on the other hand has an ionic radius that is much larger than that of Ti. It is energetically favourable to Ag ion to reside in the octahedral interstitial site. The size of octahedral interstitial is large enough, 3.78 and 9.51 for a and c axes respectively, to accommodate Ag. The substitutionally incorporated dopants are less useful for disturbing the energy level, which in turn affects the electron trapping efficiency. Co, Cu, Ni showed reduced photocatalytic enhancements compared with Ag, whereas Fe doping showed complete lack of enhancement in the photocatalytic activity. Thus, these may presumably be in substitutional positions with very little or

no potential energy disturbance, thereby diminishing their electron trapping efficiency and hence the photocatalytic activity.

Another contributing reason for the lack of photocatalytic activity enhancement by Fe may include nonoptimal valency of Fe. The accurate determination of Fe oxidation state when it is present in such low concentrations is difficult because of the problem in satisfactorily resolving the Fe 3p region of XPS spectrum [74].

For the interstitial dopants like Ag, the potential energy level can be increased negatively towards the conduction band edge because of the oxygen affinity of dopant ions. The high oxygen affinities of interstitially located Ag ions effectively create a localized positive charge around Ti and /or form an oxygen vacancy. The potential energy of ion dopants was disturbed and electrons were efficiently trapped. Consequently, the oxidation and reduction processes of MB, MG, AP, NB were improved. Another reason for enhancements in photocatalytic activity in catalysts impregnated with Ag and Cu is the charge trapping [73].

The COD results, Tables 2.9, 2.10, 2.11 and 2.12 showed that the percentage degradation of dyes and organic compounds depend upon the photocatalytic activity of the catalysts. The complete degradation of dyes was faster as compared to organic compounds. The degradation of dyes completed within 2-3 hours. The catalyst NPC-753 showed best degradation of 92% in 2 hours for MB and 95% for MG and both degraded completely within 3 hours. Similarly, the catalyst NPC-753 showed best degradation of 92% in 2 hours for AP and 83% for NB. The rutile catalyst NPC-1023 had shown the minimum decrease in COD for both dyes and organic compounds.

Also, it is understood from Table 2.11, 2.12 that the photocatalytic degradation of dyes and organic compound using catalysts prepared by Method B, i.e., metal ion impregnation depended on the type of metal ion impregnated. Ag ion impregnated catalyst demonstrated best photocatalytic activity for MB and MG amongst Co, Cu, Fe and Ni impregnated catalysts. Both dyes degraded to 90% in 1 hour and then were completely degraded within 2 hours. Ag impregnated catalyst degraded both AP and NB to 90% and 93% in 4 hours respectively while the degradation of same with other catalysts ranged from 75-90%.

From above results, it revealed that Ag ion impregnated catalyst exhibited the highest photocatalytic activity for both dyes (MB, MG) and organic compounds (AP, NB).

Also, the degradation rate exhibited by Ag ion impregnated catalyst was excellent as compared to other catalysts.

It is concluded from this study that the photocatalysts synthesized by both Method A and B, which had higher surface area, minimum bandgap and small crystallite size with maximum anatase phase constitution demonstrated the highest photocatalytic activity for degradation of dyes and organic compounds. The bandgap of the TiO₂ was found to depend upon the crystallite size. Thermal treatment and metal ion doping changed the bandgap of the catalysts. The complete decolorisation and degradation of dyes was obtained under irradiation of UV light. The metal ion played major role in the enhancement of photocatalytic activity. The catalyst having minimum bandgap and minimum work function prepared with metal ion impregnation method exhibited the highest photocatalytic activity for the degradation of dyes and organic compounds as compared to other catalysts. The silver metal ion impregnated photocatalyst was found to be a better catalyst as compared to other metal impregnated catalysts.

2.7. References

- [1] R. W. Siegel, *Ann. Rev. Mater. Sci.* 21, (1991). 559.
- [2] R. P. Andres, T. Bein, M. Dorogi, S. Feng, J. I. Henderson, C. P. Kubiak, W. Mahoney, R. G. Osifchin, R. Reifengerger, *Science* 272, (1996)1323.
- [3] A. Eychnuller, *J. Phys. Chem. B* 104 (2000) 6514.
- [4] J. Y. Chen, L. Gao, J. H. Huang, *J. Mater. Sci.* 31, (1996)3497.
- [5] D. C. Hague, M. J. Mayo, *J. Am. Ceram. Soc.* 77, (1994)1957.
- [6] K. -N. P. Kumar, K. Keizar, A. J. Burggaraaf, T. Okubo, H. Nagamoto, S. Morooka, *Nature* 358 (1992) 48.
- [7] A. Fujishima K. Honda, *Nature* 238 (1972) 37.
- [8] A. Larson J. L. Falconer, *Applied Catalysis B: Environmental* 4 (1994) 325.
- [9] P. V. Kamat, N. M. Dimitrijevic, *Solar Energy* 44(2) (1990) 83.
- [10] L. Micheli, *Am. Ceram. Soc. Bull.* 54 (1984) 694.
- [11] K. L. Sieferting and G. L. Gri\$n, *J. Electrochem. Soc.* 137(3) (1990) 814.
- [12] H. Tang, K. Prasad, R. Sanjjiness, F. Levy, *Sens. Actuators B* 26-27 (1995) 71.
- [13] H. Kominami, H. Kumamoto, Y. Kera, B. Ohtni, *Applied Cataysis B: Environmental* 20 (2001) 329
- [14] H. Zhang, J. F. Banfield, *J. Phys. Chem. B* 104 (200) 3481.
- [15] X. M. Wu, L. Wang, Z. C. Tan, G. H. Li, S. S, Qu, *J. Solid State Chem.* 156 (2001) 220.
- [16] S. Sakka, *Am. Ceram. Soc. Bull.* 64 (1985) 1463.
- [17] I. Moriguchi, H. Maeda, Y. Teraoka, s. Kagawa, *Chem. Mater.* 9 (1997) 1050.
- [18] C. Sanchez, F. Ribot, *New J. Chem.*, **18**, (1994) 1007.
- [19] J. Livage, M. Henry, C. Sanchez, *Progress in Solid State Chemistry*, **18**, 259, (1988)].
- [20] C. H. Kwon, J. H. Kim, I. S. Jung, H. Shin, K. H. Yoon, *Ceramics International* 29 (2003) 851
- [21] H. Jiang, L. Gao, *Mater. Chem. Phys.* 77 (2002) 878.
- [22] M. I. Litter, *Applied Catalysis B: Environmental* 23 (1999) 89.
- [23] M. I. Litter, J. A. Navio, *J. Photochem.Photobio. A: Chemistry* 98 (1996) 171
- [24] M. D. Fuerte, H. Alonso, A. J. Maira, A. Martínez-Arias, M. Fernández-García, J. C. Conesa , J. Soria, *Chem. Commun.* 24 (2001) 2718.
- [25] M. Anpo, Y. Ichihashi, M. Takeeuchi, H. Yamashita, *Science and Technology in Catalysis*, 1998, 305.
- [26] Y. Fu, C. Shearwood, *Scripta Materialia*, 50 (2004) 319.
- [27] Y. Wang, H. Cheng, Y. Hao, J. Ma, W. Li, S. Cai, *J. Mater. Sci.* 34 (1999) 3721.

- [28] M. S. Jeon, W. S. Yoon, H.K. Joo, T. K. Lee, H. Lee, *Appl. Surf. Sci.* 165 (2000) 209.
- [29] E. Traversa, M. L. D. Vona, P. Nunziante, S. Licoccia, T. Sasaki, N. Koshizaki, *J. Sol-Gel Sci. Technol.* 19 (2000) 733.
- [30] W. L. Burns, C. Backer, S.I. Shah, *Mat. Res. Soc. Symp. Proc.* Vol. 703.
- [31] J. Z. Zhang, *J. Phys. Chem. B* 104 (2000) 7239.
- [32] S. X. Liu, Z. P. Qu, X. W. Han, C. L. Sun, *Catalysis Today* 93-95 (2004) 877.
- [33] M. D. Ward, A. J. Bard, *J. Phys. Chem.* 1982, 86, 3599-3605.
- [34] H. Tada, K. Teranishi, Y. Inubushi, S. Ito, *Chem. Commun.* (1998) 2345.
- [35] S. I. Shah, W. Li, C. -P. Huang, O. Jung, C. Ni, *PNAS* 99 (2002)6482.
- [36] H. Uchida, S. Katoh, M. Wanatanabe, *Electrochimica Acta* 43 (1998) 2111.
- [37] M. Valden, X. Lai, and D. W. Goodman, *Science*, 281 (1998) 1647.
- [38] P. L. Hansen, J. B. Wagner, S. Helveg, J. R. Rostrup-Nielsen, B. S. Clausen, H. Topsøe, *Science*, 295, (2002) 2053.
- [39] C. T. Campbell, *Surf. Sci. Rep.*, 27, (1997) 1.
- [40] C. Verdozzi, D. R. Jennison, P. A. Schultz, M. P. Sears, *Phys. Rev. Lett.*, 82, (1999) 799.
- [41] D. J. Siegel, L. G. Hector, J. B. Adams, *Phys. Rev. B*, 65, (2002) 85415.
- [42] C. C. Wong, W. Chu, *Chemosphere* 50 (2003) 981.
- [43] S. Sakhthivel, B. Neopolian, M.V. Shanker, B. Arabindoo, M. Palanichamy, V. Murugesan, *Solar Energy Materials & Solar Cells* 77 (2003) 65-82.
- [44] C. H. Ao, S. C. Lee, C. L. Mak, L. Y. Chan, *Applied Catalysis B: Environmental* 42 (2003) 119.
- [45] E. Bessa, G. L. Santaanna Jr., M. Dezotti, *Applied Catalysis B: Environmental* 29 (2001) 125.
- [46] M. Gratzel *Heterogeneous Photochemical Electron Transfer*. CRC Press, Boca Raton, FL.
- [47] W. Wang, M. Gu, Y. Jin, *Materials Letters*, 57 (2003) 3276.
- [48] J. Arana, J. M. Dona-Rodriguez, O. Gonzalez-Diaz, E. Tello Rendon, J. A. Herrera Melian, G. Colon, J. A. Navio, J. Perez Pena, *Journal of Molecular Catalysis A: Chemical* 215 (2004) 153.
- [49] JCPDS-ICDD, Copyright (c) 1996, Reference Pattern Database
- [50] R. A. Spurr, H. Myers, *Anal. Chem.*, 29 (1957) 760.
- [51] L. V. Nadtochenko, J. Kiwi, *Langmuir* 16, 2000, 1102.
- [52] Y. H. Hsien, C. F. Chang, Y. H. Chen, S. Chen, *Applied Catalysis B: Environmental* 31 (2001) 241.
- [53] J. Liqiang, S. Xiaojun, C. Weimin, X. Zili, D. Yooguo, F. Honggang, *Journal of Physics and Chemistry of Solids* 64 (2003) 615.

- [54] Y. -F. Chen, C. -Y. Lee, M. -Y. Yang, H. -T. Chiu, *Journal of crystal growth* 247(2003) 363.
- [55] R. R. Basca, J. Kiwi, *Applied Catalysis B: Environmental* 16 (1998) 10.
- [56] J. C. Yu, J. Lin, D. Lo, S. K. Lam, *Langmuir* 16, 2000, 7304.
- [57] E. Traversa, M. L. D. Vona, P. Nunziante, S. Licocchia, T. Sasaki, N. Koshizaki, *J. Sol-Gel Sci. Technol.* 19 (2000) 733.
- [58] S. J. Gregg, K. S. W. Sing, *Adsorption, Surface Area and Porosity*, 2nd Ed; Academic Press: New York, 1982.
- [59] U. S. EPA February 1995, Nitrobenzene Fact sheet: Support document
- [60] E. J. Kim, S. -H. Hahn, *Materials Letters* 49(2001) 244.
- [61] Z. Baolong, C. Baishun, S. Keyu, H. Shangin, L. Xiaodong, D. Zongjie, Yang Kelian, *Applied Catalysis B. Environmental* 40 (2003) 253.
- [62] C. M. Wang, A. Heller, H. Gerischer, *J. Am. Chem. Soc.* 114, (1992) 5230.
- [63] M. A. Fox, M. T. Dulay, *Chem. Rev.* 93 (1993) 341.
- [64] A. Sclafani, J. M. Herrmann, *J. Phys. Chem.* 100 (1996) 13655.
- [65] J. C. Yu, J. Lin, *J. Photochem. Photobio. A: Chemistry* 111 (1997) 199.
- [66] J. C. Yu, Jun Lin, D. Lo, S. K. Lam, *Langmuir* 16 (2000) 7304.
- [67] H. Tada, T. Suzuki, S. Yoneda, S. Ito, H. Kobayashi, *Phys. Chem Chem. Phys.* 3 (2001) 1376.
- [68] H. Tada, K. Teranishi, Y.-I. Inibushi, S. Ito, *Chem. Commun.* (1998) 2345.
- [69] N. -G. Park, J. van de Lagemaat, A. J. Frank *J. Phys. Chem. B*, 104 (2000) 8989.
- [70] D. Ward, A. J. Bard, *J. Phys. Chem.* 69 (1982) 3599.
- [71] A. Burns, W. Li, C. Baker, S. I. Shah, *Mat. Res. Soc. Proc.* (2002) 703
- [72] M. S. Vohra, K. Tanaka, *Water Research* 36 (2002) 59.
- [73] K. V. Subba Rao, B. Lavedrine, P. Boule, *Journal of Photochem. Photobio. A: Chemistry* 154 (2003) 189.
- [74] S. I. Shah, W. Li, C.-P. Huang, O. Juang, C. Ni, *PNAS*, 99 (2002) 6482.

CHAPTER - 3

ENCAPSULATION OF PHOTOCATALYSTS

IN POROUS SOLIDS

3.1. Introduction

Semiconductor TiO_2 is one of the most effective photocatalyst because it is biologically and chemically inert and photostable with near ultraviolet bandgap energy. The bandgap depends upon the particle size of photocatalysts. The minimum bandgap of the photocatalyst favours higher photodegradation. The photocatalytic activity of the photocatalyst depends upon the electron-hole pair recombination. The recombination rate of the electron-hole pair is higher in bulk or large size semiconductor photocatalyst particles. The photocatalytic degradation takes place at the surface of photocatalyst. The photocatalytic activity of the photocatalyst decreases due to the electron-hole pair recombination before reaching to the surface of the photocatalyst. The nanosize particles exhibit quantum size confinement effects which is responsible for enhancement in the photocatalytic activity of photocatalysts. The fine TiO_2 powder or crystals can be dispersed in waste water to be clarified by irradiation, but they should be removed by filtering after reaction, which is tedious and costly. Thus, in order to solve this problem, many researchers have examined methods for fixing TiO_2 on other support materials like glass beads [1, 2], fibre-glass [3, 4], silica [5], electrode [6], clays [7] and zeolites [8-11]. But zeolites are interesting hosts to fix semiconductors because it has unique uniform pores and channel size [12-19].

Zeolites are found useful in photochemistry since they can adsorb and provide reaction surface to various molecules including organics in their cavities and channels and such inclusions have often been shown to modify the normal solution photochemistry of a given species. The confinement of molecules within the constrained space and the catalytic activity of the surface adsorption sites were considered decisive for host selection unique to zeolites. Zeolite are also well characterized in literature, zeolite science covers a broad spectrum, from synthesis to structural characterisation, adsorption and transport phenomena, and applications such as catalysts and other classical uses (adsorbents or desiccants, water softeners, soil improvers, and so forth) [20-22]. Furthermore, zeolites have been recognized as new materials for optical and electronic applications, such as lasers, quantum dots and Second Harmonic Generator (SHG) in recent years [23-26].

It is possible to accommodate a photoactive guest within the internal voids of pores created by the rigid zeolite framework. The presence of heteroatoms like Ti, V and other transition metals in the zeolite framework can make the structure as a whole to act as a photocatalyst [19, 27-29]. Figure 3.1 show the application of zeolite to design photocatalyst for the degradation of pollutants.

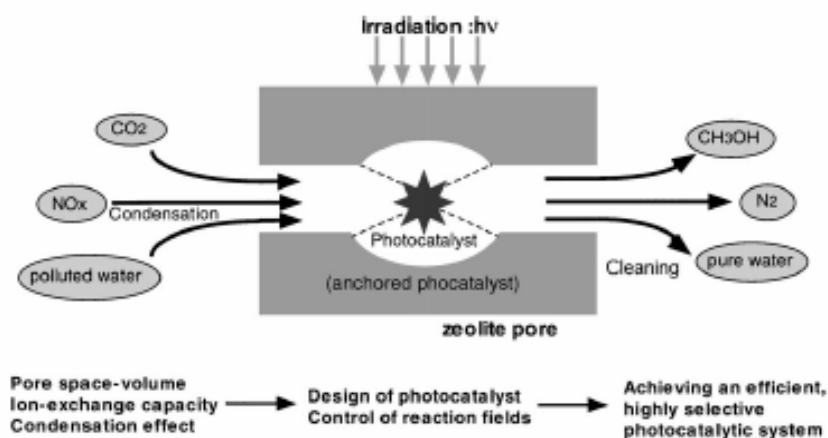


Figure 3.1: Application of zeolite to design photocatalyst for the degradation of pollutant.

Zeolites, similar to glasses and quartz vessels, are made up of silica and alumina and therefore generally one should be able to excite an organic molecule without perturbing the electronic structure of the zeolite. The combination of a zeolite host and photoactive sites renders a solid photocatalyst in which the high surface area and the adsorbent capacity provided by zeolites co-operate to increase the efficiency of the photocatalytic process. In addition, the zeolite pores define a compartmentalized space in which multi-component systems can be easily assembled by stepwise procedure. Other positive effects derived from the encapsulation of a guest inside zeolites are the observation of quantum size effects for semiconductor clusters and a favourable polar environment for photoinduced electron transfer. In semiconductor photocatalysis, light absorption excites electron from valence to the conduction band. The mobility of the excited electron in the conduction band may lead to charge separation with the creation of positive vacancies in the valence band and mobile electrons in the conduction band. This charge separation combined with interfacial electron transfer processes from the surface of the semiconductor particle to the substrate is the base of photocatalytic processes. The efficiency of the photocatalyst is

a function of the balance between charge separation, ease of interfacial electron transfer and energy-wasting charge recombination.

Among the advantages of zeolites as hosts, the one that makes these solids very attractive as hosts is their large surface area and internal pore volume. Surface areas in the range of 400–650 m²g⁻¹ with pore volumes of above 0.1 cm³g⁻¹ are not uncommon for conventional zeolites. In fact, zeolites are among the most porous materials known, being suitable to adsorb guests. These values are among the largest pore dimensions that are available for conventional zeolites. The empty voids of the dehydrated zeolites provide a compartmentalised space in which photosensitisers can be located or where multi-component systems can be assembled in a spatially organised manner and held in place without the need of covalent bonds. Zeolites and related molecular sieves exhibit several specific features that make them suitable for their use as hosts for photosensitisers such as: (i) full photochemical stability and large thermal and chemical inertness (ii) transparency to UV-Visible radiations above 240 nm thus allowing a certain penetration of the exciting light into the solid opaque powder to reach the guests located in intraparticle positions (iii) the possibility to vary the chemical composition of framework and out-of-framework positions in a large extent, thus rendering these molecular sieves photoactive or introducing active sites to co-operate in the photocatalytic activity (iv) zeolite's high adsorptivity for organic compounds in solution adding to the concentration of the substrates in the proximity of the photosensitiser contributing to the success of the photocatalytic process (v) modulation of the micropolarity and the polarizing strength of the zeolite interior by varying the nature of internal charge balancing cations (charge density) and the size of the channels. The latter factor can lead to dramatic changes and modifications in the electronic states and conformational mobility of the guests within zeolites (vi) ability of the zeolite framework to participate actively in electron transfer processes, either as electron acceptor or electron donor. Thus upon photoexcitation, an incorporated guest can eject an electron that will become delocalised through the framework or in clusters of the charge balancing cations. Also, there are reverse processes in which electron-rich sites of the zeolite can donate an electron to photoexcited guests [30].

Zeolite based photocatalysts are promising for the abatement of air and water pollution using solar light, as well as for de-NO_x and de-SO_x processes, photoreduction of CO₂ by H₂O, photooxygenation of saturated hydrocarbons, photosplitting of water into hydrogen and oxygen, photogeneration of hydrogen

peroxide and other photoprocesses of much current interest, particularly in environmental sciences and for the development of renewable energy resources alternative to fossil fuels [31-36].

A combination of well-defined highly dispersed catalysts and multifunctional materials like zeolite will make it possible to develop novel photocatalytic systems that can completely decompose toxic organic compounds into completely oxidized non-toxic compounds such as CO₂, H₂O and HCl, as shown in Figure 3.2.

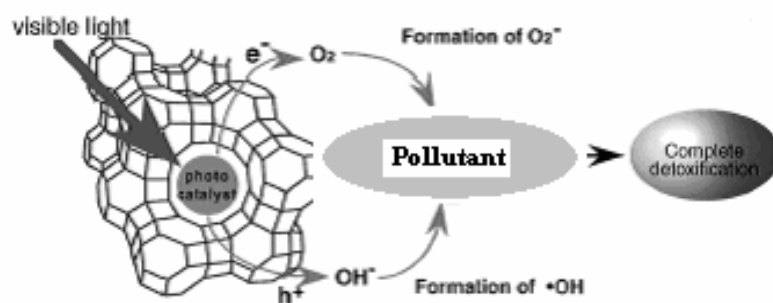
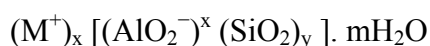


Figure 3.2: Photocatalytic system using zeolite as a host for photocatalyst for the degradation of pollutants.

3.2. Zeolites

3.2.1. Structure and chemical properties of zeolites

Zeolites are microporous crystalline aluminosilicate materials with alkali or alkaline earth metals as counter ions [21-22]. As pictorially represented in Figure 3.3, they consist of a framework of [SiO₄]⁴⁻ and [AlO₄]⁵⁻ tetrahedra linked to each other at the corners by sharing their oxygens. This leads to the following general formula:



In this formula, M⁺ represents the alkali metal cation. The tetrahedra make up three-dimensional network structures to form channels and cages or cavities of discrete size. In aluminium-containing zeolites, negative charges generated in the framework originating from the difference in charge between the [SiO₄]⁴⁻ and [AlO₄]⁵⁻ tetrahedral must be balanced by the charge compensating cations. These cations can

generally be exchanged by conventional methods of ion exchange. The cations and water molecules present are located in the cages (cavities) and channels. Several types of zeolites are frequently employed in photochemical research: their common names are X, Y, A, mordenite, L, ZSM-5, silicalite, MCM-41 or name a few. In the crystallographical classification [37], X and Y belong to FAU (Faujasite).

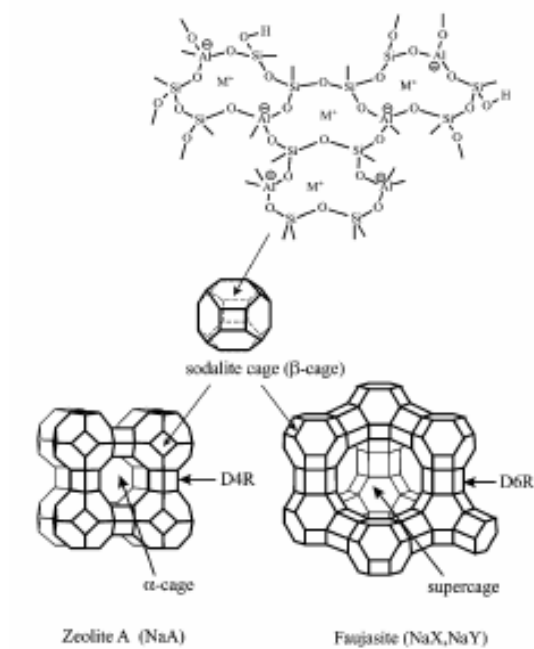


Figure 3.3: Framework structure of sodalite-based zeolite.

Physicochemical properties of some of the zeolites are tabulated in table 3.1.

Table 3.1: Properties and chemical composition of the zeolites.

Zeolite	Channel size in Å	Channel/ cavity diameter in Å	BET Surface Area in m ² g ⁻¹	Chemical Composition on anhydrous basis wt%		
				Na ₂ O	Al ₂ O ₃	SiO ₂
NaA	4.1 × 4.1	11.4	-	27.3	21.1	51.5
NaX	7.4 × 7.4	12.0	542	24.6	19.0	56.4
NaY 5.5	7.4 × 7.4	12.0	810	3.0	22.0	71.0
Zeolite L ^a	7.1 × 7.1	7.1	312	0.1	18.3	64.2
Na-Beta	6.6 × 6.7; 5.6 × 5.6	6.7	612	1.2	7.8	91.0
Na Mordenite 060	6.5 × 7.0; 2.6 × 5.7	7.0	50	7.5	12.4	80.1
Na Mordenite 510	6.5 × 7.0; 2.6 × 5.7	7.0	450	0.04	7.8	92.1
Na ZSM-5 (25)	5.1 × 5.5; 5.3 × 5.6	5.6	371	3.0	6.4	90.8
Na ZSM-5 (40)	5.1 × 5.5; 5.3 × 5.6	5.6	379	1.5	3.8	94.7
Na ZSM-5 (100)	5.1 × 5.5; 5.3 × 5.6	5.6	348	1.8	1.8	90.1
Na ZSM-5 (400)	5.1 × 5.5; 5.3 × 5.6	5.6	334	1.5	0.4	98.0
Na ZSM-5 (900)	5.1 × 5.5; 5.3 × 5.6	5.6	315	1.5	0.2	98.1

^a:K₂O = 17.5%

3.3. Encapsulated Photocatalyst in Zeolites

The remarkable structural features and physicochemical properties of zeolites are expected to provide new aspects of photophysical and photochemical processes. The present study includes the preparation and characterisation of encapsulated photocatalyst in Na and H form of zeolite Y, henceforth referred as NaY and HY respectively. The varied amounts of TiO₂ were 1%, 2%, 4%, and 10% w/w in zeolite. Such lower amounts of TiO₂ were chosen to have fine dispersion of TiO₂ inside the

zeolite cavity. The synthesized catalysts were characterized for its physical properties using XRD, SEM, UV-Vis DRS and BET analysis. The effect of various amounts of encapsulated TiO₂ in zeolite was studied by the degradation of dyes like MB and MG and organic compounds like AP and NB.

3.3.1. Chemicals and Materials

Zeolite NaY with Si/Al ratio 5.5 from *United Catalysis India Ltd., Vadodara*, titanium tetra isopropoxide (97%) from *Sigma Aldrich India, Mumbai*, methylene blue, malachite green, nitrobenzene (99.0%) from *s.d. Fine Chemicals Ltd., Mumbai* and acetophenone and COD standard chemical reagents from *E. Merck India Ltd., Mumbai* were used for the photocatalyst preparation and photocatalytic studies.

3.3.2. Preparation of H- zeolite

Sodium form of zeolite was converted to hydrogen form by ammonium ion exchange method. The zeolite was heated with 1M ammonium nitrate solution at 353K for 4 hours, zeolite to ammonium nitrate solution ratio was 1:80. The residue was filtered and washed with hot distilled water. The above cycle was repeated three times to get complete exchange of sodium. The sample was dried at a temperature 353K for 8 hours and then calcined at 823K for 6 hours.

3.3.3. Activation of zeolite

The presence of water in zeolite significantly affects the encapsulation of TiO₂. The presence of water in the zeolite cavities forms precipitate on addition of titanium isopropoxide outside the zeolite cavity. Therefore, prior to loading of TiO₂, activation of the zeolite was carried out. The NaY and HY zeolites were calcined at 723K for 4 hours in a tubular furnace and then were cooled to room temperature under the flow of nitrogen.

3.3.4. Preparation of catalysts

The scheme for preparation TiO_2 encapsulated catalysts is given in Figure 3.4. The solution of dry ethanol (100ml) and an equivalent amount of titanium tetra isopropoxide was taken in a 250 ml round bottom flask to achieve loading of 1, 2, 4, 10% TiO_2 in both NaY and HY zeolites. This mixture was continuously stirred for 30 minutes and then ultrasonicated for 30 minutes. The activated zeolites (Section 3.3) were added to the above solution and stirred for 2 hours for penetration of solution inside the cavities of zeolites. The solvent was slowly removed from the mixture by using rotavapour (Buchi Rotavapour R-205) at 343K. The powder sample was then dried in an oven at 393K for 12 hours. The hydrolysis of TiO_2 was done by adding 25ml water to the powder sample and the solution was dried in an oven at 393K for 12 hours. This sample was further calcined under air at 723K for 11 hours. The catalysts thus obtained were designated as NYT1, NYT2, NYT4 and NYT10 for 1%, 2%, 4% and 10% encapsulation of TiO_2 respectively on NaY zeolite, in NaY zeolite and HYT1, HYT2, HY4, and HYT10 for 1%, 2%, 4% and 10% loading of TiO_2 respectively, in HY zeolite.

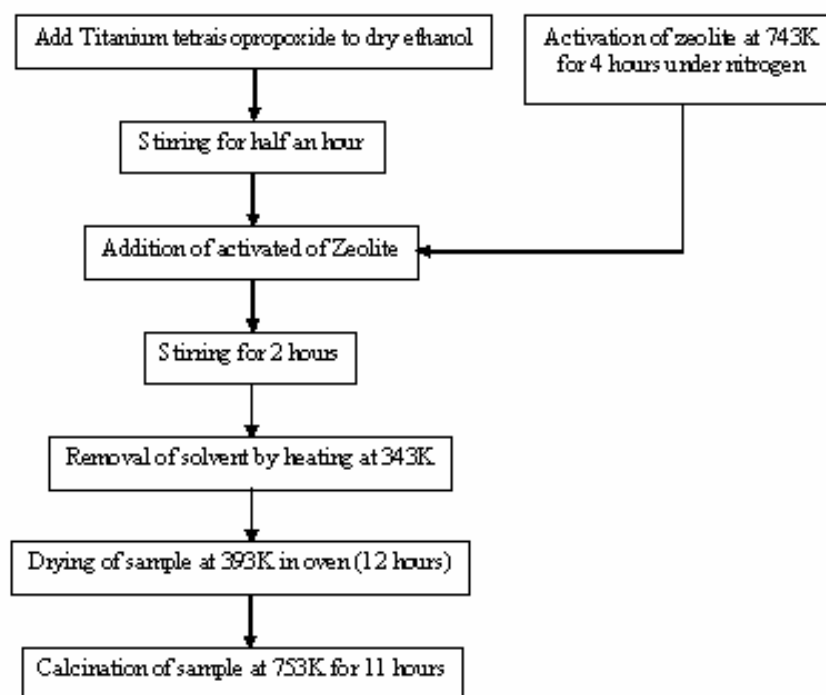


Figure 3.4: Schematic diagram of TiO_2 encapsulated zeolite preparation.

3.4. Characterisations of Encapsulated Photocatalysts

All the synthesized photocatalysts were characterised for their physical characterisation & photocatalytic activity as discussed in following section.

3.4.1. X-ray Powder Diffraction

X-ray powder diffraction studies were carried out at ambient temperature by *Philips X'pert MPD System* in the 2θ range 5-60 degrees using $\text{CuK}\alpha 1$ ($\lambda = 1.54056\text{\AA}$). The diffraction patterns of the NaY and HY zeolite showed that it is highly crystalline in the range 5-60 degrees typical to zeolites. The catalysts exhibited same crystallinity as that of NaY and HY zeolites and the structure of zeolite was retained. There was no peak obtained after encapsulation of TiO_2 which indicated that the encapsulation of TiO_2 took place in the cavity of both NaY and HY zeolites. After sodium ion exchange, some of the small peaks were vanished completely and the peak intensity of all peaks was reduced slightly. XRD pattern is shown in Figure 3.5. In HY zeolite the peak intensity of all peaks was reduced with increase in amount of TiO_2 , which is shown in Figure 3.6.

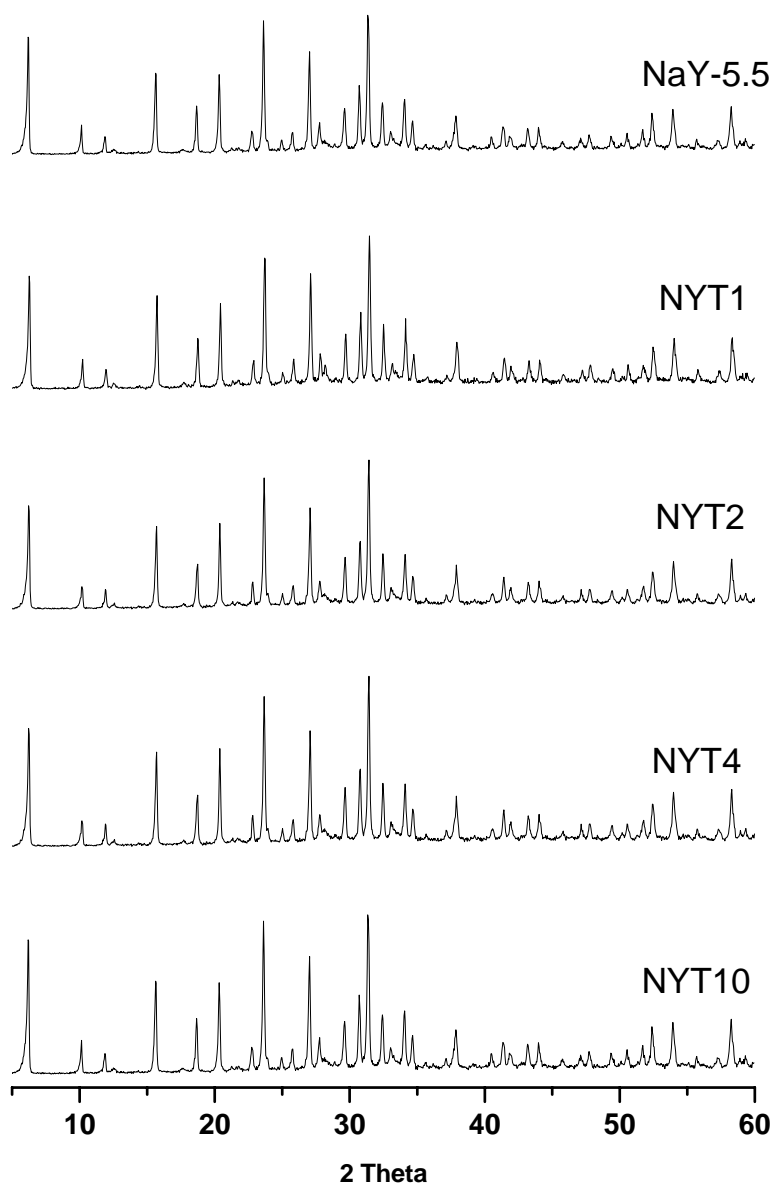


Figure 3.5: X-ray diffraction pattern of NaY zeolite and various amount of TiO₂ encapsulated NaY zeolite.

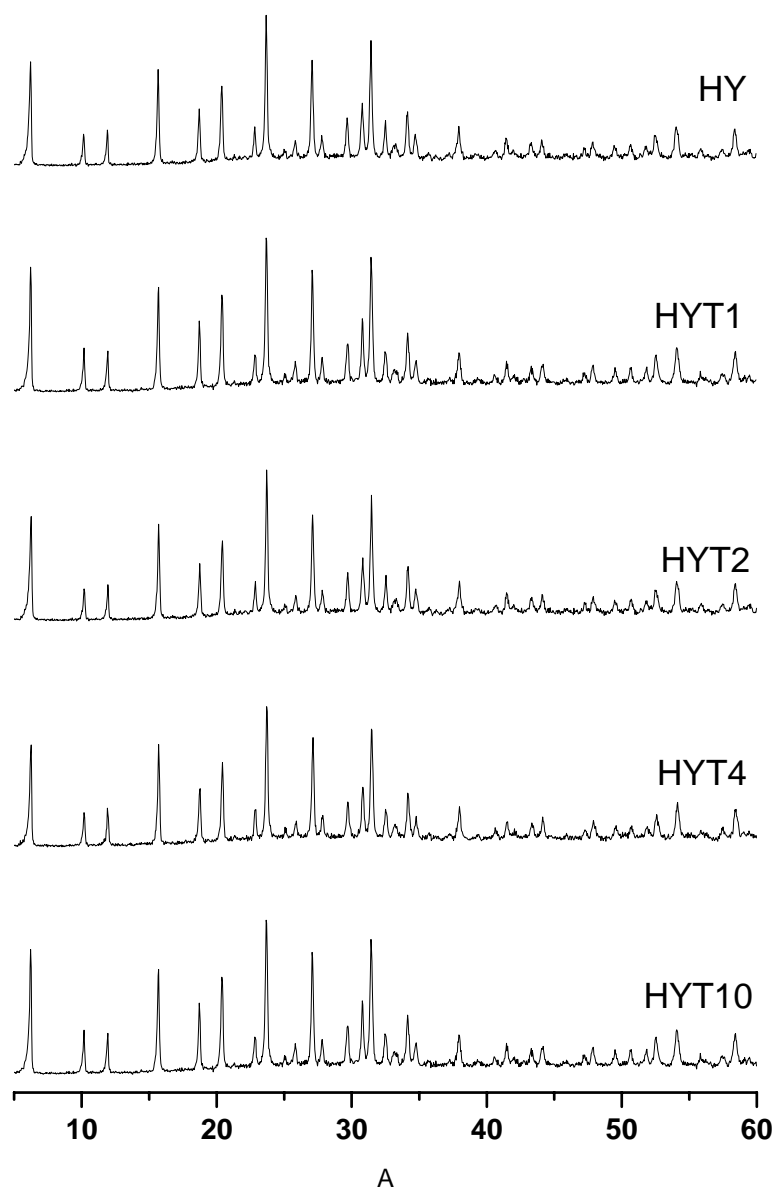


Figure 3.6: X-ray diffraction pattern of HY zeolite and various amount of TiO₂ encapsulated HY zeolite.

3.4.2. Surface area analysis (N₂ adsorption)

Specific surface area, pore volume, and pore size distributions of calcined of encapsulated photocatalyst samples were determined from N₂ adsorption-desorption isotherms at 77K by ASAP 2010, Micromeritics, USA. Surface area and pore size distribution were determined using the BET equation and BJH method respectively [38]. Figure 3.7 shows an adsorption & desorption isotherm of N₂ of zeolite NaY used

in this study at 77K. The BET surface area of the NaY zeolite found to be $698 \text{ m}^2\text{g}^{-1}$. The BET surface area of the NaY zeolite was slightly reduced after encapsulation of TiO_2 . After sodium ion exchange with H^+ ions it was increased to $754 \text{ m}^2\text{g}^{-1}$. The BET surface area of the TiO_2 encapsulated catalysts in NaY and HY zeolites catalysts are given in Table 3.2.

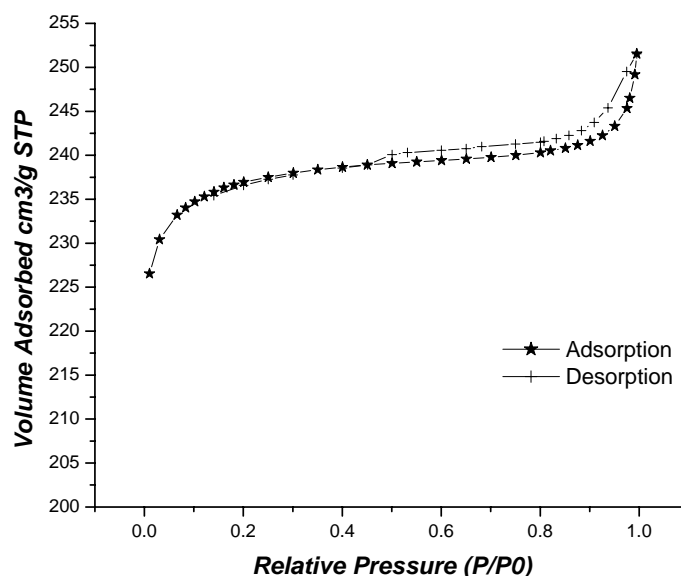


Figure 3.7: Adsorption and desorption isotherm curves of N_2 in zeolite NaY at 77 K: (*) adsorption (+) desorption.

Table 3.2: BET surface area of the encapsulated catalysts.

Catalyst	NYT1	NYT2	NYT4	NYT10	HYT1	HYT2	HYT4	HYT10
Surface Area (m^2/g)	678	659	637	628	740	723	711	698

3.4.3. SEM

Microscopic micrographs of starting zeolite and TiO_2 encapsulated zeolite catalysts were collected using *LEO 1430 VP* scanning electron microscope equipped with *INCA Oxford EDX* facility as shown in Figure 3.8.

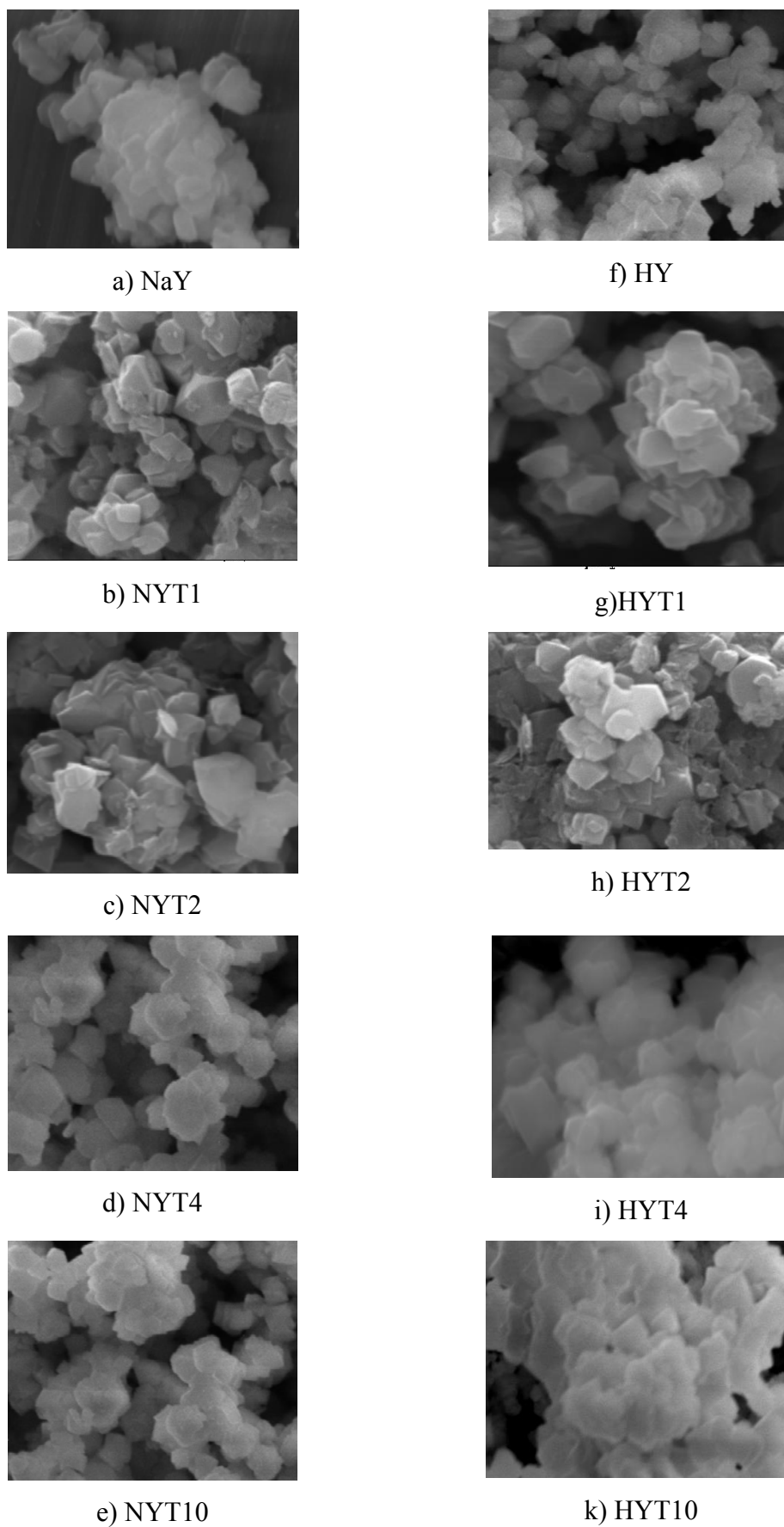


Figure 3.8: SEM images of TiO_2 encapsulated zeolite photocatalysts.

3.4.4. Diffuse Reflectance Spectroscopy

The encapsulation of various amounts of the nanocrystalline TiO_2 particles in zeolite were confirmed using the UV-Vis Diffuse Reflectance Spectroscopy (DRS) at room temperature in the range of 250-600 nm by *Shimadzu UV-3101PC spectrophotometer* with an integrating sphere [39-40]. All spectra were recorded with respect to BaSO_4 as reference. The diffuse reflectance spectra of TiO_2 (P25), NaY and TiO_2 encapsulated NaY is shown in Figure 3.9. A significant blue shift in the spectrum was observed for all catalysts as compared to bulk TiO_2 . The shift in the absorption bands of TiO_2 can attributed to the size quantization effects due to the presence of extremely small TiO_2 particles and/or the presence of highly unsaturated TiO_2 species having tetrahedral coordination [9, 19]. On other hand TiO_2 encapsulated NaY and HY catalysts exhibit absorption bands in the wavelength region of 330-370 nm. It was observed the absorption intensity increase with an increase in the content of TiO_2 . The DRS spectra of HY and TiO_2 encapsulated HY is shown in Figure 3.10. The band edge position could not be determined in TiO_2 encapsulated photocatalyst from the spectra after taking the differential of the DRS spectra. This may be due to the encapsulation, presence of small amount of TiO_2 in the catalyst.

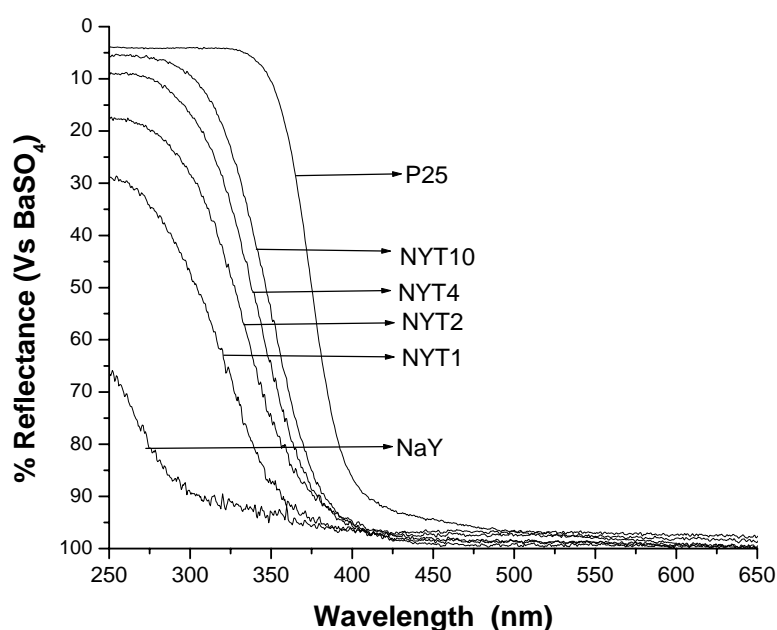


Figure 3.9: DRS spectra of TiO_2 encapsulated NaY zeolites, NaY zeolite, and P25.

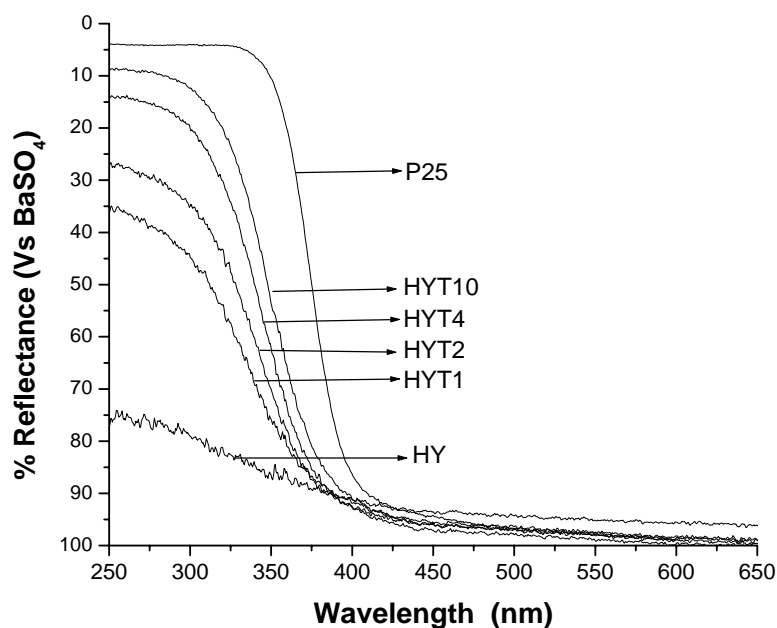


Figure.3.10: DRS spectra of TiO₂ encapsulated HY zeolite and P25.

3.4.5. Photocatalytic activity

The photocatalytic activity of TiO₂ encapsulated zeolites was evaluated by studying the decomposition of organic compounds like AP, NB, and dyes like MB, MG. The experimental setup, experimental procedure, are discussed in chapter 2 (Sections 2.4 and 2.5). The study the photocatalytic activity of the catalysts was studied by the irradiation experiments. The encapsulated catalysts contains very less amount of TiO₂ (1%, 2%, 4%, 10%), so weights of all encapsulated catalysts were taken 100mg in all irradiation experiments by keeping all other conditions same as the encapsulation of TiO₂ is very low in the zeolite.

3.5. Photocatalytic Degradation of Dyes

3.5.1 Spectroscopic Absorption measurements

First of all, the adsorption of dyes on NaY and HY zeolite was determined by spectrophotometer. These adsorption values for MB on NaY and HY were 26% and

40% respectively, while for MG it was 15% and 14% respectively. The photocatalytic degradation of MB and MG dye were carried out using TiO₂ encapsulated catalysts. The adsorption helps in the photocatalytic degradation process. The adsorption on the surface of catalysts before irradiation was determined by spectrophotometer and it was 23-25% for MB and 14-12% for MG in case of TiO₂ encapsulated in NaY zeolite, while it was 32-39% for MB and 10-13% for MG in TiO₂ encapsulated in HY catalysts. Figures 3.11 and 3.12 show UV-Vis absorption spectrum of degradation of MB with respect to time using NYT2 and HYT2 catalysts, respectively. Figures 3.12 and 3.13 show UV-Vis absorption spectrum of degradation of MG with respect to time using bare unloaded zeolite NaY, HY, NYT2 and HYT2 catalysts, respectively. It can be understood from the graph, the complete degradation of dyes took place using TiO₂ encapsulated zeolites. However, there was no measurable degradation of both the dyes with bare zeolites even though an adsorption of order of tens took place in these zeolites. The decrease in concentration of MB and MG after irradiation with respect to time using different encapsulated catalysts is shown in Figure 3.15.

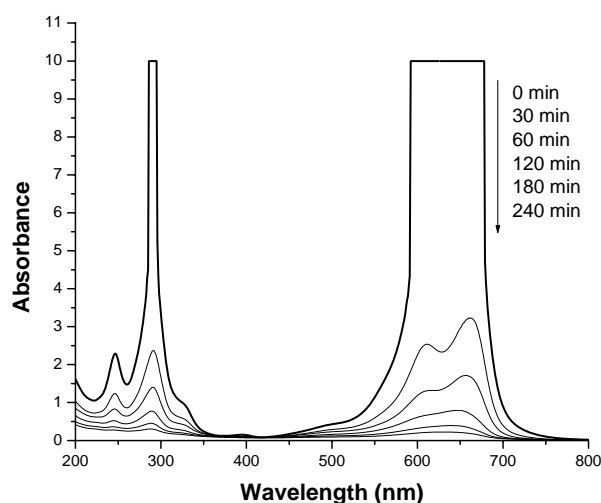


Figure 3.11: UV-Vis absorption spectra of degradation of MB using NYT2.

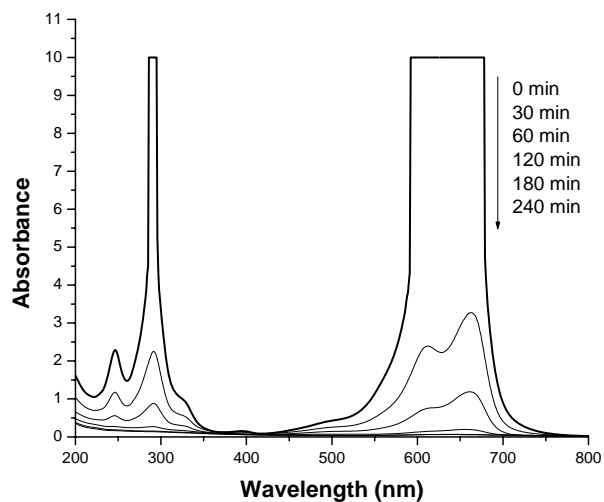


Figure 3.12: UV-Vis absorption spectra of degradation of MB using HYT2.

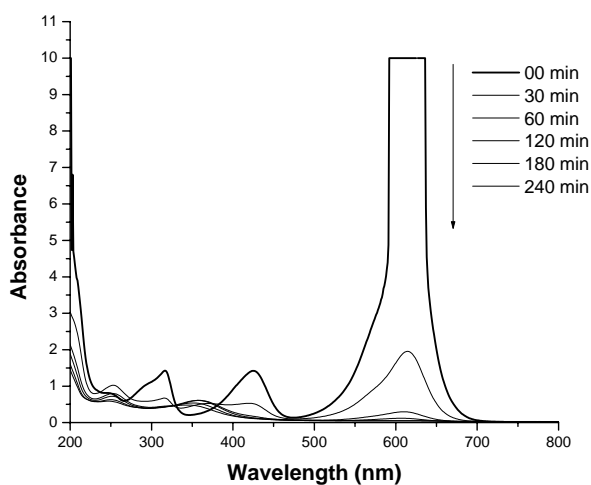


Figure 3.13: UV-Vis absorption spectra of degradation of MG using NYT2.

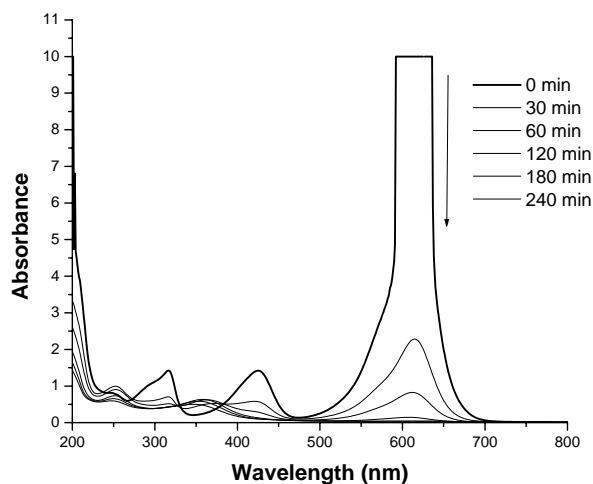
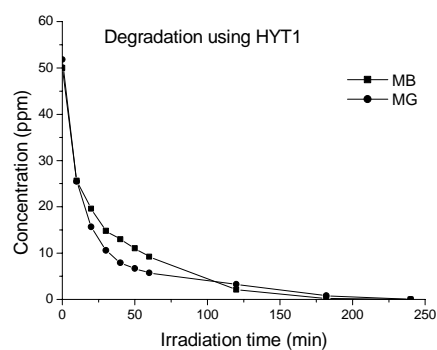
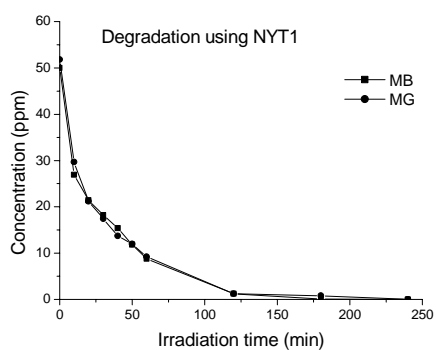
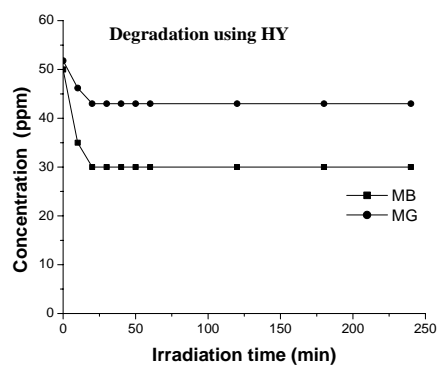
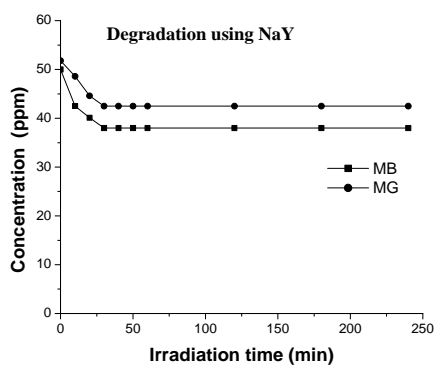


Figure 3.14: UV-Vis absorption spectra of degradation of MG using HYT2.



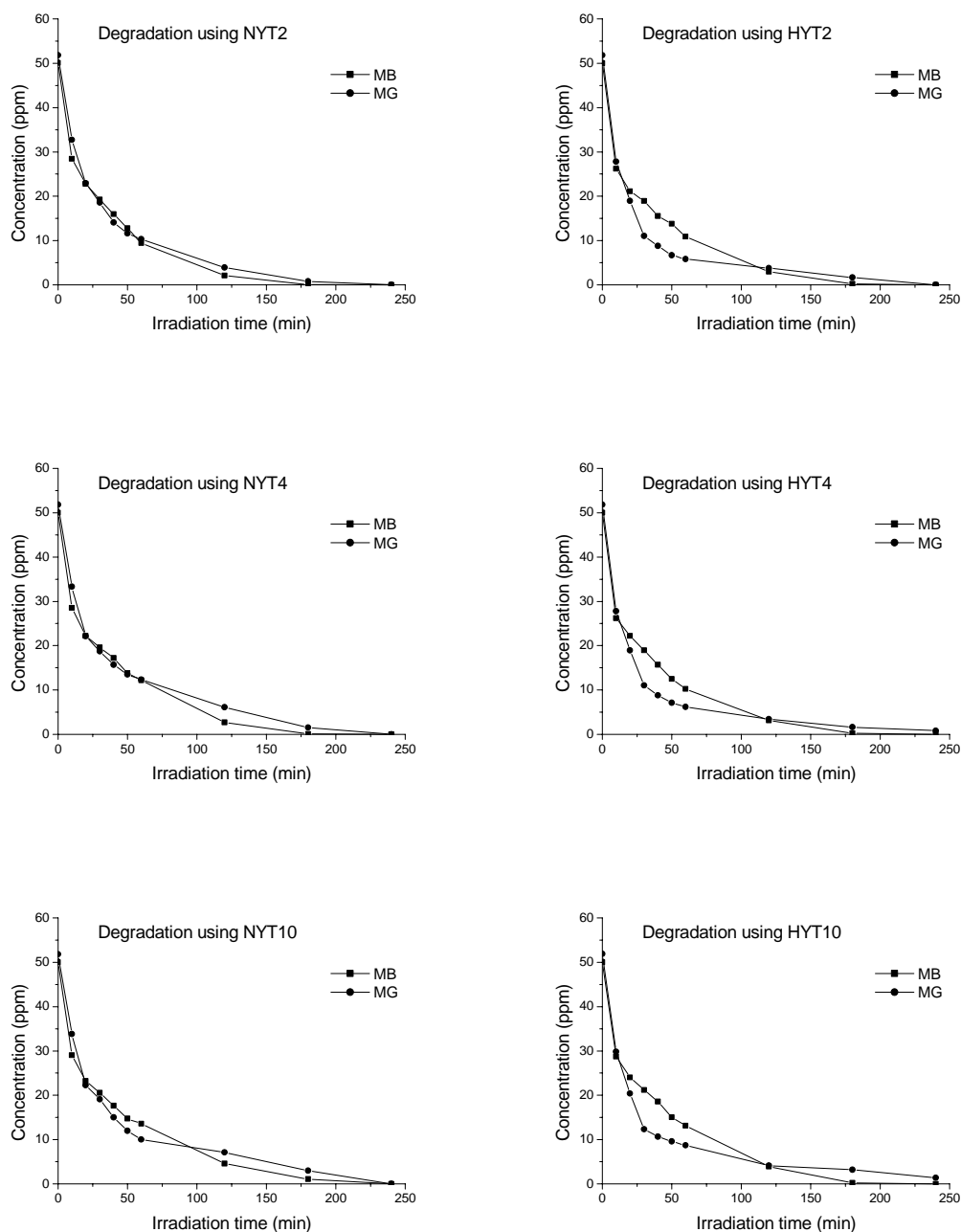
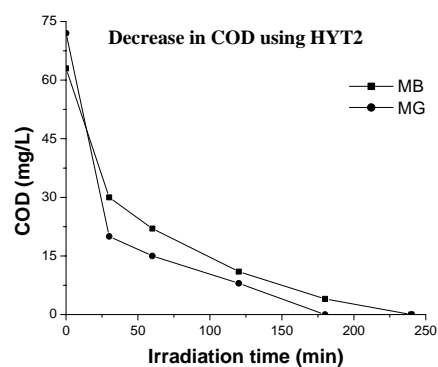
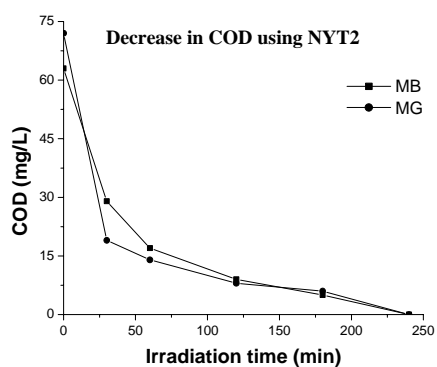
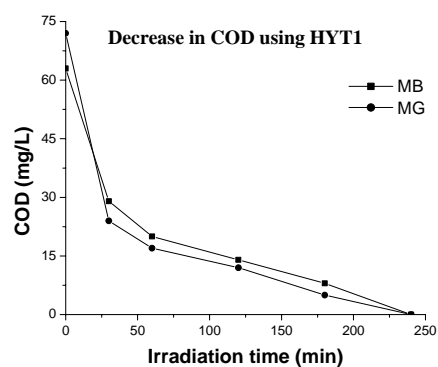
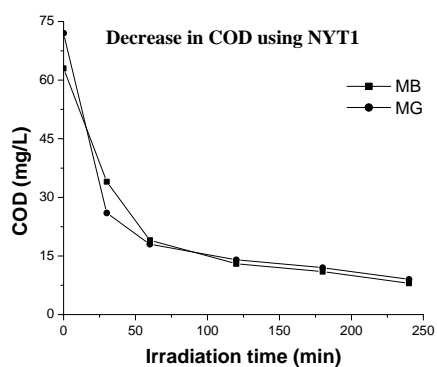
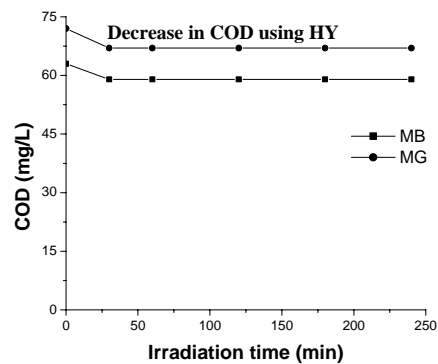
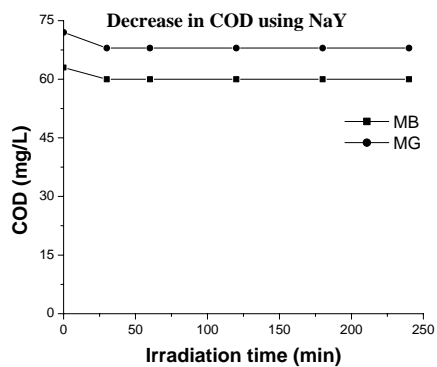


Figure 3.15: Degradation of MB and MG using bare NaY, HY and encapsulated photocatalysts.

3.5.2. Chemical Oxygen Demand (COD) Measurements

The chemical oxygen demand for the treated reaction mixture is shown in Figure 3.16 for dyes. For determination of COD also the procedure discussed in chapter 2 (Section 2.5) was repeated.

The decrease in COD was not observed in bare NaY and HY zeolites. The decrease in COD is observed using all the catalyst but only NYT2, NYT4 and HYT1 and HYT2 showed the complete removal of COD. The decrease in COD of malachite green showed the complete removal of COD. The decrease in COD of malachite green using all catalyst was faster than the methylene blue.



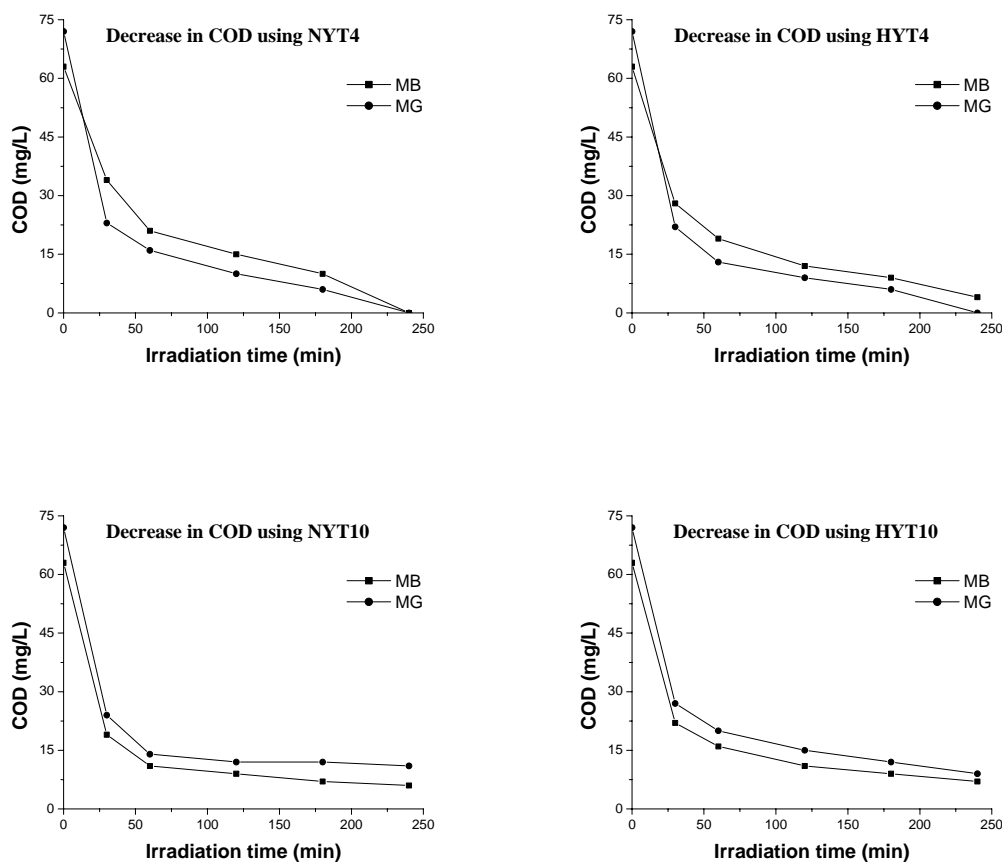


Figure 3.16: Decrease in COD of reaction mixtures of MB and MG using bare NaY, HY and encapsulated catalysts.

3.6. Photocatalytic Degradation of Organic Compounds

3.6.1. Spectroscopic Absorption Measurements

The photocatalytic degradation of AP and NB was carried out using TiO_2 encapsulated catalysts. These adsorption values for AP on NaY and HY were 12% and 14% respectively, while for NB it was 26% and 28% respectively. The adsorption on the surface of catalysts before irradiation was determined by spectrophotometer and it was 8-11 % for AP and 21-26% for NB in case of TiO_2 encapsulated in NaY zeolite, while it was 10-13% for AP and 20-22% for NB in TiO_2 encapsulated in HY catalysts. During the experiment it was observed that the 8-10% amount of organic

compound was adsorbed on the catalysts. Figures 3.17 and 3.18 show UV-Vis absorption spectrum of degradation of AP using NYT2 and HYT2 catalyst, respectively. Figures 3.19 and 3.20 show UV-Vis absorption spectrum of degradation of NB using NYT2 and HYT2 catalysts, respectively. It can be understood from the graph, the complete degradation of both organic compounds dyes took place using TiO_2 encapsulated zeolites. However, there was no measurable degradation of both the organic compounds with bare zeolites even though an adsorption of order of tens took place in these zeolites. Degradation of AP and NB with respect to time using all catalysts is shown in Figure 3.21.

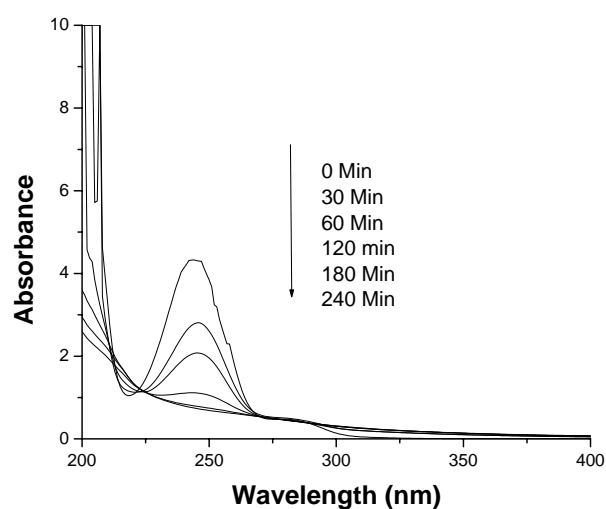


Figure 3.17: UV-Vis absorption spectra of degradation of AP using NYT2.

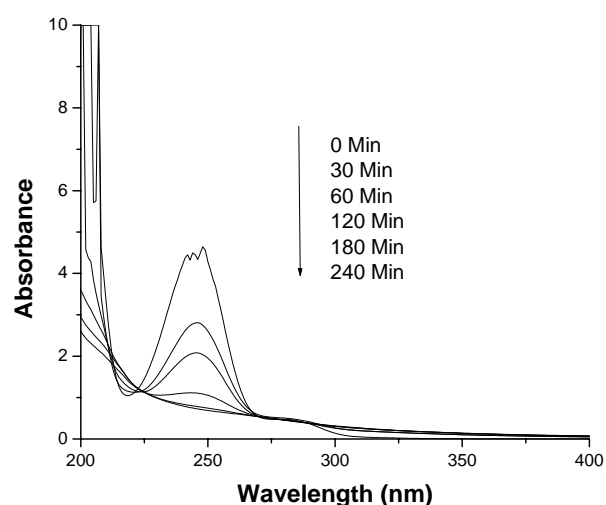


Figure 3.18: UV-Vis absorption spectra of degradation of AP using HYT2.

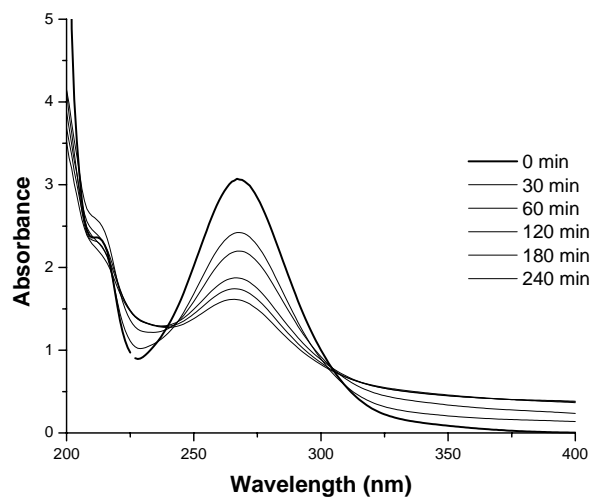


Figure 3.19: UV-Vis absorption spectra of degradation of NB using NYT2.

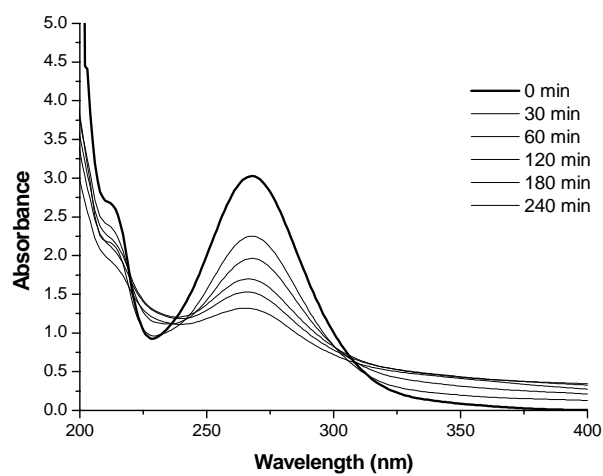
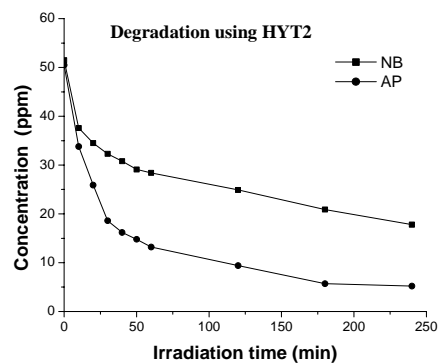
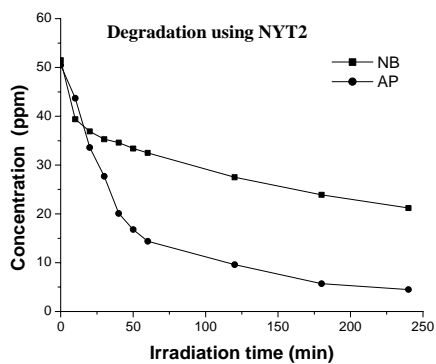
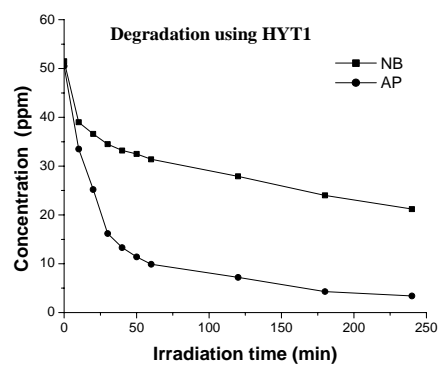
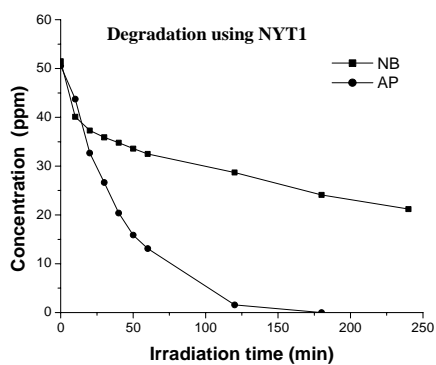
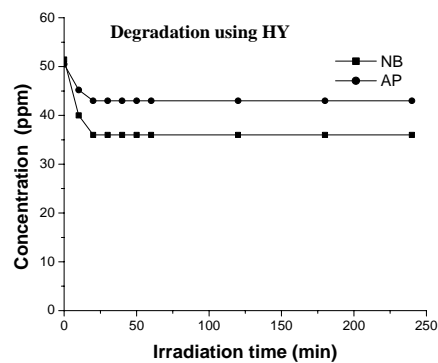
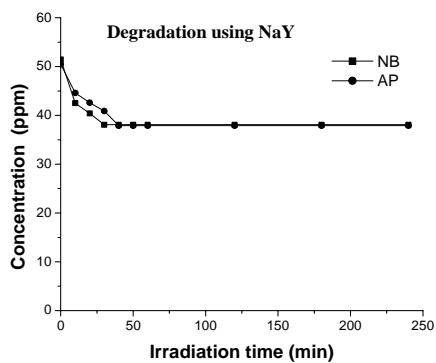


Figure 3.20: UV-Vis absorption spectra of degradation of NB using HYT2.



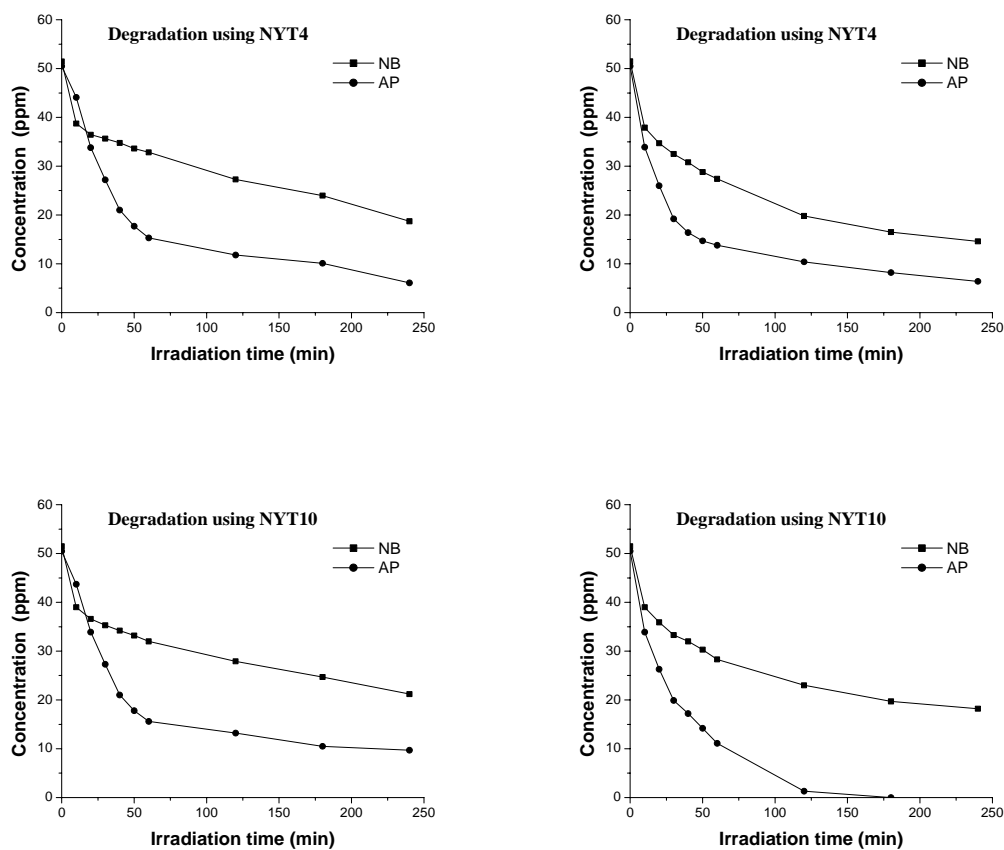
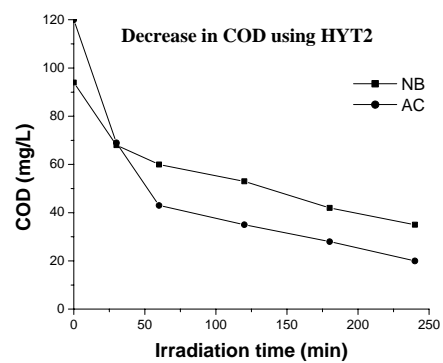
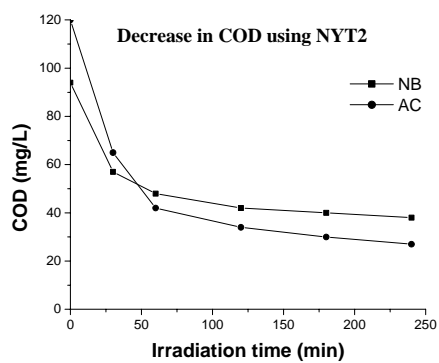
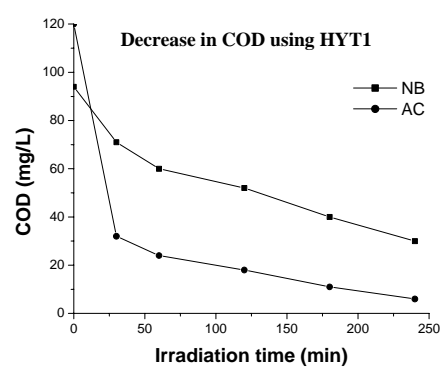
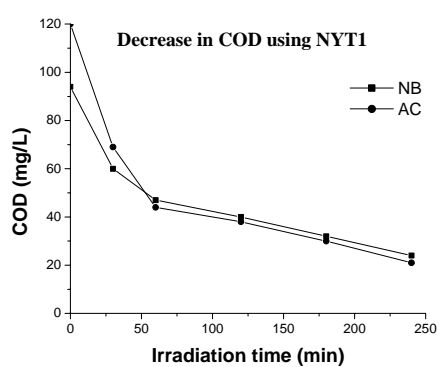
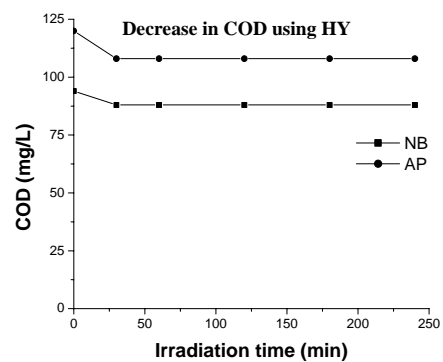
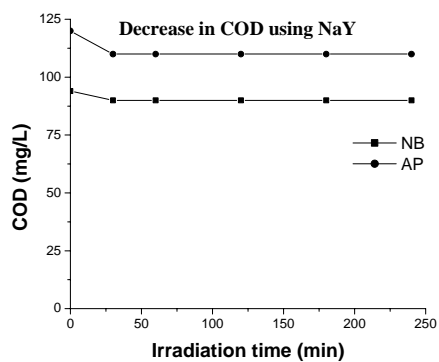


Figure 3.21: Degradation of organic compounds using bare NaY, HY and TiO₂ encapsulated photocatalysts.

3.6.2. Chemical Oxygen Demand (COD) Measurements

The chemical oxygen demand for the treated reaction mixture is shown in Figure 3.22 for organic compounds. The decrease in COD is observed using all the catalysts, but there was no complete removal of COD. The decrease in COD of AP using all catalyst was faster than the NB. The removal of COD was slow after 1 hour using all catalysts.



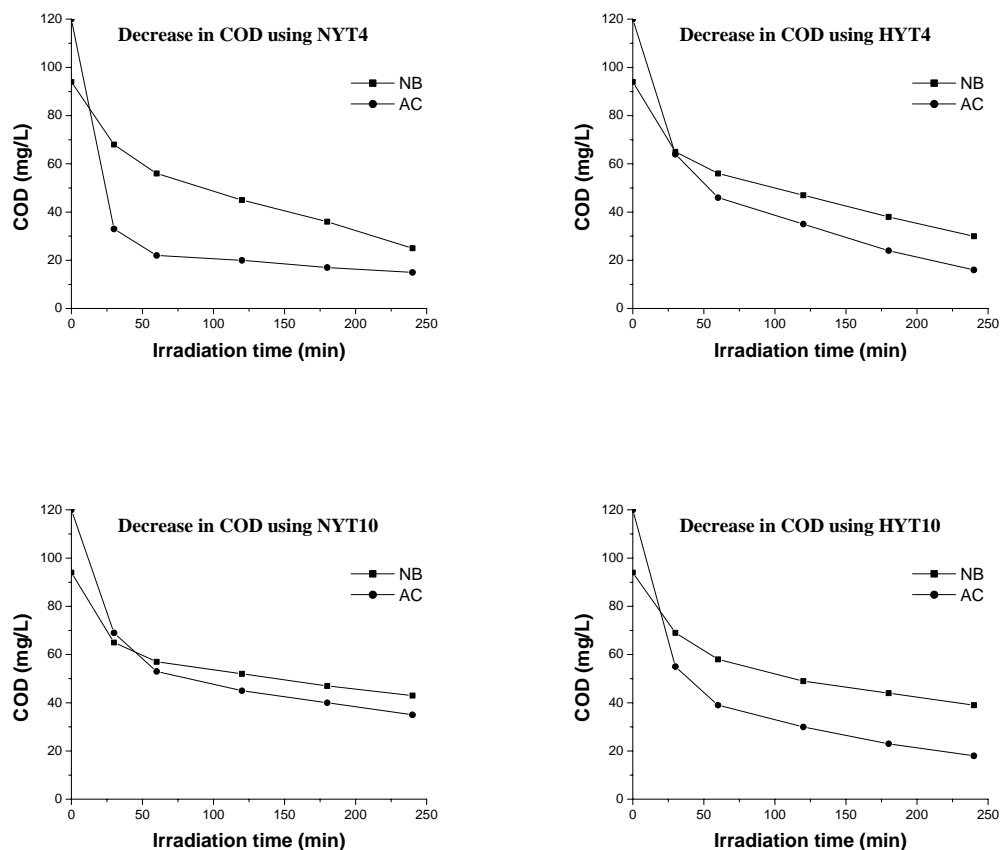


Figure 3.22: COD study of the reaction mixture organic compounds.

3.7. Results and Discussions

The organized channels and cages of zeolites provide a novel medium for carrying out photochemical reactions. Besides the confinement effect, the roles of zeolite framework and extra-framework cations have profound influence on the photocatalytic degradation of dyes and organic pollutants in water. These results indicate that by using zeolites as supports, highly dispersed titanium oxides can be produced, leading to the development of photocatalytic systems having high catalytic activity.

From above experiments, it is evident that although adsorption of dyes and organic compounds takes place on bare zeolite but there was no appreciable degradation of these substrates.

The encapsulation of a photocatalyst in the cavity of the zeolite is helpful for the adsorption of substrates on the surface of catalyst. The organized channels and cages

of zeolites provide a novel medium for carrying out photochemical reactions. Different forms of the zeolite like sodium and hydrogen are useful for the encapsulation of the TiO_2 . The surface area analysis by nitrogen adsorption shows that the increase in the surface area was observed after proton exchange. The TiO_2 encapsulation in zeolite expectedly reduces the surface area slightly. There was no significant more change seen in the SEM images of the catalyst after and before encapsulation of TiO_2 .

The XRD patterns of TiO_2 encapsulated NaY and HY zeolites agree with these of bare NaY and HY zeolite. This indicate that the framework of zeolite is unaltered after the encapsulation of TiO_2 and the TiO_2 particles residing in the zeolite cavities or channels are too small to be detected by XRD [41-43].

The entrapped titanium in zeolite was confirmed by UV-Visible Diffuse Reflectance spectroscopy. A significant blue shift was observed after TiO_2 encapsulation that increased with increase in amount of TiO_2 confirming the presence of TiO_2 particles in the zeolites. Such a blue shift to the shorter wavelength in the absorption band of titanium oxides can be attributed to the size quantization effect due to the presence of extremely small Ti-oxide particles and/or the presence of highly unsaturated Ti-oxide species having a tetrahedral coordination [44-46].

The adsorption properties of a zeolite plays major role in the photocatalytic degradation of dyes and organic compounds. The adsorption of the substrate molecules depend upon the surface area of the zeolite. The BET surface area of the NaY zeolite was $698\text{m}^2\text{g}^{-1}$. After H^+ ion exchange it was increased to $754\text{m}^2\text{g}^{-1}$. The adsorption of the substrate in percentage on the catalysts is shown in Table 3.3. The adsorption of substrate found decrease in the adsorption of substrate. The adsorption of substrate varies with the nature of substrate and the highest adsorption occurs in HYT1 catalyst for methylene blue which was 39%. This is because of the higher surface area of the HYT1 as compared to other TiO_2 encapsulated catalysts.

Table 3.3: Adsorption of substrate on TiO₂ encapsulated catalysts.

Catalyst	Adsorption of substrate (%)			
	MB	MG	AP	NB
NaY	26	15	12	26
NYT1	25	14	11	26
NYT2	25	13	10	24
NYT4	24	13	8	22
NYT10	23	12	8	21
HY	40	14	14	28
HYT1	39	13	13	22
HYT2	38	11	12	21
HYT4	36	11	12	21
HYT10	32	10	10	20

The prepared catalyst with low amount of TiO₂ has given good photocatalytic activity and showed that these can be used to immobilise the photocatalyst. The initial rate of degradation of dyes and organic compounds using TiO₂ encapsulated in zeolite with various weight percentage of TiO₂ is shown in Figures 3.23 and 3.24.

The initial rate of degradation of MB was higher than the MG. This may be due to the higher adsorption of MB on the surface of catalyst. Among the NaY photocatalyst, highest degradation (Table 3.3) was obtained using NYT2 for both dyes. While in HY photocatalyst high degradation was obtained in HYT2 for both dyes. The photocatalytic degradation activity was improved in HY photocatalyst in case of methylene blue while it was nearly same in case of malachite green as compared to NYT photocatalysts. These results show that the enhancement in photocatalytic activity is possible by TiO₂ encapsulation in zeolite cavities but it also depends upon the nature of substrate.

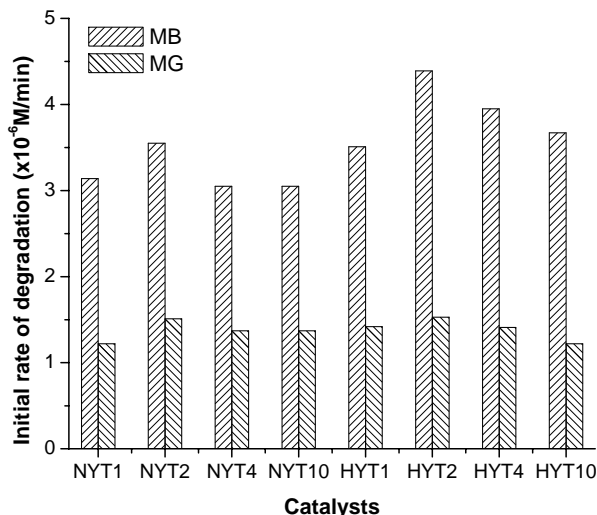


Figure 3.23: Initial rate of degradation of dyes using TiO₂ encapsulated catalysts.

The initial rate of photocatalytic degradation of organic compound using TiO₂ encapsulated photocatalysts is shown in Figure 3.24. In NaY photocatalyst, NYT2 has shown the highest initial rate of degradation for acetophenone and nitrobenzene. While NYT10 has shown the less initial rate of degradation this may be due to the agglomeration of TiO₂ particle in the cavity of zeolite. In HY photocatalyst, highest initial rate of degradation for acetophenone and nitrobenzene was observed in HYT2. HYT1 has shown the lowest initial rate of degradation of both the organic compounds.

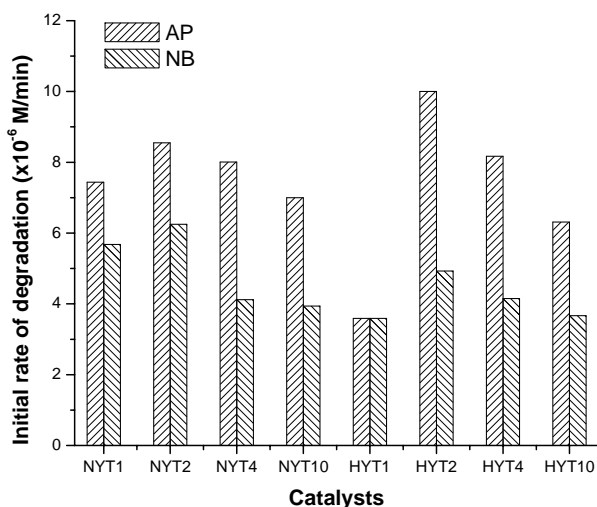


Figure 3.24: Initial rate of degradation of organic compounds using TiO₂ encapsulated catalysts.

The chemical oxygen demand for the treated reaction mixture is shown in Figure 3.16 and 3.22 for dyes and organic compounds. The decrease in COD is observed using all the catalyst but only NYT2 and HYT2 has shown the complete removal of COD for dyes. The decrease in COD of MG using all catalyst was higher than the MB. The removal of COD was higher in AP as compared to NB.

These results indicate that the structure of the zeolite plays an interesting role in the photocatalytic degradation of dyes and organic compounds and provide support for the photocatalyst. It is known that zeolite catalysts can stabilize reactive intermediates in several photochemical reactions [47-49].

From this study it is concluded that the TiO₂ encapsulated zeolite works as photocatalysts for the degradation of dyes and organic compounds. The photocatalytic activity of the photocatalysts depends upon the amount of loading of TiO₂ in the zeolite [12, 36, 44]. It is found that the lower loading of TiO₂ shows the better photocatalytic activity and it may be in the range of 2-10%. The encapsulation provides a space like a microreactor to the catalyst and because of this the recombination of electron-hole pair avoided which helps for degradation of the substrate molecules. The oxygen adsorption in the zeolite, which is essential to the electron accepting process on TiO₂, may be also one of the important factors in the photocatalytic degradation of substrate. The photocatalyst in the cavity is of nanometer size that shifts the absorption towards higher wavelength and results in more light absorption by the photocatalyst. The low amount of TiO₂ encapsulation implies favourable light collection as there is little loss of light due to the zeolite support and efficient access to the photoactive sites and species. The change in the capacity of supports to adsorb substrate is an important factor for the photocatalytic degradation of the substrates. However, the structural studies do not provide strong evidence for the detailed nature of the TiO₂ surface.

3.8. References

- [1] R. W. Mathews, *J. Phys. Chem.* 102 (1998) 6853.
- [2] M. A. Anderson, H. Kikkawa, M. Edwards, *J. Catal.* 127 (1991) 167.
- [3] K. Hofstandler, R. Bauer, S. Novalic, *Environ. Sci. Technol.* 28 (1994) 670.
- [4] R.W. Mathews, *J. Phys. Chem.* 91 (1987) 405.
- [5] S. Sato, *Langmuir* 14 (1998) 1156.
- [6] K. Vinodgopal, S. Hotchandani, P.V. Kamat, *J. Phys. Chem.* 97 (1993) 9040.
- [7] H. Yoneyama, S. Haga, S. Yamanaka, *J. Phys. Chem.* 93 (1989) 4833.
- [8] K.J. Green, *J. Chem. Soc., Faraday Trans.* 89 (1993) 1816.
- [9] X. Liu, K.K. Iu, J.K. Thomas, *J. Chem. Soc., Faraday Trans.* 89 (1993) 1861.
- [10] R. W. Mathews, *Water Res.* 24 (1990) 653.
- [11] J. Sabate, M. A. Anderson, M. A. Aguado, *J. Mol. Catal.* 71 (1992) 57.
- [12] Y. Xu, C. H. Langford, *J. Phys. Chem.* 99 (1995) 11501.
- [13] K. J. Green, *J. Chem. Soc., Faraday Trans.* 89 (1993) 1816.
- [14] X. Liu, K. K. Iu, J. K. Thomas, *Chem. Phys. Lett.* 195 (1992) 163
- [15] I. R. Beattie, V. Faecett, *J. Chem. Soc. A* (1967) 1583.
- [16] H. Chen, A. Matsumoto, N. Nishimiya, K. Tsutsumi, *Colloids Surf. A: Physicochem. Eng. Aspects* 157 (1999) 295.
- [17] M. Anpo, *Catal. Surv. Jpn.* 1 (1997) 169.
- [18] H. Yamashita, Y. Ichihashi, M. Anpo, M. Hashimoto, C. Louis, M. Che, *J. Phys. Chem.* 100 (1996) 16041.
- [19] H. Yamashita, Y. Ichihashi, M. Harada, G. Stewart, M. A. Fox, M. Anpo, *J. Catal.* 158 (1996) 97.
- [20] D. W. Breck, *Zeolite Molecular Sieves*, Krieger, Malabar, 1984.
- [21] A. Dyer, *An Introduction to Zeolite Molecular Sieves*, Wiley, NewYork, 1988.
- [22] H. Van Bekkum, E. M. Flanigen, P. A. Jacobs, J. C. Jansen (Eds.), *Introduction to Zeolite Science and Practice*, second ed., Elsevier, Amsterdam, 2001.
- [23] G. A. Ozin, A. Kuperman, A. Stein, *Angew. Chem. Int. Ed. Engl.* 28 (1989) 359.
- [24] G. D. Stucky, J. E. MacDougall, *Science* 247 (1990) 669.
- [25] A. Braun, G. Ihlein, F. Laeri, U. Nöckel, G. Schultz-Ekloff, F. Schüth, U. Veitze, Ö. Weiss, D. Wöhrle, *Appl. Phys. B* 70 (2000) 335.
- [26] F. Marlow, J. Caro, L. Werner, J. Kornaowski, S. Dähne, *J. Phys. Chem.* 97 (1993) 11286.
- [27] S. Anandan, M. Yoon, *Journal of Photochem. Photobio. C: Photochemistry Reviews* 4 (2003) 5.

- [28] S. Hashimoto, *Journal of Photochem. Photobio. C: Photochemistry Reviews* 4 (2003) 19.
- [29] M. Matsuoka, M. Anpo, *Journal of Photochemistry and Photobiology C: Photochemistry Reviews* 3 (2003) 225.
- [30] F. Blatter, H. Sun, S. Vasenkov, H. Frei, *Catalysis Today* 41 (1998) 297±309
- [31] F. Blatter, H. Erei, *J. Am. Chem. Soc.* 115 (1993), 7501.
- [32] F. Blatter, H. Erei, *Am. Chem. Soc.* 116 (1994), 1812.
- [33] F. Blatter, H. Erei, *J. Am. Chem. Soc.* 116(1994) 7951.
- [34] F. Blatter, F. Moreau, H. Frei, *J. Phys. Chem* 98 (1994)13403.
- [35] F. Blatter, H.Sun, H. Frei, *Cat. Lett.* 35(1995) 1.
- [36] F. Blatter, H.Sun, H. Frei, *J. Chem. Eur.* 2 (1996) 113.
- [37] C. Bärlocher, W.M. Meier, D.H. Olsen, *Atlas of Zeolite Framework Types*, Elsevier, Amsterdam, 2001.
- [38] S. J Gregg, K. S. W. Sing. *Adsorption, Surface Area and Porosity*, 2nd Ed; Academic Press: New York, 1982.
- [39] M. Gratzel *Heterogeneous Photochemical Electron Transfer*. CRC Press, Boca Raton, FL.
- [40] W. Wang, M. Gu, Y. Jin, *Materials Letters*, 57 (2003) 3276.
- [41] Y. Xu, C. H. Langford, *J. Phys. Chem.* 99 (1995) 11501.
- [42] Y. Kim, M. Yoon, *J. Mol. Cat. A.: Chemical* 168 (2001) 257.
- [43] J. Chen, L. Eberlein, C. H. Langford, *J. Photochem. And Photobio. A: Chemistry* 148 (2002) 183.
- [44] X. Liu, K. K. Iu, J. K. Thomas, *J. Chem. Soc., Faraday Trans.* 89 (1993) 1861.
- [45] M. Anpo, H. Nakaya, S. Kodama, Y. Kubokawa, K. Domen, T. Onishi, *J. Phys. Chem.* 90 (1986) 1633.
- [46] M. Anpo, H. Yamshita, Y. Ichihashi, Y. Fujii, M. Honda, *J. Phys. Chem. B* 101 (1997) 2632.
- [47] K. B. Yoon, *Chem. Rev.*, 93 (1993) 321.
- [48] P. K. Dutta, J. A. Incavo, *J. Phys. Chem.* 91 (1987) 4443.
- [49] S. Zhang, N. Fujii, Y. Nosaka, *J. Mol. Cat. A: Chemical* 129 (1998) 219.

Chapter - 4

MODIFICATION OF PHOTOCATALYST- ENCAPSULETED ZEOLITES

4.1. Introduction

The zeolite cavity offers a solid support to the catalyst and acts like a micro reactor. The combination of a zeolite host and photoactive sites renders solid photocatalyst in which the high surface area and the adsorbent capacity provided by zeolites are expected to increase the efficiency of the photocatalytic process. In addition, zeolite pores define a compartmentalized space in which multi-component systems can be easily assembled by a stepwise procedure. Other positive effects derived from the encapsulation of a guest inside zeolites are a higher photo stability of the sensitizer, the observation of quantum size effects for semiconductor clusters and a favourable polar environment for photoinduced electron transfer.

Zeolites have unique property of involving metal ions within the zeolite framework or cavities, which has opened new possibilities in different areas, not only in catalysis [1-3] but also in various photochemical processes [4-8]. Zeolites has both acidic and basic sites present in it that act as a catalyst for many reactions [9], including side chain alkylation of toluene [10], condensation reaction [11] and selective alkylation of aromatic compounds containing oxygen and nitrogen [12]. The photocatalytic reactions such as the decomposition of NO into N₂ and O₂ [13-20], the degradation of organic impurities in water [21-23], the photo-oxidation reaction of hydrocarbons [24-25], the photo-induced metathesis reaction of alkanes [26-27], and the reduction of CO₂ with H₂O to produce CH₄ and CH₃OH [28-31] were reported in the literature using zeolites. These photocatalytic reactions were found to proceed with a high efficiency and selectivity, displaying quite different reaction mechanisms from those observed on semiconducting photocatalysts, in which the photoelectrochemical reaction mechanism or charge separation plays an important role in determining the efficiency. These findings indicate that a fundamental understanding of the coordination structure and electronic state of the active species is important in the design and development of applicable photocatalysts having high reactivity and selectivity. It is reported that exchangeable cation even enhances the catalytic property of zeolites to a remarkable extent [32]. An important development in zeolite catalyst design would be to predict the influence and activity of different cations for specific catalytic reactions. So far there are many theoretical studies with the

influence of zeolite structure and composition on acid strength [33-34]. There is scant literature using reactivity descriptors [35].

Zeolites are porous crystalline aluminosilicates having a uniform pore structure and exhibiting ion-exchange behaviour. The framework of zeolite consists of SiO_4 and AlO_4 tetrahedra sharing oxygen ions located at their apices, thus resulting in the general framework formula $(\text{AlO}_2)_x(\text{SiO}_2)_{n-x}$, where n is the number of tetrahedral per unit cell, and $x \leq n/2$. Since aluminium is trivalent, every AlO_2 unit carries a negative charge, which is compensated by a positive charge associated with a cation. Therefore, the ion exchange capacity of a zeolite depends on the chemical composition, with when a higher ion-exchange capacity was observed in low $\text{SiO}_2/\text{Al}_2\text{O}_3$ ratio [36]. The specific ion-exchange capacity varies with the structure of the zeolite and the exchanged cation. The electronic structure of a zeolite material can be regarded as superposition of the electronic structure of the framework of the charge compensation cations of the solvent molecules and guest species. The charge compensating cations cause new electronic states some of which may lie within the band gap region. They can interact with each other depending on their nature and the mean distance between them. The presence of solvent molecules, usually water influences their interaction with the zeolite framework. The electronic structure of the zeolite and the charge compensating cations are not influenced by each other as long as the solvation shields the cations from coordination to zeolite oxygen. The cations exchanged zeolites have attracted interest in the field of catalysis because of physical adsorption or chemisorption of small molecules. For example copper exchanged zeolite can be applied not only as a catalyst in organic synthesis [37] but also for the conversion of NO_x into N_2 and O_2 [38-41] and for separation procedures like diene/olefin separation. Silver exchanged zeolites were found to oxidize water in a photochemical reaction [41].

4.1.1. Ion exchange

Zeolite Y possesses a variety of cations positions. The more common ones are SI in the hexagonal prism (octahedral coordination by 6 framework-O), site SI' in the centre of the 6R just outside the D6R in the sodalite cage, SII in the centre of 6R just outside the sodalite cage, site II' similarly in the centre of the 6R, but displaced just inside the

sodalite cage, and SIII in the supercage on a 4R. If SI is occupied, then SI' contains no cations, and if SII is occupied, there are no cations in SII'. The framework structure of zeolite NaY is shown in Figure 4.1.

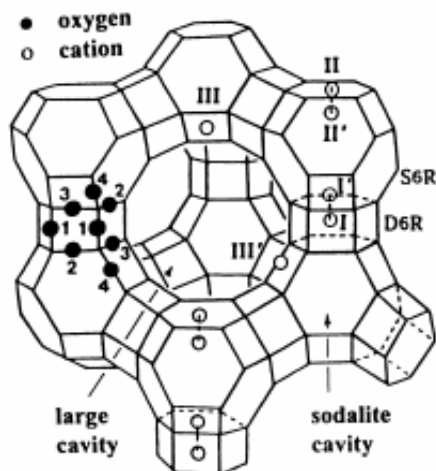


Figure 4.1: Framework structure of zeolite Y. Near the centre of each line segment is an oxygen atom. The numbers 1 to 4 indicates the different oxygen atoms. Extra framework cation positions are labelled with Roman numerals.

When the zeolite is immersed in an aqueous electrolyte, the zeolite ions communicate with external solution, resulting in an exchange of ions between the solid phase and the solution. Since the anionic charges of the framework are fixed, the number of cationic charges within the zeolite pores is also constant. Depending on particular zeolites, the pores may consist of one type of channel having essentially the same width throughout the unit cell; there may be two types of channels with different diameters and channels may or may not intersect or the intracrystalline void may consist of one or more type of cages connected by smaller opening. Anhydrous cations i.e. quaternary ammonium ions have definite size. If they are larger than the pore opening of the zeolite structure, they are unable to enter or leave the pore system, and ion exchange cannot take place. The rate of ion exchange depends on the concentration of ions of a size capable of penetrating the pores of the zeolite. At ambient temperature, a solution of a large hydrated ion may contain very few partially hydrated ions of a size smaller than the pore opening of the zeolite so that the exchange is very slow. The rate of exchange increases with increase in temperature [42].

In the present study the TiO_2 encapsulated zeolites were exchanged with different metal ions like Ag, Co, Cu, Fe, and Ni by ion exchange method. The synthesized

catalysts were characterized for its physical properties using XRD, SEM, DRS and BET analysis. The effect of post modification was studied by the degradation of dyes like MB and MG and organic compounds like AP and NB.

4.2. Post Synthesis Modification of Photocatalyst-Encapsulated Zeolites

4.2.1. Chemicals & Materials

Titanium tetra isopropoxide (97%), Copper acetate LR grade, Nickel acetate were procured from *Aldrich* USA. Silver nitrate AR grade was procured from Ranbaxy, *Fine Chemical Limited*, India. Cobalt chloride, Ferric chloride, Methylene blue, Malachite green, and Nitrobenzene AR grade (99.0%) were procured from *s. d. Fine Chem. Limited*, India. and Acetophenone AR grade and COD Standard chemical reagents were purchased from E. Merck. P-25 titanium dioxide was procured from *Degussa Corporation, Germany*.

4.2.2. Preparation of the catalysts

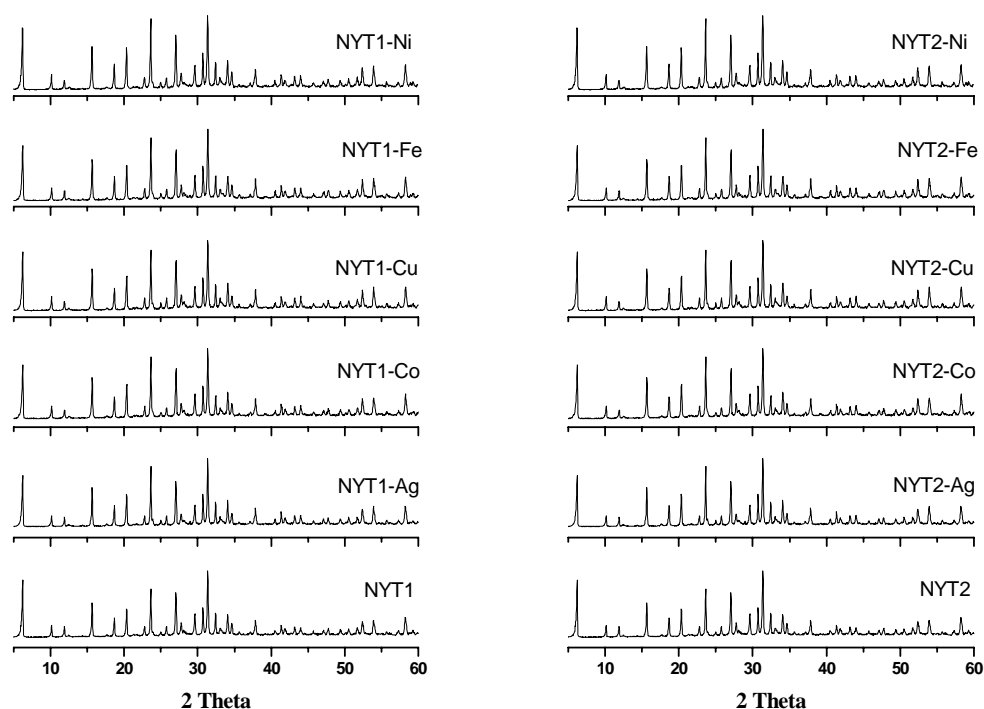
TiO₂ encapsulated catalysts were prepared by the procedure described in chapter 3. The post modification of the photocatalyst encapsulated zeolite was carried out by ion exchange method. The TiO₂ encapsulated catalyst was heated in metal salt solution at 353K for 4 hours for ion exchange. The residue was filtered and washed with hot distilled water. The above cycle was repeated three times to get complete exchange of sodium and hydrogen. The sample was dried at a temperature 353K for 8 hours and then calcined at 823K for 6 hours. The catalyst thus obtained is termed as NYT1-Ag, where NYT1 (Silver ion exchange in 1% TiO₂ encapsulated NaY catalysts)

4.3. Characterisation of Encapsulated Photocatalyst

All the synthesized photocatalysts were characterised for their physical characterisation and photocatalytic activity as discussed in following section.

4.3.1. X-ray Powder Diffraction

X-ray powder diffraction studies at ambient temperature were carried out using *Philips X'pert MPD system* in the 2θ range 5-60 degrees using $\text{CuK}\alpha 1$ ($\lambda = 1.54056\text{\AA}$). The crystallinity of the TiO_2 encapsulated zeolite sample was found same after post modification using different metal ion exchange. There was no peak obtained after ion exchange because of low amount of ion exchange XRD pattern of the post modified TiO_2 encapsulated NaY and HY catalyst are Figures 4.2 and 4.3 respectively.



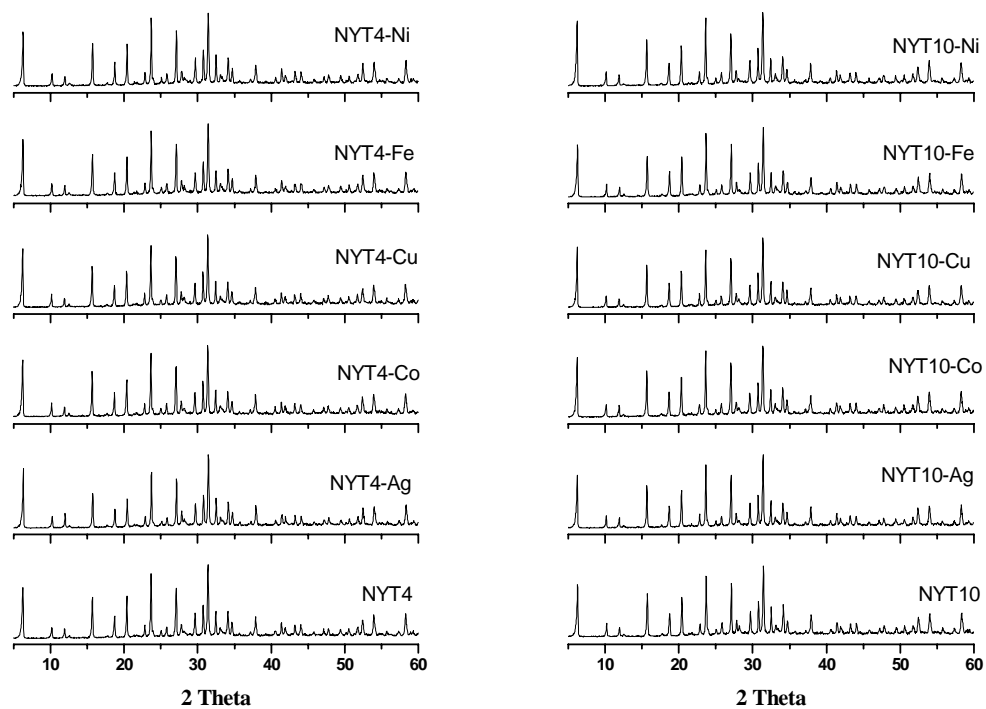
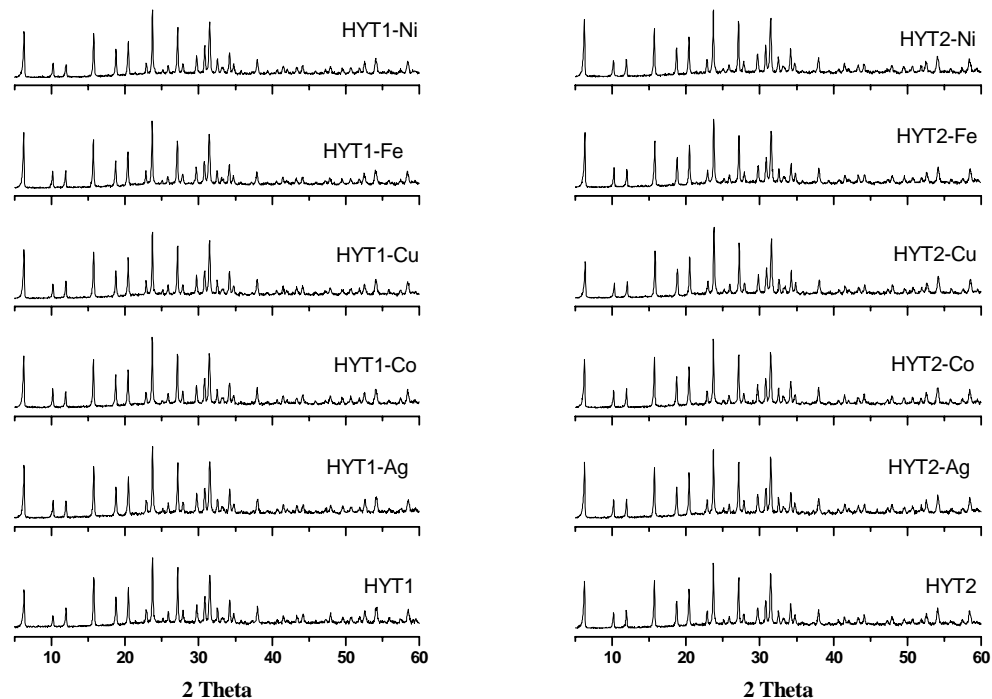


Figure 4.2: X-ray diffraction pattern of post modified NaY zeolite catalysts



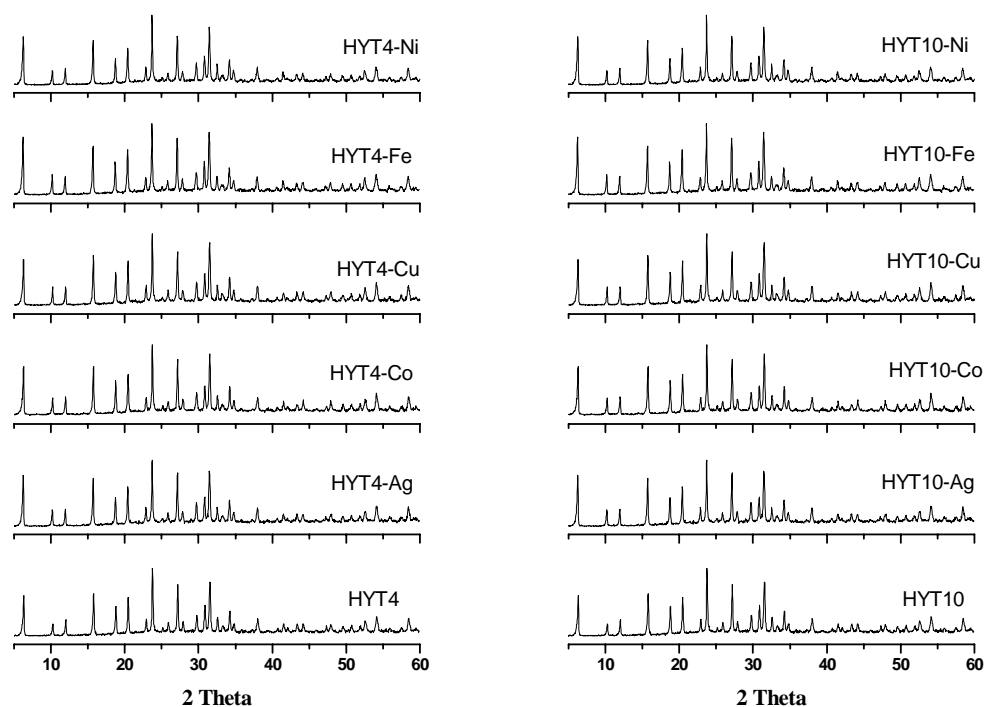


Figure 4.3: X-ray diffraction pattern of post modified HY zeolite catalysts

4.3.2. Surface area analysis (N₂ adsorption)

Specific surface area, pore volume and pore size distributions of calcined encapsulated photocatalyst samples were determined from N₂ adsorption-desorption isotherms at 77K (ASAP 2010, Micromeritics, USA). Surface area and pore size distribution were determined using the BET equation and BJH method respectively [43]. The BET surface area of the TiO₂ encapsulated catalysts in NaY and HY zeolites catalysts are given in Table 4.1.

Table 4.1: Surface area of post modified catalysts.

Catalyst	BET Surface Area (m ² g ⁻¹)	Catalyst	BET Surface Area (m ² g ⁻¹)
NYT1-Ag	668	HYT1-Ag	730
NYT1-Co	663	HYT1-Co	727
NYT1-Cu	652	HYT1-Cu	717
NYT1-Fe	658	HYT1-Fe	723
NYT1-Ni	662	HYT1-Ni	727
NYT2-Ag	650	HYT2-Ag	714
NYT2-Co	648	HYT2-Co	710
NYT2-Cu	638	HYT2-Cu	705
NYT2-Fe	640	HYT2-Fe	717
NYT2-Ni	645	HYT2-Ni	710
NYT4-Ag	627	HYT4-Ag	704
NYT4-Co	623	HYT4-Co	698
NYT4-Cu	620	HYT4-Cu	689
NYT4-Fe	618	HYT4-Fe	697
NYT4-Ni	628	HYT4-Ni	700
NYT10-Ag	620	HYT10-Ag	690
NYT10-Co	613	HYT10-Co	684
NYT10-Cu	619	HYT10-Cu	672
NYT10-Fe	608	HYT10-Fe	675
NYT10-Ni	618	HYT10-Ni	680

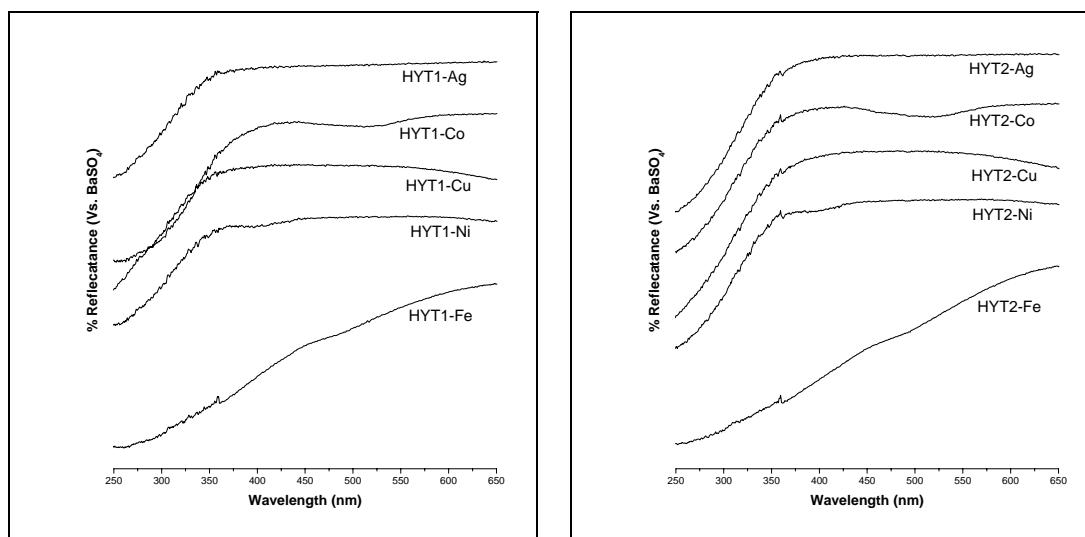
4.3.3. SEM

Microscopic analysis of starting zeolite and post modified TiO₂ encapsulated zeolite samples were done by using *LEO 1430 VP* scanning electron microscope equipped with *INCA Oxford* EDX facility. All the images of the catalysts were nearly same as compare to the TiO₂ encapsulated zeolites.

4.3.4. Diffuse Reflectance Spectroscopy

The spectra of post modified zeolites with different metal ion exchange were recorded using the Diffuse Reflectance Spectroscopy (DRS) (*Shimadzu UV-3101PC*) equipped with an integrating sphere at room temperature in the wavelength range of 250-600nm. All The spectra were recorded with BaSO₄ as a reference [44-45].

The diffuse reflectance spectra of post modified zeolites are shown in Figure 4.4. The difference in the spectra confirms presence of the different metal ion in zeolite. Same trend was observed in case of same metal ion exchange catalysts with different percentage of TiO₂.



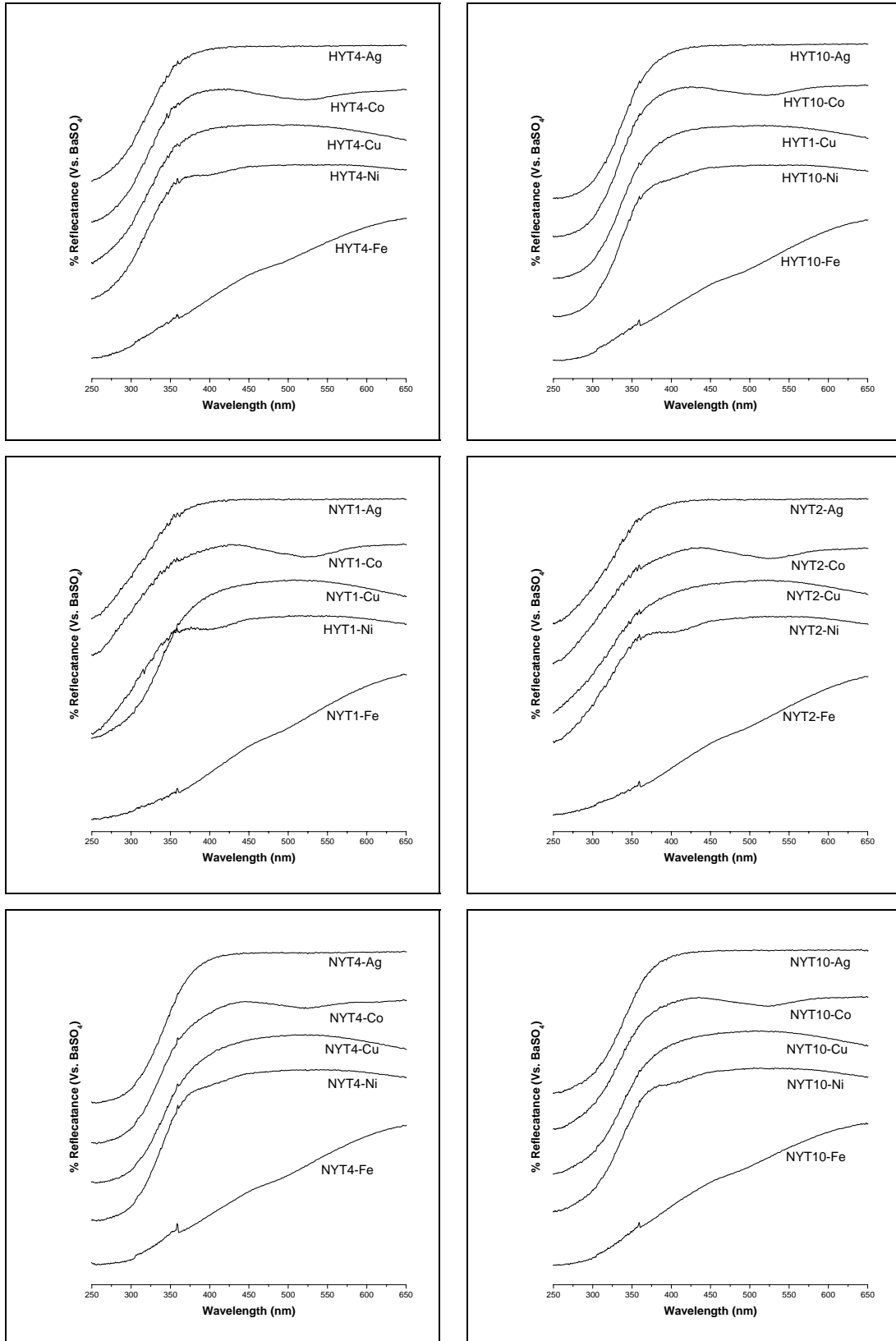


Figure 4.4: DRS spectra of post modified TiO_2 encapsulated NaY and HY catalysts.

4.3.5. Photocatalytic activity

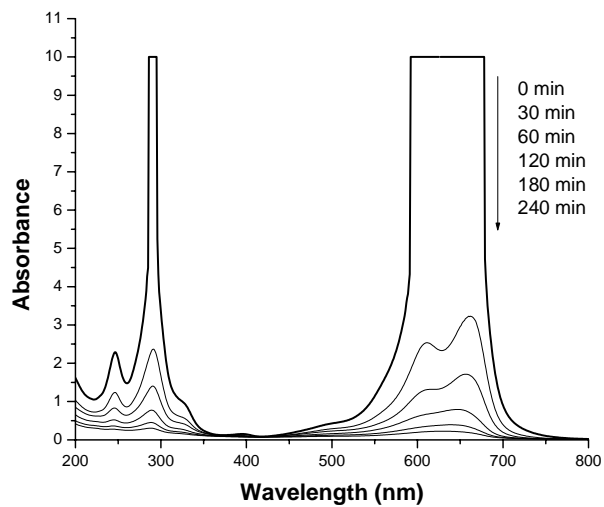
The photocatalytic activity of post modified catalysts was evaluated by studying decomposition of organic compounds like AP, NB, and dyes like MB, MG. The same experimental setup and experimental procedure, discussed in Chapter 2 (Section 2.4 and 2.5) was followed to carry out the irradiation experiments to study the photocatalytic activity of the catalysts. The catalyst weight 100mg was taken in all irradiation experiment while keeping all other conditions same.

4.4. Photocatalytic Degradation of Dyes

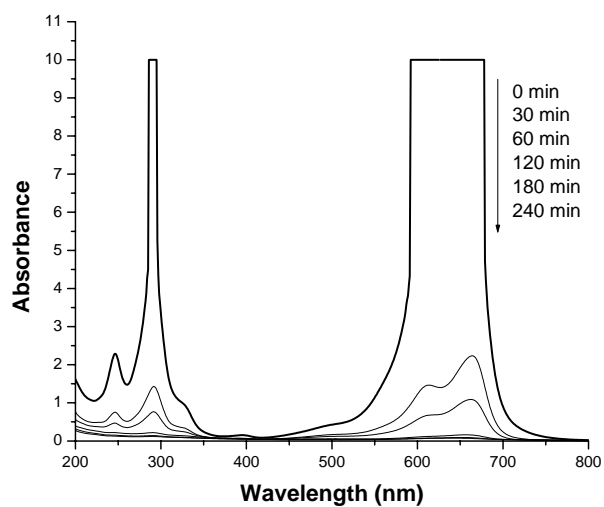
The photocatalytic degradation of MB and MG dye was carried out using post modified catalysts. The adsorption on the surface of catalysts before irradiation was determined by spectrophotometer and it was nearly same as TiO₂ encapsulated in NaY and HY zeolite. The adsorption was 23-25% for MB and 12-14% for MG in case of post modified NaY catalysts, while it was 32-39% for MB and 10-13% for MG in post modified HY catalysts.

4.4.1. Degradation of MB

The UV-Vis spectrum of degradation of MB with respect to time using post modified catalysts. It was nearly same as compared to TiO₂ encapsulated zeolites as shown in Figure 4.5 and Tables 4.2 and 4.3. The decrease in concentration of MB upon irradiation of UV light using post modified NaY and HY catalyst respectively is shown in Tables 4.2 and 4.3. The decrease in COD of MG using different post modified NaY and HY catalyst are shown in Tables 4.4 and 4.5. The silver cation exchanged encapsulated catalysts showed higher photocatalytic activity as compare to other ion exchanged catalysts for both dyes.



(a) UV-Vis absorption spectra of degradation of MB using NYT1-Ag



(b) UV-Vis absorption spectra of degradation of MB using HYT1-Ag

Figure 4.5: UV-Vis absorption spectra of degradation of MB using (a) NYT1-Ag & (b) HYT1-Ag.

Table 4.2: Degradation of MB using post modified NaY catalysts under irradiation of UV light.

Catalysts	Time in minutes					
	0	30	60	120	180	240
NYT1-Ag	49.9	11.5	01.6	00.0	00.0	00.0
NYT2-Ag	49.9	15.0	07.0	01.6	00.0	00.0
NYT4-Ag	49.9	19.5	12.2	02.9	00.0	00.0
NYT10-Ag	49.9	23.0	13.4	04.5	00.1	00.0
NYT1-Co	49.9	12.5	04.5	01.3	00.0	00.0
NYT2-Co	49.9	16.3	07.7	02.2	00.2	00.0
NYT4-Co	49.9	16.6	08.0	03.2	00.3	00.0
NYT10-Co	49.9	18.9	08.6	03.4	00.4	00.0
NYT1- Cu	49.9	17.6	09.6	02.6	00.0	00.0
NYT2-Cu	49.9	20.2	09.6	02.6	00.0	00.0
NYT4-Cu	49.9	22.4	11.2	03.2	0.3	00.0
NYT10-Cu	49.9	22.4	11.5	03.2	00.3	00.0
NYT1-Fe	49.9	17.6	07.7	01.9	00.0	00.0
NYT2-Fe	49.9	16.3	09.3	02.6	00.0	00.0
NYT4-Fe	49.9	17.6	09.3	02.6	00.0	00.0
NYT10-Fe	49.9	18.9	08.6	03.2	00.3	00.0
NYT1-Ni	49.9	17.6	07.7	01.9	00.0	00.0
NYT2-Ni	49.9	19.2	09.0	02.2	00.0	00.0
NYT4-Ni	49.9	19.2	09.0	02.2	00.0	00.0
NYT10-Ni	49.9	22.1	09.9	02.6	00.3	00.0

Table 4.3: Degradation of MB using post modified HY catalysts under irradiation UV light.

Catalyst	Time in minutes					
	0	30	60	120	180	240
HYT1-Ag	49.9	12.8	05.8	00.0	00.0	00.0
HYT2-Ag	49.9	14.1	06.1	01.0	00.0	00.0
HYT4-Ag	49.9	14.4	06.1	01.3	00.0	00.0
HYT10-Ag	49.9	14.7	09.0	01.9	00.3	00.0
HYT1-Co	49.9	8.6	02.9	00.6	00.0	00.0
HYT2-Co	49.9	10.6	03.8	01.0	00.3	00.0
HYT4-Co	49.9	11.5	05.4	02.2	00.3	00.0
HYT10-Co	49.9	11.8	05.1	02.2	00.6	00.0
HYT1-Cu	49.9	10.9	02.6	00.6	00.0	00.0
HYT2-Cu	49.9	11.5	03.8	00.6	00.0	00.0
HYT4-Cu	49.9	13.4	05.8	01.6	00.0	00.0
HYT10-Cu	49.9	16.3	08.3	02.2	00.0	00.0
HYT1-Fe	49.9	10.9	07.4	02.9	00.0	00.0
HYT2-Fe	49.9	14.7	08.3	04.2	00.3	00.0
HYT4-Fe	49.9	19.2	10.9	05.8	00.3	00.0
HYT10-Fe	49.9	19.7	11.1	05.8	00.6	00.0
HYT1-Ni	49.9	13.1	04.8	01.6	00.0	00.0
HYT2-Ni	49.9	13.4	05.8	2.2	01.3	00.0
HYT4-Ni	49.9	13.8	07.0	02.9	01.6	00.0
HYT10-Ni	49.9	14.7	08.6	02.9	00.3	00.0

Table 4.4: Decrease in COD of MB using post modified NaY catalysts.

Catalysts	Time in minutes					
	0	30	60	120	180	240
NYT1-Ag	62	19	07	00	00	00
NYT2-Ag	62	23	13	07	00	00
NYT4-Ag	62	28	19	09	00	00
NYT10-Ag	62	32	21	11	00	00
NYT1-Co	62	20	11	07	00	00
NYT2-Co	62	24	14	08	00	00
NYT4-Co	62	24	15	09	00	00
NYT10-Co	62	27	15	09	00	00
NYT1-Cu	62	26	16	08	00	00
NYT2-Cu	62	28	16	08	00	00
NYT4-Cu	62	31	18	09	00	00
NYT10-Cu	62	31	19	09	00	00
NYT1-Fe	62	26	14	08	00	00
NYT2-Fe	62	24	16	08	00	00
NYT4-Fe	62	26	16	08	00	00
NYT10-Fe	62	27	15	09	00	00
NYT1-Ni	62	26	14	08	00	00
NYT2-Ni	62	27	16	08	00	00
NYT4-Ni	62	27	16	08	00	00
NYT10-Ni	62	31	17	08	00	00

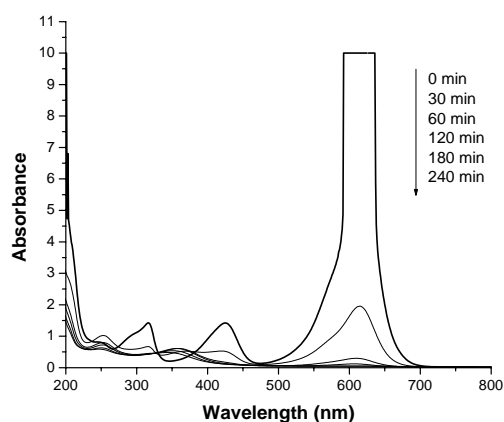
Table 4.5: Decrease in COD of MB using post modified HY catalysts.

Catalysts	Time in minutes					
	0	30	60	120	180	240
HYT1-Ag	62	20	12	07	00	00
HYT2-Ag	62	22	12	07	00	00
HYT4-Ag	62	22	12	07	00	00
HYT10-Ag	62	22	16	08	00	00
HYT1-Co	62	15	09	06	00	00
HYT2-Co	62	18	10	07	00	00
HYT4-Co	62	19	12	08	00	00
HYT10-Co	62	19	11	08	00	00
HYT1-Cu	62	18	8	06	00	00
HYT2-Cu	62	19	10	06	00	00
HYT4-Cu	62	21	12	07	00	00
HYT10-Cu	62	24	15	08	00	00
HYT1-Fe	62	18	14	09	00	00
HYT2-Fe	62	22	15	10	00	00
HYT4-Fe	62	27	18	12	00	00
HYT10-Fe	62	28	18	12	00	00
HYT1-Ni	62	20	11	07	00	00
HYT2-Ni	62	21	12	08	00	00
HYT4-Ni	62	21	13	09	00	00
HYT10-Ni	62	22	15	09	00	00

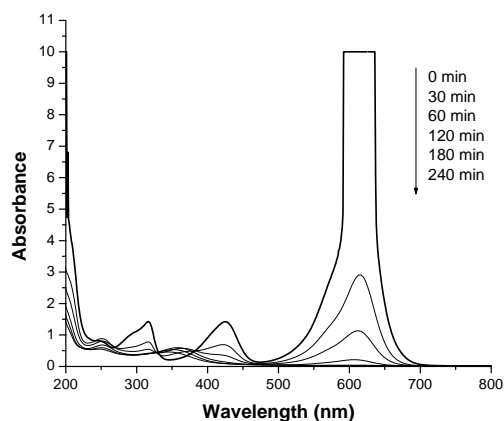
The complete degradation of MB took place using post modified TiO₂ encapsulated catalysts as evidenced from the zero COD value from Tables 4.4 and 4.5

4.4.2. Degradation of MG

The UV-Vis spectrum of degradation of MG with respect to time using post modified catalysts was nearly same as compared to TiO_2 encapsulated zeolites as shown in Figure 4.6. Tables 4.6 and 4.7 show the decrease in concentration of MB under irradiation of UV light using different post modified NaY and HY catalyst, respectively. The decrease in COD of MG using different post modified NaY and HY catalyst are shown in Tables 4.8 and 4.9.



(a) UV-Vis absorption spectra of degradation of MG using NYT1-Ag



(b) UV-Vis absorption spectra of degradation of MG using HYT1-Ag

Figure 4.6: UV-Vis absorption spectra of degradation of MG using a) NYT1-Ag & b) HYT1-Ag.

Table 4.6: Degradation of MG using post modified NaY catalysts under irradiation of UV light.

Catalysts	Time in minutes					
	0	30	60	120	180	240
NYT1-Ag	51.9	17.6	09.3	00.9	00.0	00.0
NYT2-Ag	51.9	14.8	05.6	01.9	00.0	00.0
NYT4-Ag	51.9	21.3	09.3	04.6	02.8	00.0
NYT10-Ag	51.9	15.8	06.5	01.9	00.0	00.0
NYT1-Co	51.9	13.9	03.7	01.9	00.9	00.0
NYT2-Co	51.9	10.2	03.7	00.9	00.6	00.0
NYT4-Co	51.9	13.9	05.6	02.4	00.9	00.0
NYT10-Co	51.9	14.2	06.5	03.9	01.5	00.0
NYT1- Cu	51.9	8.7	03.9	01.0	00.6	00.0
NYT2- Cu	51.9	10.2	05.6	02.6	00.0	00.0
NYT4- Cu	51.9	11.1	04.6	00.9	00.0	00.0
NYT10-Cu	51.9	11.9	07.0	01.6	00.0	00.0
NYT1-Fe	51.9	14.8	05.6	01.9	00.0	00.0
NYT2-Fe	51.9	15.8	05.6	01.9	00.0	00.0
NYT4-Fe	51.9	15.7	07.4	02.8	00.9	00.0
NYT10-Fe	51.9	16.7	08.3	03.7	00.9	00.0
NYT1-Ni	51.9	14.8	05.6	01.9	00.0	00.0
NYT2- Ni	51.9	17.6	05.6	00.9	00.0	00.0
NYT4- Ni	51.9	15.8	06.5	01.9	00.0	00.0
NYT10- Ni	51.9	17.6	06.5	01.9	00.0	00.0

Table 4.7: Degradation of MG using post modified HY catalysts under irradiation of UV light.

Catalysts	Time in minutes					
	0	30	60	120	180	240
HYT1-Ag	51.9	08.3	04.6	01.9	00.0	00.0
HYT2-Ag	51.9	11.1	05.6	02.8	00.5	00.0
HYT4-Ag	51.9	11.1	05.6	03.7	01.9	00.0
HYT10-Ag	51.9	14.1	07.0	05.6	02.1	00.0
HYT1-Co	51.9	11.6	02.4	00.7	00.1	00.0
HYT2-Co	51.9	13.0	04.3	01.9	00.0	00.0
HYT4-Co	51.9	15.8	08.3	02.8	00.9	00.0
HYT10-Co	51.9	15.8	08.2	03.7	01.9	00.0
HYT1- Cu	51.9	09.3	02.0	00.9	00.0	00.0
HYT2- Cu	51.9	10.2	02.8	00.9	00.0	00.0
HYT4- Cu	51.9	11.6	05.6	01.9	00.5	00.0
HYT10-Cu	51.9	13.0	08.5	03.7	00.9	00.0
HYT1-Fe	51.9	21.3	10.6	03.7	00.9	00.0
HYT2-Fe	51.9	20.9	10.9	03.7	00.9	00.0
HYT4-Fe	51.9	20.4	10.2	03.7	00.9	00.0
HYT10-Fe	51.9	16.7	09.3	03.7	00.9	00.0
HYT1-Ni	51.9	14.8	03.7	01.9	00.0	00.0
HYT2-Ni	51.9	13.9	05.6	01.9	00.0	00.0
HYT4-Ni	51.9	17.6	07.4	01.9	00.0	00.0
HYT10-Ni	51.9	18.6	08.3	02.8	00.0	00.0

Table 4.8: Decrease in COD of MG using post modified NaY catalysts.

Catalysts	Time in minutes					
	0	30	60	120	180	240
NYT1-Ag	74	30	20	09	00	00
NYT2-Ag	74	27	15	10	00	00
NYT4-Ag	74	35	20	14	12	00
NYT10-Ag	74	28	16	10	00	00
NYT1-Co	74	26	13	10	00	00
NYT2-Co	74	21	13	09	00	00
NYT4-Co	74	26	15	11	00	00
NYT10-Co	74	26	16	13	10	00
NYT1-Cu	74	19	13	09	00	00
NYT2-Cu	74	21	15	11	00	00
NYT4-Cu	74	22	14	09	00	00
NYT10-Cu	74	23	17	10	00	00
NYT1-Fe	74	27	15	10	00	00
NYT2-Fe	74	28	15	10	00	00
NYT4-Fe	74	28	17	12	09	00
NYT10-Fe	74	29	19	13	09	00
NYT1-Ni	74	27	15	10	00	00
NYT2-Ni	74	30	15	09	00	00
NYT4-Ni	74	28	16	10	00	00
NYT10-Ni	74	30	16	10	00	00

Table 4.9: Decrease in COD of MG using post modified HY catalysts.

Catalyst	Time in minutes					
	0	30	60	120	180	240
HYT1-Ag	74	19	14	10	00	00
HYT2-Ag	74	22	15	12	09	00
HYT4-Ag	74	22	15	13	10	00
HYT10-Ag	74	26	17	15	11	00
HYT1-Co	74	23	11	9	00	00
HYT2-Co	74	25	13	10	00	00
HYT4-Co	74	28	19	12	09	00
HYT10-Co	74	28	18	13	10	00
HYT1-Cu	74	20	11	9	00	00
HYT2-Cu	74	21	12	9	00	00
HYT4-Cu	74	23	15	10	09	00
HYT10-Cu	74	25	19	13	09	00
HYT1-Fe	74	35	22	13	09	00
HYT2-Fe	74	35	22	13	09	00
HYT4-Fe	74	34	21	13	09	00
HYT10-Fe	74	29	20	13	09	00
HYT1-Ni	74	27	13	10	00	00
HYT2- Ni	74	26	15	10	00	00
HYT4-Ni	74	30	17	10	00	00
HYT10-Ni	74	32	19	12	00	00

There was decrease in concentration of MG upon irradiation of UV light using different post modified NaY and HY catalyst as evident from Tables 4.6 and 4.7, respectively. The enhanced photoactivity was obtained in silver ion exchange catalyst

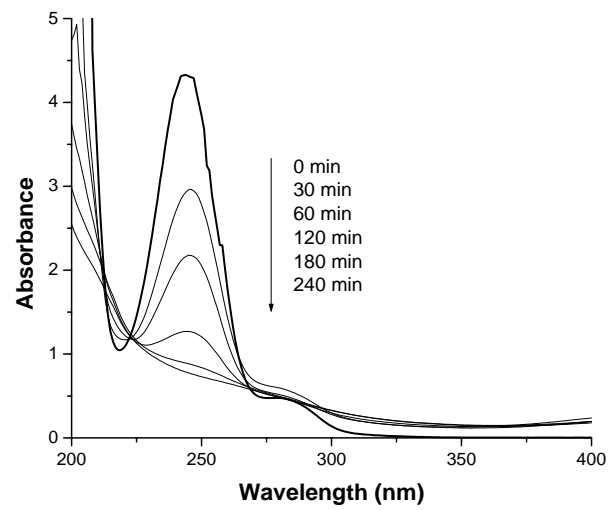
as compared to other metal ion exchanged catalyst in case of both the dyes MB and MG. The complete degradation of MG took place using post modified TiO₂ encapsulated catalysts as evidenced from the zero COD value from Tables 4.8 & 4.9

4.5. Photocatalytic Degradation of Organic Compounds

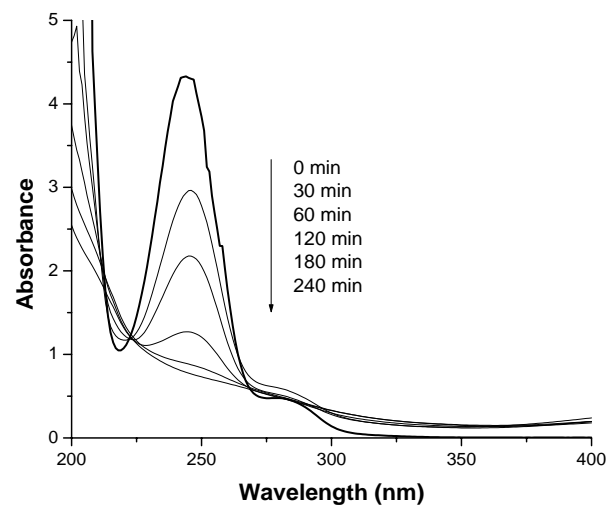
The photocatalytic degradation of AP and NB was carried out using post modified TiO₂ encapsulated catalysts. The adsorption on the surface of catalysts before irradiation was determined by spectrophotometer was nearly same as compare to the TiO₂ encapsulated catalysts, it was 8-11 % for AP and 21-26% for NB in case of post modified TiO₂ encapsulated in NaY zeolite, while it was 10-13% for AP and 20-22% for NB in post modified TiO₂ encapsulated HY catalysts.

4.5.1. Degradation of AP

The UV-Vis absorption spectrum of degradation of AP with respect to time using post modified catalysts was nearly same as compare TiO₂ encapsulated zeolites as shown in Figures 4.7. Tables 4.10 and 4.11 show the decrease in concentration of AP under irradiation of UV light using different post modified NaY and HY catalyst, respectively. The decrease in COD of AP using different post modified NaY and HY catalyst are shown in Tables 4.12 and 4.13.



(a) UV-Vis absorption spectra of degradation of AP using NYT1-Ag



(b) UV-Vis absorption spectra of degradation of AP using HYT1-Ag

Figure 4.7: UV-Vis absorption spectra of degradation of AP post modified catalysts
(a) NYT1-Ag (b) HYT1-Ag.

Table 4.10: Degradation of AP using post modified NaY catalysts under irradiation of UV light.

Catalysts	Time in minutes					
	0	30	60	120	180	240
NYT1-Ag	50.6	19.9	11.4	08.5	06.5	03.4
NYT2-Ag	50.6	23.4	13.1	10.3	07.2	06.1
NYT4-Ag	50.6	20.4	12.6	08.8	06.6	03.7
NYT10-Ag	50.6	20.9	12.7	08.9	06.7	03.7
NYT1-Co	50.6	22.4	11.7	09.0	08.1	04.9
NYT2-Co	50.6	23.3	12.0	09.1	07.6	04.9
NYT4-Co	50.6	31.7	16.8	12.3	10.5	07.7
NYT10-Co	50.6	24.5	12.3	09.4	08.1	05.2
NYT1-Cu	50.6	30.6	18.0	12.0	09.7	07.5
NYT2- Cu	50.6	30.6	16.6	12.1	10.1	07.6
NYT4-Cu	50.6	31.7	16.8	12.3	10.5	07.7
NYT10-Cu	50.6	32.8	16.2	12.7	10.6	08.5
NYT1-Fe	50.6	25.4	18.2	15.8	12.2	11.3
NYT2-Fe	50.6	24.5	16.6	14.9	11.9	10.2
NYT4-Fe	50.6	24.6	17.3	15.6	13.8	12.7
NYT10-Fe	50.6	24.9	15.6	14.2	12.9	12.0
NYT1-Ni	50.6	23.4	13.1	10.3	07.2	06.1
NYT2-Ni	50.6	23.0	12.7	09.3	07.5	06.4
NYT4-Ni	50.6	20.4	12.6	08.8	06.6	03.7
NYT10-Ni	50.6	20.9	14.7	12.7	08.9	06.7

Table 4.11: Degradation of AP using post modified HY catalysts under irradiation of UV light.

Catalysts	Time in minutes					
	0	30	60	120	180	240
HYT1-Ag	50.6	13.8	07.5	04.6	02.3	01.9
HYT2-Ag	50.6	15.9	10.3	07.8	04.8	2.5
HYT4-Ag	50.6	19.6	10.7	08.4	06.5	04.7
HYT10-Ag	50.6	19.9	12.4	08.7	06.5	05.3
HYT1-Co	50.6	19.6	08.9	07.1	04.3	03.6
HYT2-Co	50.6	22.5	09.6	06.5	06.0	04.3
HYT4-Co	50.6	27.8	14.7	10.5	07.7	05.2
HYT10-Co	50.6	25.1	13.2	09.6	07.6	04.7
HYT1- Cu	50.6	25.5	13.1	10.3	07.6	05.0
HYT2-Cu	50.6	26.4	13.9	10.5	07.7	05.2
HYT4-Cu	50.6	27.8	14.7	10.5	07.7	05.2
HYT10-Cu	50.6	31.5	15.6	11.8	10.2	08.4
HYT1-Fe	50.6	25.7	16.5	12.7	09.4	06.8
HYT2-Fe	50.6	23.3	13.9	10.7	08.2	05.5
HYT4-Fe	50.6	25.5	16.7	12.9	09.9	06.2
HYT10-Fe	50.6	28.4	16.9	13.8	10.6	07.8
HYT1-Ni	50.6	20.5	07.2	04.3	02.0	01.9
HYT2-Ni	50.6	19.9	06.5	04.0	01.9	01.7
HYT4-Ni	50.6	23.3	13.2	10.0	07.3	06.0
HYT10-Ni	50.6	24.3	13.6	10.1	07.3	06.1

Table 4.12: Decrease in COD of AP using post modified NaY catalysts.

Catalysts	Time in minutes					
	0	30	60	120	180	240
NYT1-Ag	121	54	36	30	26	19
NYT2-Ag	121	62	40	34	27	25
NYT4-Ag	121	55	39	31	26	20
NYT10-Ag	121	57	39	31	26	20
NYT1-Co	121	60	37	31	29	22
NYT2-Co	121	62	38	31	28	22
NYT4-Co	121	80	48	38	34	28
NYT10-Co	121	64	38	32	29	23
NYT1-Cu	121	77	50	38	33	28
NYT2-Cu	121	77	47	38	34	28
NYT4-Cu	121	80	48	38	34	28
NYT10-Cu	121	82	47	39	35	30
NYT1-Fe	121	66	51	46	38	36
NYT2-Fe	121	64	47	44	37	34
NYT4-Fe	121	64	49	45	41	39
NYT10-Fe	121	65	45	42	40	38
NYT1-Ni	121	62	40	34	27	25
NYT2-Ni	121	61	39	32	28	26
NYT4-Ni	121	55	39	31	26	20
NYT10-Ni	121	57	43	39	31	26

Table 4.13: Decrease in COD of AP using post modified HY catalysts.

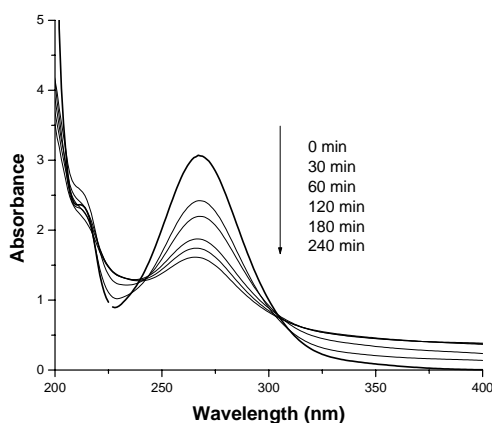
Catalysts	Time in minutes					
	0	30	60	120	180	240
HYT1-Ag	121	041	028	022	017	016
HYT2-Ag	121	046	034	029	022	017
HYT4-Ag	121	054	035	030	026	022
HYT10-Ag	121	054	038	031	026	023
HYT1-Co	121	054	031	027	021	020
HYT2-Co	121	060	032	026	025	021
HYT4-Co	121	071	043	034	028	023
HYT10-Co	121	066	040	032	028	022
HYT1-Cu	121	066	040	034	028	023
HYT2- Cu	121	068	042	034	028	023
HYT4-Cu	121	071	043	034	028	023
HYT10-Cu	121	079	045	037	034	030
HYT1-Fe	121	067	047	039	032	026
HYT2-Fe	121	062	042	035	029	024
HYT4-Fe	121	066	048	040	033	025
HYT10-Fe	121	073	048	041	035	029
HYT1-Ni	121	056	027	021	016	016
HYT2-Ni	121	054	026	021	016	016
HYT4-Ni	121	062	040	033	028	025
HYT10-Ni	121	064	041	034	028	025

Tables 4.10 and 4.11 show the degradation of AP and it reaches nearly 100% in case of post modified catalysts exchanged with silver. The degradation of AP was increased in post modified HY catalysts as compared to post modified NaY catalysts.

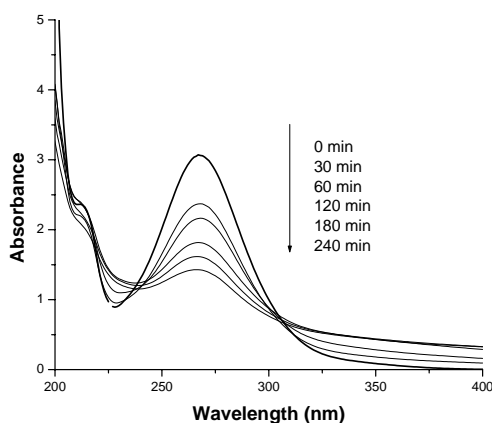
Tables 4.12 and 4.13 show the decrease in COD of the AP and it is reduced from 121 to 6 mgL⁻¹.

4.5.2. Degradation of NB

The UV-Vis absorption spectrum of degradation of NB with respect to time using post modified catalysts was nearly same as compared with TiO₂ encapsulated zeolites as shown in Figure 4.8. Tables 4.14 and 4.15 show the decrease in concentration of NB under irradiation of UV light using different post modified NaY and HY catalyst, respectively. The decrease in COD of NB using different post modified NaY and HY catalyst are shown in Tables 4.16 and 4.17.



(a) UV-Vis absorption spectrum of degradation of NB using NYT2-Ag



(b) UV-Vis absorption spectrum of degradation of NB using HYT2-Ag

Figure 4.8: UV-Vis absorption spectra of degradation of NB post modified catalysts
(a) NYT1-Ag (b) HYT1-Ag.

Table 4.14: Degradation of NB using post modified NaY catalysts under irradiation of UV light.

Catalyst	Time in minutes					
	0	30	60	120	180	240
NYT1-Ag	51.5	31.1	28.3	26.0	24.1	22.3
NYT2-Ag	51.5	31.1	28.2	25.7	23.3	20.1
NYT4-Ag	51.5	31.1	27.9	26.0	23.4	20.4
NYT10-Ag	51.5	32.3	29.7	25.5	21.8	19.0
NYT1-Co	51.5	42.1	38.7	33.4	29.2	24.1
NYT2-Co	51.5	39.4	35.2	31.9	27.2	22.3
NYT4-Co	51.5	39.9	36.9	34.1	30.3	26.2
NYT10-Co	51.5	43.1	40.0	35.8	31.1	26.0
NYT1-Cu	51.5	41.9	38.8	35.6	32.1	30.8
NYT2-Cu	51.5	40.1	37.6	33.6	30.2	27.2
NYT4-Cu	51.5	39.4	36.0	32.5	26.6	22.3
NYT10-Cu	51.5	42.0	39.0	35.6	31.5	28.3
NYT1-Fe	51.5	39.5	36.0	32.0	26.5	24.1
NYT2-Fe	51.5	41.0	37.6	33.5	29.4	26.2
NYT4-Fe	51.5	43.1	40.1	33.7	30.5	27.5
NYT10-Fe	51.5	42.1	39.5	36.0	32.8	30.8
NYT1-Ni	51.5	37.3	34.0	29.7	25.4	22.0
NYT2-Ni	51.5	37.3	32.3	27.9	23.9	20.2
NYT4-Ni	51.5	36.2	33.1	27.7	22.2	19.2
NYT10-Ni	51.5	36.2	32.5	27.1	20.7	18.1

Table 4.15: Degradation of NB using post modified HY catalysts under irradiation of UV light.

Catalyst	Time in minutes					
	0	30	60	120	180	240
HYT1-Ag	51.5	30.2	26.8	22.9	18.7	14.2
HYT2-Ag	51.5	28.3	24.7	21.8	18.1	12.8
HYT4-Ag	51.5	26.6	22.3	18.1	13.1	10.8
HYT10-Ag	51.5	27.7	24.0	19.7	17.5	13.9
HYT1-Co	51.5	38.4	35.2	30.3	25.1	21.1
HYT2-Co	51.5	32.1	28.7	24.1	20.9	17.4
HYT4-Co	51.5	37.6	34.4	29.7	25.6	22.0
HYT10-Co	51.5	27.7	24.0	19.7	17.5	13.9
HYT1- Cu	51.5	37.6	35.2	32.5	28.4	24.1
HYT2- Cu	51.5	35.3	32.1	28.3	24.1	21.1
HYT4- Cu	51.5	40.1	37.1	33.7	29.7	26.7
HYT10-Cu	51.5	43.2	40.1	36.9	32.4	28.8
HYT1-Fe	51.5	38.5	35.2	31.6	28.2	25.2
HYT2-Fe	51.5	38.2	34.4	30.5	26.8	22.7
HYT4-Fe	51.5	39.0	36.8	32.3	28.3	24.1
HYT10-Fe	51.5	41.2	38.3	34.1	29.7	24.7
HYT1-Ni	51.5	34.6	31.5	27.6	24.3	20.7
HYT2- Ni	51.5	33.7	31.0	27.0	22.8	20.4
HYT4- Ni	51.5	33.6	29.4	25.9	22.7	20.6
HYT10- Ni	51.5	31.9	29.1	25.5	20.4	17.0

Table 4.16: Decrease in COD of NB using post modified NaY catalysts.

Catalyst	Time in minutes					
	0	30	60	120	180	240
NYT1-Ag	93	54	49	45	41	38
NYT2-Ag	93	54	49	44	40	33
NYT4-Ag	93	54	48	45	40	34
NYT10-Ag	93	57	52	44	37	31
NYT1-Co	93	76	69	59	51	41
NYT2-Co	93	70	62	56	47	38
NYT4-Co	93	71	66	60	53	45
NYT10-Co	93	77	71	63	54	45
NYT1-Cu	93	75	69	63	56	54
NYT2-Cu	93	72	67	59	53	47
NYT4-Cu	93	70	64	57	46	38
NYT10-Cu	93	75	70	63	55	49
NYT1-Fe	93	71	64	56	46	41
NYT2-Fe	93	73	67	59	51	45
NYT4-Fe	93	77	72	59	53	48
NYT10-Fe	93	76	71	64	58	54
NYT1-Ni	93	66	60	52	44	37
NYT2-Ni	93	66	57	48	41	34
NYT4-Ni	93	64	58	48	37	32
NYT10-Ni	93	64	57	47	35	30

Table 4.17: Decrease in COD of NB using HY post modified catalysts.

Catalysts	Time in minutes					
	0	30	60	120	180	240
HYT1-Ag	93	53	46	39	31	22
HYT2-Ag	93	49	42	37	30	19
HYT4-Ag	93	46	38	30	20	16
HYT10-Ag	93	48	41	33	28	22
HYT1-Co	93	68	62	53	43	35
HYT2-Co	93	56	50	41	35	28
HYT4-Co	93	67	61	52	44	37
HYT10-Co	93	48	41	33	28	22
HYT1-Cu	93	67	62	57	49	41
HYT2- Cu	93	63	56	49	41	35
HYT4-Cu	93	72	66	59	52	46
HYT10-Cu	93	78	72	66	57	50
HYT1-Fe	93	69	62	55	49	43
HYT2-Fe	93	68	61	53	46	38
HYT4-Fe	93	70	65	57	49	41
HYT10-Fe	93	74	68	60	52	42
HYT1-Ni	93	61	55	48	41	35
HYT2-Ni	93	59	54	47	39	34
HYT4-Ni	93	59	51	45	38	34
HYT10-Ni	93	56	51	44	34	28

Tables 4.14 and 4.15 show the degradation of NB and it reaches nearly 27% in case of post modified HY catalysts exchanged with silver. The degradation of NB was increased in post modified HY catalysts as compared to post modified NaY catalysts.

As compared to AP the degradation of NB was found slow in all post modified catalysts. Tables 4.16 and 4.17 show the decrease in COD of the NB and it is reduced from 92 to 22 mgL⁻¹.

4.6. Results and Discussion

As discussed above, degradation of dyes and organic compounds was studied using bare zeolites. The results state that there was no substantial degradation of dyes and organic compounds (Chapter 3).

The initial rate of the degradation of dyes and organic compounds by TiO₂ encapsulated NaY and HY zeolites, before metal ion exchange is listed in Table 4.18.

Table 4.18: Initial rate of degradation using TiO₂ encapsulated NaY and HY catalyst.

Catalyst	Initial rate of degradation of substrates ($\times 10^6$ M/min)			
	MB	MG	AP	NB
NaYT1	03.14	01.22	07.44	05.68
NaYT2	03.55	01.51	08.55	06.25
NaYT4	03.05	01.37	08.01	04.12
NaYT10	03.05	01.37	07.00	03.94
HYT1	03.57	01.42	03.59	03.59
HYT2	04.39	01.53	10.00	04.93
HYT4	03.95	01.41	08.17	04.15
HYT10	03.67	01.22	06.31	03.67

The metal ion exchange was carried out by aqueous metal ion exchanged method. The Ag, Cu, Co, Fe, and Ni metals were used for the metal ion exchange. After metal ion exchange the structure of zeolite remained the same. This was determined from the XRD pattern of the metal ion exchanged zeolites where no additional peak was observed. This established that there was no perturbation in the structure of the

zeolites. In the following sections, the degradation of MB, MG AP and NB by catalysts after ion exchange is discussed.

4.6.1. Silver ion exchange

The initial rate of degradation of MB, MG, AP and NB increased upon silver exchange of TiO₂ encapsulated NaY and HY catalysts as compared to TiO₂ encapsulated catalysts. This is evident from the figures tabulated in Table 4.19 for silver exchange TiO₂ encapsulated NaY and HY catalysts when compared with figures for TiO₂ encapsulated NaY and HY catalysts tabulated in Table 4.18.

The above enhancements in photocatalytic activity can be attributed to the reason that silver ion was completely exchanged on NYT and HYT catalysts. The silver ion may be located in the positions SI, SI', SII, SII' of the supercage [46]. The reduction of Ag causes the zeolitic acid sites to be generated which may be helpful for the enhancement in the initial rate of degradation of MB, MG, AP, and NB and subsequent photodegradation with time.

Table 4.19: Initial rate of degradation using post modified catalyst with silver exchange.

Catalyst	Initial rate of degradation of substrates ($\times 10^{-6}$ M/min)			
	MB	MG	AP	NB
NaY-T1-Ag	04.0	01.5	09.0	06.8
NaY-T2-Ag	04.9	03.9	09.2	07.0
NaY-T4-Ag	03.9	02.0	08.6	06.8
NaY -T10-Ag	03.4	01.1	08.3	06.5
HY-T1-Ag	05.0	01.8	08.0	07.0
HY-T2-Ag	05.0	02.0	12.0	08.0
HY-T4-Ag	05.0	02.0	10.0	08.0
HY-T10-Ag	04.4	01.7	10.0	08.1

4.6.2. Cobalt ion exchange

The tables 4.18 and 4.20 show that initial rate of degradation for both dyes has increased for cobalt ion exchanged catalysts. While in case of nitrobenzene, the initial rate of degradation reduced.

The cobalt ion exchange catalyst has displayed an increased photocatalytic activity for all substrates as compared to TiO₂ encapsulated zeolite catalyst except NB where it got reduced. This showed that Co is selective, in general, for the degradation of organic compounds and dyes. The cobalt ions after ion exchange are located in sodalite cages and double six rings (D6R) framework.

Table 4.20: Initial rate of degradation using post modified catalyst with cobalt exchange

Catalyst	Initial rate of degradation of substrates ($\times 10^6$ M/min)			
	MB	MG	AP	NB
NaY-T1-Co	4.8	2.0	8.0	2.0
NaY-T2-Co	4.0	2.0	8.0	2.0
NaY-T4-Co	4.0	1.6	8.0	4.0
NaY-T10-Co	3.6	1.6	2.7	2.7
HY-T1-Co	5.3	1.8	9.5	4.1
HY-T2-Co	5.0	1.7	8.8	4.8
HY-T4-Co	4.8	1.6	7.0	4.6
HY-T10-Co	4.8	1.6	8.0	2.7

4.6.3. Copper ion exchange

The initial rate of degradation of MB, MG, AP and NB using Cu exchanged TiO₂ encapsulated catalysts are tabulated in Table 4.21. The initial rate of degradation of dyes using Cu metal ion exchange in NaY and HY catalysts increased. It reduced in case of both AP and NB as compared to the TiO₂ encapsulated in NaY zeolite. With HY, it increased for NB and it decreased for AP. Thus, it can be concluded that on an

average the degradation is favoured with Cu exchanged catalysts. After copper ion exchange, the copper cations were located in SI or SI', SII' and SII sites [47]. The copper ion, with hydrogen generates bronsted acid sites in NaY and HY. This may cause the change in the initial rate of degradation, as was observed in all the TiO₂ encapsulated NaY and HY catalysts in the present work.

Table 4.21: Initial rate of degradation using post modified catalyst with copper exchange.

Catalyst	Initial rate of degradation of substrates ($\times 10^{-6}$ M/min)			
	MB	MG	AP	NB
NaY-T1-Cu	4.0	2.0	6.0	3.0
NaY-T2-Cu	4.0	2.0	4.0	4.0
NaY-T4-Cu	3.0	2.0	5.0	3.0
NaY-T10-Cu	3.3	1.6	4.8	1.1
HY-T1-Cu	5.0	1.9	8.0	5.0
HY-T2-Cu	4.7	1.8	7.4	5.6
HY-T4-Cu	5.0	1.8	7.0	4.0
HY-T10-Cu	4.2	1.7	5.2	2.6

4.6.4. Iron ion exchange

In Fe ion exchanged catalysts, the initial rate of degradation of MB, MG and AP increased but it decreased in case of NB as compared to TiO₂ encapsulated NaY and HY catalysts. The enhancement was higher in TiO₂ encapsulated HY catalyst than NaY catalyst. After ion exchange iron cations were located at SI', SII' and /or II positions. The initial rates of degradation are tabulated in Table 4.22.

Table 4.22: Initial rate of degradation using post modified catalyst with iron exchange

Catalyst	Initial rate of degradation of substrates ($\times 10^{-6}$ M/min)			
	MB	MG	AP	NB
NaY-T1-Fe	4.0	2.0	8.0	4.0
NaY-T2-Fe	4.0	1.5	8.0	3.0
NaY-T4-Fe	3.8	1.6	7.8	2.8
NaY-T10-Fe	3.6	1.5	7.7	2.8
HY-T1-Fe	5.2	1.3	7.6	4.3
HY-T2-Fe	4.5	1.3	8.4	4.4
HY-T4-Fe	3.9	1.4	7.8	4.1
HY-T10-Fe	3.7	1.5	6.7	3.3

4.6.5. Nickel ion exchange

Nickel ion exchanged catalyst in NaY showed an enhancement in the initial rate of degradation in case of MB, MG and AP except NB where it got reduced as compared to TiO₂ encapsulated NaY catalysts. In HY with nickel ion exchanged catalyst, the initial rate of degradation of MB, MG, AP and NB increased as compared to TiO₂ encapsulated HY catalyst. The nickel ions also located in SI, SI' and SII or SII'. The initial rates of degradation are tabulated in Table 4.23.

Table 4.23: Initial rate of degradation using post modified catalyst with nickel exchange

Catalyst	Initial rate of degradation of substrates ($\times 10^{-6}$ M/min)			
	MB	MG	AP	NB
NaY-T1-Ni	4.0	2.0	8.0	4.0
NaY-T2-Ni	4.0	1.4	8.5	4.5
NaY-T4-Ni	4.0	1.5	8.2	4.8
NaY-T10-Ni	3.4	1.4	8.3	4.9
HY-T1-Ni	4.6	1.6	9.1	5.6
HY-T2-Ni	4.6	1.6	9.5	6.1
HY-T4-Ni	4.5	1.5	8.5	6.1
HY-T10-Ni	4.4	1.4	8.0	6.7

From all above results of metal ion exchanged catalysts, it can be concluded that the initial rate of degradation of MB, MG, AP and NB are the highest in silver ion exchanged catalyst amongst all metal ion exchanged zeolite encapsulated TiO₂ catalysts. It was understood that the some metal ions can effectively enhance the photocatalytic activity of the TiO₂ encapsulated catalysts. This may be because of their position in the framework and the increase in acidity of the zeolite. It can be further concluded that the enhancement in HY zeolite ion exchanged catalysts was higher than the NaY ion exchanged catalyst for degradation of all the dyes and organic compounds. The degradation of NB was found to reduce in all metal ions exchanged catalysts except silver exchanged catalysts. The possible reason may be because of the complete replacement of all Na and H in the 6R of the zeolite.

Thus, it can be concluded that the cation exchange in TiO₂ encapsulated zeolite catalysts enhances the photocatalytic degradation of dyes and organic compounds and can be a better candidate for the selective degradation of pollutants in wastewaters. In particular, silver ion exchanged catalyst has the most favoured photocatalytic degradation characteristics among other metal ions exchanged catalysts as was evident from the present experimental findings.

4.7. References

- [1] A. Corma, *Chem. Rev.* 97 (1997) 2373, and references therein.
- [2] G. Centi, B. Wichterlova, A.T. Bell (Eds.), *Catalysis by Unique Metal Ion Structures in Solid Matrices*, NATO Science Series, vol. 13, 2001, and references therein.
- [3] A. Notari, *Adv. Catal.* 41 (1996) 253, and references therein.
- [4] N. J. Turro, X.G. Lei, S. Jockusch, W. Li, Z.Q. Liu, L. Abrams, M.F. Ottaviani, *J. Org. Chem.* 67 (2002) 2606.
- [5] J. Shailaja, J. Sivaguru, S. Uppili, A. Joy, V. Ramamurthy, *Microporous Mesoporous Mater.* 48 (2001) 319.
- [6] M. Anpo (Ed.), *Photofunctional Zeolites*, NOVA Publishers Inc., 2000, and references therein.
- [7] H. Nishiguchi, M. Anpo, *J. Photochem. Photobiol. A: Chemistry* 77 (1994) 183.
- [8] M. Anpo (Ed.), *Surface Photochemistry*, Wiley, New York, 1996, and references therein.
- [9] D. Barthomeuf, *Catal. Rev.* 38 (1996) 521.
- [10] J. Engelhardt, J. Szani, J. Valyon, *J. Catal.* 107 (1987) 29.
- [11] A. Corma, *Mater. Res. Soc. Symp. Proc.* 233 (1991) 17.
- [12] W. F. Heolderich, M.Hesse, F. Naeumann, *Angew. Chem.* 27 (1988) 226.
- [13] M. Anpo, S. Dohshi, M. Takeuchi, K. Ikeue, *Curr. Opin. Solid State Mater. Sci.* 6 (2002), in press.
- [14] H. Yamashita, Y. Ichihashi, M. Anpo, M. Hashimoto, C. Louis, M. Che, *J. Phys. Chem.* 100 (1996) 16041.
- [15] H. Yamashita, Y. Ichihashi, S.G. Zhang, Y. Matsumura, Y. Souma, T. Tatsumi, M. Anpo, *Appl. Surf. Sci.* 121 (1997) 305.
- [16] J. L. Zhang, Y. Hu, M. Matsuoka, H. Yamashita, M. Minagawa, H. Hidaka, M. Anpo, *J. Phys. Chem. B*, 105 (2001) 8395.
- [17] S. Higashimoto, M. Matsuoka, S.G. Zhang, H. Yamashita, O. Kitao, H. Hidaka, M. Anpo, *Microporous Mesoporous Mater.* 48 (2001) 329.
- [18] M. Anpo, S. G. Zhang, H. Mishima, M. Matsuoka, H. Yamashita, *Catal. Today* 39 (1997) 159.
- [19] S. Higashimoto, K. Nishimoto, T. Ono, M. Anpo, *Chem. Lett.*, (2000) 1160.
- [20] W. S. Ju, M. Matsuoka, M. Anpo, *Catal. Lett.*, 71 (2001) 91.
- [21] H. Yamashita, S. Kawasaki, Y. Ichihashi, M. Harada, M. Takeuchi, M. Anpo, G. Stewart, M.A. Fox, C. Louis, M. Che, *J. Phys. Chem. B*, 102 (1998) 5870.
- [22] H. Yamashita, M. Honda, M. Harada, Y. Ichihashi, M. Anpo, T. Hirao, N. Itoh, N. Iwamoto, *J. Phys. Chem. B*, 102 (1998) 10707.
- [23] H. Yamashita, Y. Ichihashi, M. Harada, G. Stewart, M.A. Fox, M. Anpo, *J. Catal.* 158 (1996) 97.
- [24] M. Anpo, T. Suzuki, E. Giamello, M. Che, *New Developments in Selective Oxidation*, Elsevier, Amsterdam, 1990, p. 683.
- [25] M. Anpo, Y. Shioya, M. Che, *Res. Chem. Intermed.* 17 (1992) 15.

- [26] M. Anpo, T. Suzuki, Y. Kubokawa, F. Tanaka, S. Yamashita, *J. Phys. Chem.* 88 (1984) 5778.
- [27] M. Anpo, M. Kondo, S. Coluccia, C. Louis, M. Che, *J. Am. Chem. Soc.* 111 (1989) 8791.
- [28] K. Ikeue, S. Nozaki, M. Ogawa, M. Anpo, *Catal. Lett.* 80 (2002) 111.
- [29] K. Ikeue, S. Nozaki, M. Ogawa, M. Anpo, *Catal. Today* 74 (2002) 241.
- [30] H. Yamashita, K. Ikeue, T. Takewaki, M. Anpo, *Top. Catal.* 18 (2002) 95.
- [31] K. Ikeue, H. Yamashita, M. Anpo, T. Takewaki, *J. Phys. Chem. B*, 105 (2001) 8350.
- [32] Y. Yoshimura, N. Kijima, T. Hayakawa, K. Murata, K. Suzuki, F. Mizukami, *Catal. Survey Jpn.* 4 (2000) 157.
- [33] A. Chatterjee, T. Iwasaki, Ebina, A. Miyamoto, *Microporous Mater.* 21 (1998) 421.
- [34] G. Saster, A. Corma, *Chem. Phys. Lett.* 302 (1999) 447.
- [35] R. Deka, R. Vetrivel, S. Pal, *J. Phys. Chem.* 103 (1999) 5978.
- [36] D. W. Breck, *Zeolite Molecular Sieves*, John Wiley & Sons, Inc., 1974.
- [37] S. T. King, *J. Catal.* 161(1996) 530
- [38] M. Anpo, M. Matsuoka, K. Hanou, H. Mishima, H. Yamashita, H. H. Patterson, *Coord. Chem. Rev.* 171(1998) 175.
- [39] A. Takahashi, R.T. Yang, *Langmuir*, 17 (2001) 8405.
- [40] P.A. Jacobs, J.B. Uytterhoeven, H.K. Beyer, *J. Chem.Soc. Chem. Commun.* (1977) 128.
- [41] G. Calzferri, S.Hug, T. Hugentobler, B, Sulzberger, *J. Photochem.* 26 (1984) 109.
- [42] J. Weitkamp, L. Puppe (Eds), *Catalysis and zeolites fundamentals and Applications*, Springer, Germany, 1999
- [43] S. J Gregg, K. S. W. Sing. *Adsorption, Surface Area and Porosity*, 2nd Ed; Academic Press: New York, 1982.
- [44] M. Gratzel *Heterogeneous Photochemical Electron Transfer*. CRC Press, Boca Raton, FL.
- [45] W. Wang, M. Gu, Y. Jin, *Materials Letters*, 57 (2003) 3276.
- [46] R. A. Schoonheydt, *J. Chem. Solids*, 50 (1989) 523.
- [47] J. Howard, J.M. Nicol, *Zeolites*, 8 (1988) 142.

Chapter - 5

COATING OF PHOTOCATALYSTS ON TILES & GLASS PLATES

5.1. Introduction

Titanium dioxide (TiO_2) is the most promising semiconductor photocatalyst, which has been extensively studied for waste water treatment and air purification, due to its good characteristics of powerful oxidation strength, chemical stability and non-toxicity. It is especially interesting to support TiO_2 on inert substrates for wastewater and indoor atmosphere pollution remediation. TiO_2 is a potent photocatalyst that can de-grade break down almost any organic compound it touches when exposed to sunlight in the presence of water vapor. The photocatalytic oxidation reaction with TiO_2 either in coated or dispersed form has been studied for last two decades. A commercially available TiO_2 containing greater than 80 percent of anatase and 20 percent rutile can be used as a photocatalyst to degrade various organic species to render it environmentally safe. These TiO_2 particles either coated on support material or dispersed in aqueous solution have been found to have good photocatalytic degradation efficiencies when it is desired to impact oxidation or reduction properties of organic moieties. Titanium dioxide have specific properties for its use as a photocatalyst such as (i) oxidation of water-bound environmental contaminants, irradiated with solar or simulated light; (ii) complete photo degradation of halocarbons, viz. dibromo-ethane, trichloroethylene; chloro-benzenes etc widely used as solvents in pesticides, insecticides, herbicides; (iii) photo destruction of different classes of organic dyes and biological stains from waste water; (iv) oxidation of cyanide found in rinse water of steel industry, electroplating, gold extraction, extraction in mines, to less toxic oxidation products. The latter is further oxidized to NO_3^- and CO_3^{2-} ; (v) reduction of metal ions to metallic state to remove toxic and noble metal ions from waste water; (vi) photo destruction of anionic, cationic and non-ionic surfactants under solar or simulated light using aqueous TiO_2 suspensions. The immobilization of TiO_2 in the form of a thin film provides an advantage over the drawbacks encountered with powder suspensions [1]: (i) separation of TiO_2 particles from the suspension is difficult, (ii) the suspended TiO_2 particles tend to aggregate especially at high concentrations and (iii) suspensions are difficult to apply to continuous flow systems.

Typically, photocatalyst is deposited on the surface of a support structure to provide a stable photo catalytic surface and to ensure that the flowing stream does not carry it away. To be effective, the contaminants must be brought into contact with the photocatalyst. Today, Companies are putting attention on a wide range of products that seek to capitalize on TiO_2 's reactivity, including self-cleaning fabrics, auto body finishes, and ceramic tiles. Also in development is a paving stone that uses the catalytic properties of TiO_2 to remove nitrogen oxide from the air, breaking it down into more environmentally benign substances that can then be washed away by rainfall. Other experiments with TiO_2 involve stripping organic pollutants such as trichloroethylene and methyl-tert-butyl ether from water; and degrading toxins produced by blue-green algae. It remains to be seen, however, whether the formation of undesirable intermediate products during these processes outweighs the benefits offered by TiO_2 's photocatalytic properties.

In recent years, "self-cleaning" coating using photocatalytic Titanium Dioxide (TiO_2) has gained considerable industry attention. With assistance of little UV light from fluorescence source or sunlight, TiO_2 offers two unique properties: (a) strong oxidation power, and (b) super-hydrophilicity. The first strong oxidation power can be used to kill bacteria attached on the wall, or oxide/remove foul smell from stains in toilet (e.g., TiO_2 -coated tile and TiO_2 -coated glass). The second super-hydrophilic property can allow dirt and stains to be easily washed away with water or by rainfall when such coating is applied to exterior surfaces.

The potential application of TiO_2 coated ceramic tiles and glass are high-rise office buildings (especially those with painted aluminum panels), towers, hotels, convention centres, shopping malls, train stations even train, Glass window, Plastic panels. The advantage of these coated ceramic tiles and glasses are: maintenance free, automatic removal of contaminated gas and odour, environmental friendly, reduces the maintenance cost.

To explore the potential use of TiO_2 , it is essential to immobilization of TiO_2 in such a way that it should absorb the maximum light and degradation of pollutant in air and water should not leach out TiO_2 . However, due to its strong photoreactivity, TiO_2 coating cannot be coated directly onto an organic paint surface as this will attack the paint surface itself, causing a phenomenon so called paint-chalking. Many efforts have been put toward the immobilization of TiO_2 on ceramic tiles, glass plates, and

fibers, using inorganic binder such as silica. Out of this more attention is given to coat the TiO₂ on ceramic tiles and glass so that it can be used in various places like hospitals, offices and homes for automatic removal of contaminated gas and to kill various bacteria.

Good photocatalytic activities of TiO₂ films necessitate (a) an efficient photo-induced electron–hole pair generation, and (b) an efficient charge separation, which requires in turn preparations of well-crystallized TiO₂ films, preferably in the anatase crystalline form [2,3].

A variety of physical and chemical approaches have been used for TiO₂ thin-film preparation. The sol–gel technique has emerged as one of the most promising techniques for growing TiO₂ thin films [4-9]. However, since the adherence of the TiO₂ coated surface with good activity is the main problem. Therefore, it will be very interesting and challenging to prepare the photocatalytically active stable surface.

5.1.1. Coating processes

In common practice, a coating/layer of TiO₂ on support material can be prepared by applying a smooth paste, removing the excess TiO₂ and heating/firing at higher temperature. Other methods of thin layer formation are spray pyrolysis, chemical vapour deposition, plasma enhanced vapour deposition. Some of the conventional methods for preparing stable coating are given below.

5.1.1.1. Dip Coating : This method refers to immersing a piece into a tank containing the coating material, removing the piece from the tank, and allowing it to drain. The coated piece can then be dried by force-drying or baking. Dip coating is well suited for high production coating of relatively simple shapes. Transfer efficiency is very high, all contact areas are coated, equipment requirements are low, and the process can be controlled manually and automated.

5.1.1.2. Flow Coating : In flow coating, the part is suspended, and the coating is poured over it. The excess material drips off and is collected for reuse. In a flow-coat system, 10 to 80 separate streams of coating material are directed to impinge on the parts. The streams flow out of drilled pipes or through short, crimped pipe outlets.

Flow coating is usually used for large or oddly shaped parts that are difficult or impossible to dip coat. Coatings applied by flow coating have only a poor to fair appearance unless the parts are rotated while dripping. Flow coating is fast and easy, requires little space, involves relatively low installation cost, requires low maintenance, and has a low labor requirement.

5.1.1.3. Spin Coating : Spray coating: In conventional or air atomized spraying, the coating is supplied to a spray gun by siphon, gravity, or pressure feed. When the gun trigger is pulled, the coating flows through the nozzle as a fluid stream. Compressed air from the center of the nozzle surrounds the fluid with a hollow cone as it leaves the nozzle, breaking the coating into small droplets and transferring velocity to it. Additional jets of compressed air from the nozzle break up the droplets further and form an elliptical pattern. Spray technique offers control of spray pattern.

The present work has been carried out with intention to use simple coating method to make a reliable and stable TiO₂ coated surface to remove the stains of turmeric and chilly emulsion which are mainly observed in the kitchen platform under the illumination in-house fluorescent light. The TiO₂ was coated on rough surface of ceramic tiles and the spot tests were carried out to degrade persistent stains caused by splashing, spilling of chilly and turmeric emulsion on the walls/platform of kitchen, invariably observed in Indian household under in-house fluorescent light.

5.2. Coating on Ceramic Tiles and Glass Plates

5.2.1. Materials

Ceramic tiles were purchased from locally, Glass plates, P25 Degussa procured from Degussa Corporation, Germany, and Silica sol from Aldrich, Mumbai. Sodium Silicate (Neutral grade) from Kadwani Chemicals, Jamnagar, India, 40 Watt fluorescent tube light from M/s Crompton & Greaves, India.

5.2.2. Photocatalyst Coating Procedure

5.2.2.1. Preparation of rough surface

For the immobilization of TiO₂ particle rough surface was prepared as follows: The ceramic tiles were dipped in water 24 hours. Then using the sand wheel the surface of ceramic tile was made rough and uniform. Tiles were cleaned several times by tap water and by distilled water to remove dust from the surface.

5.2.2.2. Preparation of coating mixture

For coating three types of mixtures prepared to coat on ceramic tiles and glass plates.

Mixture A, was prepared without binder, the varied amount of P25 TiO₂ in distilled water were 4%, 8%, 12%, and 15% w/v.

Mixture B, with sodium silicate (5%), as an inorganic binder the varied amount of P25 TiO₂ in distilled water were 4%, 8%, 12%, and 15% w/v.

Mixture C, with colloidal silica (5%) as a inorganic binder the varied amount of P25 TiO₂ in distilled water were 4%, 8%, 12%, and 15% w/v.

These mixtures were continuously stirred for 2 hours. Fresh mixture was used for the coating.

5.2.2.3. Dip coating procedure

In deep coating the ceramic tile and glass plates with rough and smooth surface were dipped in the solution contain TiO₂ (P25 Degussa) for 30 minutes then the tile and glass plates taken out and kept at an angle of 45 degree for 10 minute. After this tiles and glass plates dried at 80°C for two hours in oven. After drying the tiles and glass plates were calcined at various temperatures from 250-450°C for four hours in muffle furnace.

5.2.2.4. Spray coating procedure

In spray coating the mixture containing TiO₂ was sprayed using sprayer on the rough and smooth surface of the tiles and glass plates. The spraying was done in such a way that all surfaces of the tile and plates should get coated uniformly. After this tiles and glass plates were dried at 80°C for two hours in oven. After drying the tiles and plates were calcined at various temperatures from 250-450 °C for four hours in muffle furnace.

5.2.3. Adherence of photocatalyst

The adherence of TiO₂ on the surface is very important parameter for the photocatalytic surfaces. To get stable coated surface the adherence of TiO₂ on the surface should be very strong. To evaluate the strength of adherence of TiO₂ to the surface of the tile and glass plate was tested as follows:

5.2.3.1. Water of different pH

To study the effect of pH of solution on coated surfaces, coated tiles and glass plates were dipped for 12 hours under different pH solution and then cleaned with tap water. The removal of TiO₂ was observed visually.

5.2.3.2. Water of different temperature

To study the temperature sustainability of coated surfaces, coated tiles and glass plates were dipped in hot water bath at different temperature from 50-100°C for two hours to see the adherence of photocatalyst. The removal of TiO₂ was examined visually.

5.2.3.3. Under flow of water

To study the effect of flow of water on the coated surfaces, coated tiles and glass plates were kept under the flow of tap water continuously for two hours and the removal of TiO₂ particles from tile and glass plates surface was checked visually .

5.2.3.4. Applying adhesive tape

The adhesive tape was applied on the coated surface firmly and the removed to check the removal of photocatalyst from the surface of tiles and glass plates.

The adherence of photocatalyst on tiles and glass plate coated with mixture A was not good enough. The photocatalyst was removed after drying the tiles and glass plate. The adherence of photocatalyst on tiles and glass plate with mixture B was found better than the coated with mixture A. But in this case the catalyst gets removed under the flow of water. In case of mixture C, the adherence of TiO₂ on ceramic tiles and glass plates was good and all the tests mentioned above showed the adherence of the catalyst on the tile and surface of glass plates. This may be due to the rough surface of tiles and glass plates. The prepared rough surface of the ceramic tile is shown in Figure 5.1. This surface was coated with TiO₂ by spray coating technique using above mentioned mixture C as shown in Figure 5.2.

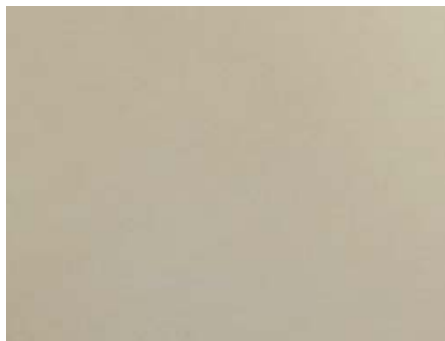


Figure 5.1: Prepared rough surface of ceramic tile.



Figure 5.2: Rough surface of ceramic tile coated with TiO₂.

5.3. Spot test under Fluorescent & Solar light

In general, the photocatalytic reaction between the excited surface and the organic species present in turmeric and chilly powder can be carried out under the influence of a weak light in a room. It is understood that higher efficiency of anatase-type TiO_2 for degradation of organic species depends significantly upon the energy band gap, which is ca. 3.2 eV. The band gap energy for such TiO_2 photocatalyst is the minimum energy of light required to make the material electrically conductive. The photoreaction under controlled light leads to surface excitation and simultaneously to the destruction of chromophoric organic species present in turmeric and chilly. The latter can be either in a mixture form with water or can be an emulsion with oil and water as is normally the case during cooking of a variety of dishes.

To check the photocatalytic activity of the coated tiles the spot test were carried out. To carry out the spot test, ceramic tile and glass plates coated with mixture C were used in the experiment. as it has showed the good adherence for all the tests. The spot test was carried out for 1) stains of emulsion of turmeric and chilly 2) MB and MG dyes under fluorescent tube light and solar light.

5.3.1. Spot Test for Removal of Stains of Emulsion of Turmeric and Chilly

The spot test for the removal of stains and dye spot was carried out on ceramic tiles and glass plates coated with TiO_2 . The spot test was carried out under fluorescent tubelight and solar light. The illumination intensity of the light falling on the tile was varied by adjusting the distance of the tubelight from the tile surface vertically. For spot test solar light, the tiles were exposed to sun light during afternoon from 12.00-3.00 P.M., which being maximum during this period. The tiles and glass plates exposed to sunlight were then kept in dark to avoid other stray light.

5.3.1.1. Stain mixture

To carry out the experiment for removal of stains, following composition of emulsions were used.

A: 25 ml water + 0.5 gm turmeric + 0.5 gm Chilly

B: 25 ml water + 0.5 gm turmeric + 1.0 gm Chilly

C: 25 ml water + 0.5 gm turmeric + 2.0 gm Chilly

D: 25 ml water + 0.5 gm turmeric + 3.0 gm Chilly

E: 25 ml water + 5 ml vegetable oil + 0.5 gm turmeric + 0.5 gm Chilly

F: 25 ml water + 5 ml vegetable oil + 1.0 gm turmeric + 1.0 gm Chilly

G: 25 ml water + 5 ml vegetable oil + 1.5 gm turmeric + 2.0 gm Chilly

H: 25 ml water + 5 ml vegetable oil + 0.5 gm turmeric + 3.0 gm Chilly

The above composition was thoroughly mixed, heated to 50°C for 10 minutes to get good dispersion of the turmeric and chilly in the final solution.

5.3.1.2. Spot Test on Ceramic Tiles

This test was carried out under fluorescent tube light as well as under solar light. The removal of stains of emulsion of turmeric and chilly of different compositions was examined under light intensity. The light intensity falling on the tiles was adjusted by varying the distance between the tile and the fluorescent tubelight vertically. The emulsion was applied on the coated tiles by brush. Half part of tile was irradiated with florescent tube light and another half part of the tile was covered to prevent light. The percentage of removal of stains was determined visually. Annexure-II lists some of the photographs for demonstrating the removal of stains with elapsed time. It was observed that the stains started getting dim on the surface exposed to light which vanished with the elapsed time. However, on the covered surface, the stains got a bit lighter than the first coat and it remained same with the elapsed time. The removal of stains was faster in tiles at higher luminance.

The removal of stains in solar light was found higher as compared to fluorescent tube light. Annexure-II shows photographs of the tile before and after exposure of fluorescent tube light and solar light with elapsed time.

Table 5.1: Removal of stains under fluorescent tube light (100 Lux) on ceramic tile.

Time (Hrs.)	Percentage stain removal							
	A	B	C	D	E	F	G	H
00	00	00	00	00	00	00	00	00
0.5	00	00	00	00	10	10	10	10
01	05	02	00	00	30	25	25	20
02	08	05	00	00	80	75	65	40
03	10	08	05	00	90	85	75	60
04	15	10	08	05	~100	95	85	70
05	20	15	12	10	-	~100	90	80
06	25	20	15	15	-	-	95	85
07	30	25	20	20	-	-	~100	90
08	40	30	30	25	-	-	-	95
09	45	35	35	30	-	-	-	~100
10	50	40	40	40	-	-	-	-
11	55	45	45	45	-	-	-	-
12	60	50	50	50	-	-	-	-
18	90	90	90	90	-	-	-	-
24	95	95	95	95	-	-	-	-
48	~100	~100	~100	~100				

Table 5.2: Removal of stains under fluorescent tube light (250 Lux) ceramic tile.

Time (Hrs.)	Percentage stain removal							
	A	B	C	D	E	F	G	H
00	00	00	00	00	00	00	00	00
0.5	00	00	00	00	15	12	10	10
01	05	05	05	05	45	40	30	20
02	10	10	10	08	65	60	50	30
03	15	15	15	12	90	80	70	40
04	20	20	20	15	~100	90	80	50
05	25	25	25	20	-	~100	90	60
06	30	30	30	25	-	-	95	70
07	35	35	35	30	-	-	~100	~100
08	40	40	40	35	-	-	-	-
09	45	45	45	40	-	-	-	-
10	50	50	50	45	-	-	-	-
11	55	60	55	50	-	-	-	-
12	60	65	60	55	-	-	-	-
18	90	90	90	90	-	-	-	-
24	95	95	95	95	-	-	-	-
48	~100	~100	~100	~100				

Table 5.3: Removal of stains under fluorescent tube light (350 Lux) on ceramic tile.

Time (Hrs.)	Percentage stain removal							
	A	B	C	D	E	F	G	H
00	00	00	00	00	00	00	00	00
0.5	10	05	05	05	15	12	10	20
01	15	15	12	10	45	40	30	50
02	20	30	25	15	65	60	50	60
03	30	40	35	20	90	80	80	70
04	40	45	45	25	~100	90	90	80
05	50	50	50	30	-	~100	95	90
06	55	60	60	35	-	-	~100	~100
07	60	70	70	40	-	-	-	-
08	65	75	75	45	-	-	-	-
09	70	80	80	50	-	-	-	-
10	75	85	80	55	-	-	-	-
11	80	85	85	60	-	-	-	-
12	85	90	85	65	-	-	-	-
18	95	95	95	95	-	-	-	-
24	~100	~100	~100	~100	-	-	-	-

Table 5.4: Removal of stains under solar light (4500 Lux) on ceramic tile.

Time (min)	Percentage stain removal							
	A	B	C	D	E	F	G	H
00	00	00	00	00	00	00	00	00
10	05	05	00	00	30	15	15	15
20	10	10	05	00	50	50	35	25
30	20	20	10	05	70	80	60	45
40	30	25	15	10	70	90	80	65
50	40	30	20	15	~100	~100	90	80
60	45	35	25	20	-	-	~100	90
90	50	40	30	25	-	-	-	~100
120	55	45	35	30	-	-	-	-
150	60	50	40	35	-	-	-	-
180	70	55	45	40	-	-	-	-
210	80	60	50	45	-	-	-	-
240	90	65	55	50	-	-	-	-
300	95	70	60	55	-	-	-	-
360	100	75	70	60	-	-	-	-
480	-	90	90	70				
600	-	~100	~100	80	-	-	-	-

5.3.1.3. Spot Test on Glass plate

Similar procedure and composition of emulsions were used to carry out the spot test on glass plates surface as mentioned in Section 5.3.1.2-5.3.1.3 for removal of stains on glass plate surface, both under fluorescent tubelight and sun light. The results were nearly same as compared to the ceramic tile. Annexure III lists the photographs taken before and after light exposure

5.3.2. Spot Test for MB & MG dyes

A drop of approximately 2 cm diameter of MB (50ppm) and MG (50ppm) was applied on the coated tiles and kept under fluorescent tube light and sunlight. The decolorisation of the drop was observed visually with the elapsed time. The decolorisation of dyes spot on the surfaces of ceramic tile and glass plate was found very slow as compare to the decrease in stains.

5.3.2.1. Dye concentration

To study the removal of dyes spot from the coated surface, 50 ppm solution of methylene blue and malachite green was used.

5.3.2.2. Spot Test on Ceramic tiles

Initially the water from the dyes solution got absorbed by the tile surface. During first one hour, there was small change in the intensity of the colour of dyes (MB: Blue, MG: Green). The decolorisation started after one hour and it was slow. The decolorisation reached to 80% in 24 hours after which there was no appreciable decolorisation. But after adding few drops of water, 100% decolorisation took place. This indicated that for decolorisation of dyes, presence of medium like water was required. The removal of dyes spot under fluorescent tubelight for different illuminations is given in Table 5.5-5.7 and under solar light in Table 5.8. The results showed that the removal of dyes spot was highest under solar light illumination as

compared to fluorescent tubelight due to the higher illuminance by solar light. The photographs of removal of dyes spot are shown in Annexure-III

Table 5.5: Removal of dye spots under fluorescent tube light on coated ceramic tile (100 lux)

Time (Hrs.)	Percentage dye removal under fluorescent light	
	MB	MG
00	00	00
0.5	00	00
01	05	00
02	10	05
03	15	10
04	20	15
05	25	20
06	30	25
07	35	30
08	40	35
09	45	40
10	50	45
11	60	50
12	65	55
18	70	60
24	90	70
48	100	80

Table 5.6: Removal of dye spots under fluorescent tube light coated ceramic tile (250 lux)

Time (Hrs.)	Percentage dye removal under fluorescent light	
	MB	MG
00	00	00
0.5	05	05
01	10	10
02	15	15
03	20	20
04	25	25
05	30	30
06	35	35
07	40	40
08	45	45
09	50	50
10	60	55
11	70	60
12	80	70
18	90	80
24	100	90
48	-	100

Table 5.7: Removal of dye spots under fluorescent tube light coated ceramic tile (450 lux)

Time (Hrs.)	Percentage dye removal under fluorescent light	
	MB	MG
00	00	00
0.5	15	10
01	20	15
02	25	20
03	30	25
04	35	30
05	40	35
06	45	40
07	50	45
08	65	50
09	70	55
10	80	60
11	90	70
12	100	80
18	-	90
24	-	100

Table 5.8: Removal of dye spots under solar light coated ceramic tile (4500 lux)

Time (Hrs.)	Percentage dye removal under solar light	
	MB	MG
00	00	00
0.5	10	5
01	25	15
02	40	25
03	50	35
04	60	45
05	70	50
06	80	60
07	90	70
08	100	80
09	-	90
10	-	100

5.3.2.3. Spot test on Glass plate

Similar tests were carried out on the coated glass plate. It was observed the removal of dyes spot from the glass plate was faster than from ceramic tile. The photographs of the removal of dyes spot are shown in Annexure-III

Table 5.9: Removal of dye spots under fluorescent tube light (350 Lux) on glass plate

Time (Hrs.)	Percentage dye removal under fluorescent light	
	MB	MG
00	00	00
0.5	00	00
01	05	15
02	10	25
03	15	30
04	20	35
05	25	40
06	30	45
07	35	50
08	40	55
09	45	60
10	50	65
11	55	70
12	60	75
18	65	80
24	75	~100
48	~90	

Table 5.10: Removal of dye spots under solar light (4500 Lux)

Time (Hrs.)	Percentage dye removal under solar light	
	MB	MG
00	00	00
0.5	20	30
01	30	40
02	35	45
03	45	50
04	55	55
05	60	60
06	65	65
07	70	70
08	75	75
09	85	85
10	~100	~100

5.4. Results & Discussions

The coating of TiO_2 on rough surface of ceramic tile and glass plate was done using spray coating technique. This coating was stable and highly photoactive in presence of fluorescent tube light and solar light.

The adherence of TiO_2 on ceramic tile was better than the glass plates. This was due to the large pores of ceramic tile and the TiO_2 particles got trapped in the pores of ceramic tile and the binding of colloidal silica with photocatalyst took place on tile ceramic material. This led to the strong adherence of TiO_2 on ceramic tile.

The reusability of the same tile was examined by repeating spot test at same place. It was found that there is no decrease in the photoactivity of tiles.

5.5. References

- [1] I. Sopyan, M. Watanabe, S. Murasawa, K. Hashimoto, A. Fujishima, *J. Photochemistry & Photobiology A* 98 (1996) 79.
- [2] K.M. Schindler, M. Kunst, *J. Phys. Chem.* 94 (1990) 8222.
- [3] K. Kato, A. Tsuzuki, H. Taoda, Y. Torii, T. Kato, Y. Butsugan, *J. Mater. Sci.* 29 (1994) 5911.
- [4] K.-N.P. Kumar, K. Keizer, A.J. Burgaaf, T. Okubo, H. Nagamoto, S. Morooka, *Nature* 358 (1992) 48.
- [5] K.-N.P. Kumar, J. Kumar, K. Keizer, *J. Amer. Ceram. Soc.* 77 (1994) 1396.
- [6] B.L. Bischoff, M.A. Anderson, *Chem. Mater.* 7 (1995) 1772.
- [7] R.R. Bacsa, M. Gratzel, *J. Am. Ceram. Soc.* 79 (1996) 2185.
- [8] M. Langlet, A. Kim, M. Audier, C. Guillard, J.M. Herrmann, *J. Mater. Sci.* 38 (2003) 3945.
- [9] M. Langlet, A. Kim, M. Audier, C. Guillard, J.M. Herrmann, *Thin Solid Films* 429 (2003) 13.

CHAPTER - 6

CONCLUSIONS

6.1. Conclusions

The study outlined in this thesis has evolved an easy synthesis method for highly photoactive nanocrystalline TiO₂ catalyst. The developed method has demonstrated that the photocatalyst can be tuned for parameters like bandgap, crystallite size, surface area and phase constitution for various demanding applications. Further during the study, it evolved that a simple spray technique can serve as a simple tool for coating purposes of photocatalyst on substrates like tiles as highlighted in the thesis that serves as an excellent platform for the degradation of effluents.

During this study, four types of photocatalysts were synthesized, characterized and were studied for their photocatalytic degradation capabilities. All photocatalysts were synthesized by sol-gel method. These catalysts are individually discussed below with highlight to the most efficient photocatalyst for the photocatalytic degradation of MB, MG, AP and NB:

6.1.1. Nanocrystalline TiO₂

The highly photoactive nanocrystalline TiO₂ (NPC-753) with low bandgap 3.1 eV, higher surface area 124 m² g⁻¹, predominant anatase phase, smaller crystallite size 14 nm was prepared by sol-gel method (Section 2.2.2). The amorphous phase of TiO₂ changed to anatase and then rutile as the temperature increased. The TiO₂ synthesized by this method was stable in anatase phase upto 833K and then it started to convert into rutile phase with increase in calcination temperature. Similar effects were observed for crystallite size and surface area of the catalyst. Thus it is established from the experimental results, that thermal treatment induces alterations in phase constitution, crystallite size and surface area of the catalyst. This study confirmed that a temperature of 753 K favours tailoring of optimum physical characteristics of the catalyst, where the photocatalytic activity of catalyst would be at its peak. Further, it was understood that at this calcination temperature, the bandgap of the catalyst was the lowest (3.1 eV) among all the catalysts calcined at temperatures other than 753 K temperature. Decrease in bandgap increases the absorption spectrum of the catalyst. Bandgap of the nanocrystalline TiO₂ was reduced

with increase in calcination temperature. This lowest bandgap with predominant anatase phase constitution favours increased light absorption capacity of the catalyst promoting greater number of electrons and holes at the surface of the catalyst. This greater number of electrons and holes participate in the oxidation and reduction process, thereby increasing its photocatalytic activity. The photocatalyst NPC-753 showed greatest photocatalytic degradation of MB, MG, AP, and NB amongst all catalysts prepared by method A.

6.1.2. Metal Ion Impregnated TiO₂

In metal impregnated catalysts, it was understood that metal dopants affect the characteristics and performance of catalyst. The XRD patterns of metal impregnated (Ag, Co, Cu, Fe, Ni) catalyst (MT-10) showed that the anatase phase of the catalyst was retained. This confirmed that the metal impregnated catalysts had nearly the same phase constitution. However, it was found that the crystallite size of the metal impregnated catalysts varied from the bare catalyst MT-10 (crystallite size 30nm) in order of Ag-doped (44 nm) < Fe-doped (45 nm) < Ni-doped (48 nm) < Co-doped (49 nm) < Cu-doped (50 nm). The lowest crystallite size in Ag-doped enhances the promotion of electrons and holes to the surface of the catalyst coupled with decrease in recombination rate within the catalyst. This imparts increased photocatalytic activity as compared to other metal impregnated catalysts. Also highest surface area was obtained for Ag-impregnated catalyst. The lowest bandgap was obtained for Ni-impregnated catalyst, but its photocatalytic degradation for all substrates was phenomenally less as compared to Ag-impregnated catalyst. The reason ascribed to this was the high surface area of Ag-impregnated catalyst that provided more active sites for redox reactions at the surface as confirmed by this experimental finding.

6.1.3. TiO₂ Encapsulated in Zeolites

The encapsulation of catalyst in zeolites induces fine dispersion in the cavities of zeolite. The lower amount of TiO₂ was chosen to get fine dispersion in zeolite cavities with out alteration in the structure of zeolite with was confirmed by XRD studies. The inherently high surface area of zeolite provides greater active sites for photocatalytic activity to the catalyst. The TiO₂ encapsulation possesses quantum size effect which populates more number of electron hole pairs for the degradation of substrates. The catalysts encapsulated with lower amount of TiO₂ showed the higher photocatalytic activity. The higher photocatalytic activity was obtained in TiO₂ encapsulated HY zeolite catalysts.

6.1.4. Cation Exchange on TiO₂ Encapsulated Catalysts in Zeolite

The post modification by ion exchange method (chapter 3, 4) was also carried out to study the photocatalytic property of the catalyst. The cation exchange was done using Ag, Co, Cu, Fe and Ni metal ions in the zeolite framework. Among these catalysts, the Ag cation exchanged catalyst demonstrated the highest photocatalytic activity for the degradation of substrates compared to other metal ions exchanged catalysts. This can be attributed to the quantum size confinement effects in zeolite cavities that promote increased number of electron-hole pairs at the surface of photocatalyst participating in redox reactions thereby enhancing photocatalytic degradation of effluents. Also, it was observed that Ag cation exchanged catalyst in zeolite framework exhibited higher photocatalytic activity as compared to TiO₂ encapsulated in zeolite. This study has established that the incorporation of metal ion exchange in TiO₂ encapsulated zeolite catalysts can produce a catalyst with splendid photocatalytic degradation capabilities.

6.2. Scope and Future Prospects

The synthesis method for photocatalysts outlined in this thesis has the potential to function as a reliable catalyst production process for its simplicity and less number of steps. This makes it economical to manufacture these catalysts. Also, the simple coating

technique on tiles makes it a potential approach for developing photocatalysis that rugged enough to withstand the harsh conditions. These components have been demonstrated to function according to the devised theory & method and results derived in this thesis. The described synthesis method for photocatalyst can be scaled up for industrial level production. This thesis forms a starting point for large scale industrial production of photocatalyst with excellent photocatalytic degradation characteristics. The results obtained during this study are far encouraging.

In the future it is possible to synthesize photocatalysts using other metal complexes, algae and other ligand systems. This can simply be done by its incorporation in catalyst as outlined in this thesis.

An essential part of the photodegradation element manufacturing process is the coating of photocatalyst films by an easiest means such as spray coating as demonstrated in this thesis. It is possible to manufacture a large number of reactor structures either open welled or, open or closed troughs with these photocatalytic tiles for large volume degradation of effluents. The simple spray coating can very easily be done anyone without much specialized training. This can help in upcoming of small scale industries providing employment opportunities to unemployed population.

This kind of catalyst can be coated on various substrates likes fibers, clothes, plastics, papers which can be shaped in to some ornamental showpieces that would adorn homes, cars etc. and the coat will degrade VOCs, provide clean surface and air. These photocatalysts can be mixed coated with distempers, whitewash etc. that will restrict the indoor pollution and protect the high raised beautiful buildings, monuments, heritage structures from the polluted air. Photocatalysts can kill the cancerous bacteria. Photocatalytic reactor can degrade the flowing effluents.

Nanostructured TiO_2 are reported to have applications as films in electrochromic devices that control light transmission in windows or light reflection in mirrors and displays. Most heterogeneous catalysts consist of small metal clusters on an oxide support, many growth studies of metals on TiO_2 have been performed which often serve as a model for other metal/oxide surfaces. When TiO_2 is mixed with vanadia it works for selective oxidation reactions. Adsorption of simple molecules like O_2 , CO , CO_2 has also been

investigated for a few metal overlayers or clusters on TiO₂ that can provide separation of these gases from mixture of gases.

The solar energy conversion is an extensively explored active area of research. These photocatalysts coated on solar panel can enhance their conversion efficiency. TiO₂ photocatalyst can serve as a cheaper alternate to conventional Si or Ge based solar cells. These catalysts can be used as photocatalyst for H₂ production from water by utilizing sunlight and will be a promising tool for solar energy conversion in future.

Annexure-I

List of Regulated Air Pollutants:

** For the purposes of Air Pollution Control Permit Applications, hazardous air pollutants (HAPs) that are volatile organic compounds (VOCs) should be included as VOCs for reflection of total VOCs from the facility and need to be identified separately as well.*

Total suspended particulate matter	Hydrochlorofluorocarbon-21
Particulate matter less than 10 microns	Hydrochlorofluorocarbon-22
Sulfur dioxide	Hydrochlorofluorocarbon-31
Nitrogen oxides	Hydrochlorofluorocarbon-121
Carbon monoxide	Hydrochlorofluorocarbon-122
Volatile organic compounds (VOCs)*	Hydrochlorofluorocarbon-123
Lead	Hydrochlorofluorocarbon-124
Dioxin/Furan	Hydrochlorofluorocarbon-131
Fluorides	Hydrochlorofluorocarbon-132
Hydrogen chloride	Hydrochlorofluorocarbon-133
Hydrogen sulfide	Hydrochlorofluorocarbon-141
Sulfuric acid mist	Hydrochlorofluorocarbon-142
Total reduced sulfur	Hydrochlorofluorocarbon-221
Reduced sulfur compounds	Hydrochlorofluorocarbon-222
Arsenic	Hydrochlorofluorocarbon-223
Asbestos	Hydrochlorofluorocarbon-224
Beryllium	Hydrochlorofluorocarbon-225
Benzene	Hydrochlorofluorocarbon-226
Mercury	Hydrochlorofluorocarbon-231
Radionuclides	Hydrochlorofluorocarbon-232
Vinyl chloride	Hydrochlorofluorocarbon-233
Carbon tetrachloride	Hydrochlorofluorocarbon-234
Chlorofluorocarbon-11	Hydrochlorofluorocarbon-235
Chlorofluorocarbon-12	Hydrochlorofluorocarbon-241
Chlorofluorocarbon-13	Hydrochlorofluorocarbon-242
Chlorofluorocarbon-111	Hydrochlorofluorocarbon-243
Chlorofluorocarbon-112	Hydrochlorofluorocarbon-244
Chlorofluorocarbon-113	Hydrochlorofluorocarbon-251
Chlorofluorocarbon-114	Hydrochlorofluorocarbon-252
Chlorofluorocarbon-115	Hydrochlorofluorocarbon-253

Chlorofluorocarbon-211	Hydrochlorofluorocarbon-261
Chlorofluorocarbon-212	Hydrochlorofluorocarbon-262
Chlorofluorocarbon-213	Hydrochlorofluorocarbon-271
Chlorofluorocarbon-214	Halon-1211
Chlorofluorocarbon-215	Halon-1301
Chlorofluorocarbon-216	Halon-2402
Chlorofluorocarbon-217	Methyl chloroform

* - Volatile organic compounds (VOC) includes any compound of carbon, excluding carbon monoxide, carbonic acid, metallic carbides or carbonates and ammonium carbonate, which participates in atmospheric photochemical reactions. This includes any such organic compound other than the following which have been determined to have negligible photochemical reactivity: Methane; ethane; methylene chloride; 1,1,1-trichloroethane; CFC-113, CFC-11, CFC-12, CFC-22, FC-23; CFC-114; CFC-115; HCFC-123; HFC-134a; HCFC-141b; HCFC-142b; HCFC-124; HFC-125; HFC-125; HFC-134; HFC-143a; HFC-153a; and perfluorocarbon compounds which fall into these classes: (i) Cyclic, branched, or linear, completely fluorinated alkanes; (ii) Cyclic, benched, or linear, completely fluorinated ethers with no unsaturations; (iii) Cyclic, branched, or linear completely fluorinated tertiary amines with no unsaturations; and (iv) Sulfur containing perfluorocarbons with no unsaturations and with sulfur bonds only to carbon and fluorine.

Annexure-II

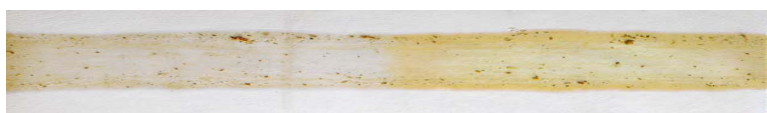
Removal of stain of mixture 5 under fluorescent tube light illumination (350 Lux) on coated ceramic tile (a) before illumination of light (b) after 1 hour (c) after 4hours.



a) Before exposure to illumination.



b) After 1 hour with continuous illumination.



c) After 4 hours continuous illumination.

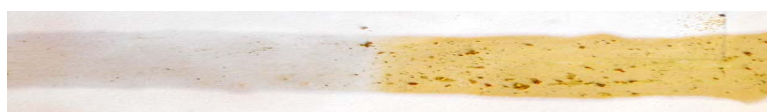
Removal of stain of mixture 5 under solar light illumination (4500 LUX) a) before illumination of light on coated ceramic tile (a) before illumination of light (b) after 1 hour (c) after 4 hours (d) after 6 hours



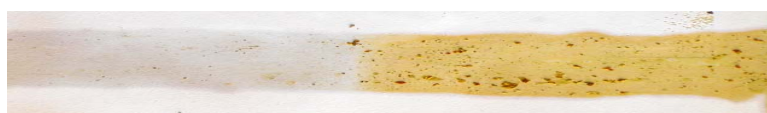
a) Before illumination of solar light



b) After 30 minutes with continuous exposure to solar light.



c) After 50 minutes with continuous exposure to solar light..



d) After 90 minutes exposure to solar light.

Annexure-III

Removal of stains on coated glass plate

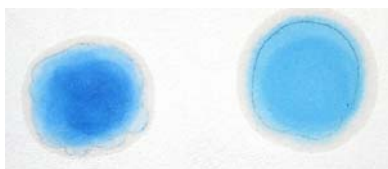


a) Before irradiation of fluorescent light



b) After irradiation of fluorescent light (20Hrs.)

Removal of dyes spot on coated ceramic Tiles



a) Before irradiation of fluorescent light



b) After irradiation of fluorescent light (48 Hrs.)

Removal of dyes spot on coated glass plate



MB

MG

a) Before irradiation of fluorescent light



MB

MG

b) After irradiation of fluorescent light (48 Hrs.)

Annexure-IV

LIST OF PATENTS GRANTED / FILED

1. **Photocatalytic auto cleaning process of chilly and turmeric stains under fluorescent light.**

Pushpito Kumar Ghosh, Raksh Vir Jasra, Dipak Balvantrai Shukla, Anjani Ketan Bhatt, **Rajesh Jagannath Tayade** (Submitted)

LIST OF PUBLICATIONS

1. Photocatalytic Degradation of Nitrobenzene Using Nanocrystalline TiO₂.
Rajesh J. Tayade, Ramchandra G. Kulkarni and Raksh. V. Jasra
(communicated)
2. Synthesis and characterization of impregnated mesoporous TiO₂ using transition metal ion of various work function for degradation of nitrobenzene.
Rajesh J. Tayade, Ramchandra G. Kulkarni and Raksh. V. Jasra
(communicated)

LIST OF POSTER PRESENTED

1. Synthesis & characterisation of titanium dioxide porous nanosphere using sol-gel method for degradation of various dyes.
R. J. Tayade, R. G. Kulkarni, R. V. Jasra, 3rd All Gujarat Research Scholar Meet, M.S. University, Baroda. (Feb 2003)
2. Photocatalytic degradation of Methylene Blue dye with nanocrystalline titanium dioxide synthesized using sol-gel method.
R. J. Tayade, R. G. Kulkarni, R. V. Jasra, International Symposium on Chemical Education and Research, Dept. of Chemistry, Loyola College, Chennai (Jan 2004).